FACHBEREICH MATHEMATIK UND NATURWISSENSCHAFTEN
FACHGRUPPE PHYSIK
BERGISCHE UNIVERSITÄT
WUPPERTAL

Measurement of the W boson helicity in $t\bar{t}$ decays

Christian Schmitt

Juni 2005
WUB-DIS 2005-07

Diese Dissertation kann wie folgt zitiert werden:

urn:nbn:de:hbz:468-20050717
[http://nbn-resolving.de/urn/resolver.pl?urn=urn%3Anbn%3Ade%3Ahbz%3A468-20050717]

Contents

List of Tables

List of Figures

1 Introduction

The top quark was the last missing quark to complete the three generations existing in the standard model of particle physics. It is by far the heaviest of all known fermions and might even be heavier than the predicted Higgs boson: a single top quark is as heavy as a whole gold atom and about five orders of magnitude heavier than the up or down quark. The high mass gives rise to unique features of the top quark: it is the only known particle that has a Yukawa coupling to the standard model Higgs boson of order unity and its very short lifetime, a direct consequence of its high mass, opens up the possibility to study a bare quark, free from hadronization effects.

Apart from the importance of the top quark mass in the indirect determination of the mass of the Higgs boson through virtual loop corrections to the W boson mass, the top quark plays an important role in the search for new physics: assuming that the standard model is just a low energy approximation of a more fundamental theory, deviations from the standard model predictions might be first observed in the top quark sector due to the high mass of the top quark.

Even if the top quark turns out to be nothing more than just the weak isospin partner of the b quark, it is extremely important to study its properties as events containing top quarks will be an important background in the searches for new physics at the next proton-proton collider at CERN, the Large Hadron Collider. A good understanding of the background from events containing top quarks will be mandatory in order to establish new particles.

The subject of this thesis is the measurement of the helicity of the W boson produced in the decay of the top quark. The standard model predicts the helicity of these W bosons to be either negative or zero, but not positive. In case the top quark sector is already influenced by effects from new physics, the weak charged current, responsible for the decay of the top quark, can be altered from a pure $V - A$ charged current interaction to a pure $V + A$ interaction or a mixture between these two scenarios. This would decrease the fraction of W bosons with negative helicity and W bosons with positive helicity would appear. A change would then be visible in the distribution of the decay angle θ between the lepton and the (negative) b quark direction in the rest frame of the W boson.

In chapter two the basic theoretical framework is outlined. Starting from a very brief description of the standard model of particle physics, the production and the decay

of top quarks are presented. This analysis makes use of proton-antiproton collisions produced at the Fermilab Tevatron collider and recorded with the DØ detector. The third chapter describes the experimental setup of the Tevatron and the DØ experiment with its individual subdetectors.

The different signals recorded by the DØ detector need to be converted into physics objects. Chapter four describes the methods and algorithms used to reconstruct the individual physics objects as well as the reconstruction of the whole $t\bar{t}$ system and its decay products. The actual data sample and the initial selection criteria applied at the trigger level as well as at the preselection level are described in chapter five. This selection is necessary to reduce the amount of background events: the $t\bar{t}$ production cross section is nearly ten orders of magnitude smaller than the total inelastic cross section for proton-antiproton collisions.

The actual measurement of the W helicity is presented in chapter six. The background contamination of the data sample is reduced using b quark identification and a topological selection with a discriminant that combines different variables to obtain an optimal separation between background and $t\bar{t}$ events. By constraining the top quark mass to 175 GeV, the resolution in $\cos\theta$ can be improved leading to a more precise measurement of the fraction of W bosons with positive helicity. At the end of chapter six a detailed study of systematic uncertainties, potentially affecting the measurement, is described.

Chapter seven summarizes the result of this measurement and compares it with other methods and measurements of the W helicity in top quark decays. Finally, an outlook of the expected uncertainty achievable using this method at the end of the Tevatron run in 2009 is given together with the expected precision reachable at the upcoming Large Hadron Collider.

2 Theory

2.1 The Standard Model

One of the major achievements in physical science in the last decades of the 20^{th} century was the development of a theory describing the basic building blocks in nature: the Standard Model (SM) of particle physics. It incorporates three of the four known fundamental interactions, electric, weak and strong. The development of the standard model started with the combination of the weak and the electromagnetic interaction into a single theory by Glashow, Salam and Weinberg [1, 2, 3] in the middle sixties of the last century.

At roughly the same time, Gell-Mann, Ne'eman and Zweig [4, 5, 6] derived the quark hypothesis. This theory implies that all particles that interact strongly carry a new degree of freedom: the color. In the mid 70^{th} a corresponding gauge theory, called Quantum Chromodynamics (QCD), was developed. The combination of these developments lead to the standard model: a gauge theory based on the mathematical framework of local $SU(3)_c \times SU(2)_L \times U(1)_Y$ invariances.

Just like ordinary quantum mechanics fails in the relativistic limit, it is not expected that the standard model remains valid over the whole energy scale. However, its remarkable success up to energies of around 100 GeV suggests that it will remain an excellent approximation to nature at least up to energies of $\mathcal{O}(100\,\text{GeV})$.

There are countless textbooks available that describe in detail the theory behind the standard model [7, 8, 9]. Therefore only a very brief overview of the general concepts will be given, followed by a more detailed description of the topics relevant to this thesis.

2.1.1 Particle content and interactions

In the standard model matter is built from elementary fermions, the leptons and the quarks, with half a unit of intrinsic angular momentum, or spin. There exist three generations of fermions that are identical in every attribute except for their mass. Table 2.1 lists these elementary fermions together with their quantum numbers. Here the neutrinos are still treated as massless, i.e. they only appear as left-handed parti-

Fermions			Q	I	I_3	Y
	Leptons					
$\begin{pmatrix} \nu_e \\ e^- \end{pmatrix}_L$	$\begin{pmatrix} \nu_\mu \\ \mu^- \end{pmatrix}_L$	$\begin{pmatrix} \nu_\tau \\ \tau^- \end{pmatrix}_L$	$\begin{matrix} 0 \\ -1 \end{matrix}$	$+1/2$	$\begin{matrix} +1/2 \\ -1/2 \end{matrix}$	-1
e_R^-	μ_R^-	τ_R^-	-1	0	0	-2
	Quarks					
$\begin{pmatrix} u \\ d \end{pmatrix}_L$	$\begin{pmatrix} c \\ s \end{pmatrix}_L$	$\begin{pmatrix} t \\ b \end{pmatrix}_L$	$\begin{matrix} +2/3 \\ -1/3 \end{matrix}$	$+1/2$	$\begin{matrix} +1/2 \\ -1/2 \end{matrix}$	$+1/3$
u_R	c_R	t_R	$+2/3$	0	0	$+4/3$
d_R	s_R	b_R	$-1/3$	0	0	$-2/3$

Table 2.1: List of the fundamental fermions together with their charge Q, their quantum numbers for the weak isospin I,I_3, and the hypercharge Y. The corresponding anti-fermions are not shown nor the fact that the quarks carry a color charge. The subscript L,R refers to the chirality of the particle.

cles. Recent results on neutrino oscillations [10] suggest that the neutrinos do have in fact a very small mass. In this case the list has to be extended to incorporate three right-handed neutrinos.

The interactions are described in the standard model via the exchange of gauge bosons with spin 1. In Quantum Electrodynamics (QED), the interactions among electrically charged particles are due to the exchange of photons (γ), the quanta of the electromagnetic field. The fact that the photon is massless and carries no charge itself accounts for the long range of the electromagnetic force.

Table 2.2 summarizes the properties of the gauge bosons and identifies the bosons with the interactions. It includes already the gauge bosons of the strong and electroweak interactions that will be described in the following.

2.1.2 The strong interaction

Another interaction with massless bosons is the strong interaction. It is described by Quantum Chromodynamics (QCD) which is a gauge theory based on the gauge group $SU(3)_c$. The force is mediated by the eight gauge bosons of this group, the gluons. Three different color charges exist, called "red", "green" and "blue" and the

	Gluon	γ	Z	$W^{\pm}$
Interaction	strong	electromagnetic	weak	
Gauge group	$SU(3)_c$	$SU(2)_L \times U(1)_Y$		
Mass/GeV	0	0	91.1876 ± 0.0021	80.425 ± 0.038
Width/GeV	0	0	2.4952 ± 0.0023	2.124 ± 0.041

Table 2.2: The gauge bosons of the standard model. The values for the mass and the width of the W and Z boson are taken from Ref. [11].

corresponding anti-colors. A $SU(3)_c$ triplet consists of a red, green and blue quark of identical flavor. The strong interaction does not change flavor.

In contrast to the photon, the gluons carry color charge and hence couple to each other. This fact has an important consequence: the color force between colored particles increases in strength with increasing distance. Particles that carry color, quarks and gluons, do not appear as free particles but exist only inside compound objects called hadrons ("confinement"). In contrast to the confinement at large distances and therefore low energies, the colored particles can move quasi-free at small distances respectively high energies. This behavior is called "asymptotic freedom".

These two effects, confinement and asymptotic freedom, are reflected in the theory by an energy dependent coupling constant[1] α_s that rises rapidly with decreasing energy. In first order perturbation theory α_s can be written as function of the energy scale Q^2:

$$\alpha_s(Q^2) = \frac{12\pi}{(33 - 2n_f) \cdot \ln(Q^2/\Lambda^2_{QCD})}\,, \tag{2.1}$$

where Λ_{QCD} is the only free parameter in the QCD and n_f is the number of contributing quark flavors. This number depends on Q^2 because virtual quark-antiquark pairs from heavy quarks can only be resolved at high values of Q^2.

2.1.3 The electroweak interaction

Strictly speaking, the electroweak theory is not a unified field theory of the weak and electromagnetic interaction as it contains two distinct coupling constants g' and g for the $SU(2)_L$ and the $U(1)_Y$ interactions, respectively.

In the $SU(2)$ sector, the left-handed fermions form an isodoublet, while the right-handed fermions form an isosinglet as shown in Table 2.1 where the indices L and R

[1] The name "constant" is only used in analogy to the coupling constant α of the electromagnetic interaction which, historically, was assumed to be constant.

indicate the handedness. This curious feature, that e.g. the charged leptons are split into two parts, with the left- and the right-handed part transforming differently, is a consequence of the fact that the weak interaction violates parity. Theoretically, this parity violation is described by the so called $V - A$ interaction. In the Dirac algebra this is represented by a factor $\gamma^\mu(1-\gamma_5)$, where $\gamma^\mu\gamma_5$ applied to a Dirac spinor ψ forms the axial vector part of the coupling. The left and right-handed fields are then defined as

$$\psi_L = \frac{1}{2}(1-\gamma_5)\psi\,, \tag{2.2}$$

$$\psi_R = \frac{1}{2}(1+\gamma_5)\psi\,. \tag{2.3}$$

The generators of the $SU(2)_L$ gauge group are the massless gauge bosons W^1, W^2 and W^3 that form a triplet and the conserved quantum number is the weak isospin I.

The electric charge Q of an isodoublet, e.g. (ν_e, e), is $(0, -1)$ which is not equal to the eigenvalue of the isospin operator T_3. Thus, to get the charge correctly, an additional quantum number is needed, the hypercharge Y, which is associated with the gauge group $U(1)_Y$. The charge can then be defined as:

$$Q = I_3 + \frac{Y}{2}\,, \tag{2.4}$$

where $I_3 = \pm 1/2$ and $Y = -1$ for the left-handed doublets and $T_3 = 0$ and $Y = -2$ for the right-handed singlets. The gauge boson associated with $U(1)_Y$ is the singlet B^0.

The four vector bosons involved in the electroweak interaction are the γ, the Z and the two W bosons. Experimentally it was found that the Z boson, though not carrying electric charge itself, couples differently to charged leptons and neutrinos. It can therefore not be identified with the W^3. Thus the physically observable bosons must be a mixture of the gauge bosons B^0, W^1, W^2 and W^3:

$$W^\pm = \frac{1}{\sqrt{2}}(W^1 \mp iW^2) \tag{2.5}$$

$$\begin{pmatrix} Z \\ \gamma \end{pmatrix} = \begin{pmatrix} \cos\theta_W & \sin\theta_W \\ -\sin\theta_W & \cos\theta_W \end{pmatrix} \begin{pmatrix} B^0 \\ W^3 \end{pmatrix}, \tag{2.6}$$

where the angle θ_W is called the Weinberg angle. It can be expressed in terms of the coupling constants g' and g as

$$\sin\theta_W = \frac{g'}{\sqrt{g^2 + g'^2}}\,. \tag{2.7}$$

This is not the only place in the electroweak interaction where a mixing takes place. There is also a mixing in the quark sector: Only the weak interaction is able to change

a member of an isospin doublet to the corresponding partner within the same family. As a consequence, the lighter quarks in each doublet will be stable, specifically, the b quark would be stable as its mass is lower than that of its partner, the top quark.

However, stable particles containing b quarks are not found in nature. Instead the decay of b quarks into quarks from the second or first family are observed. Hence, the electroweak eigenstate b' must be different from the mass eigenstate b. These different eigenstates are related via the Cabibbo-Kobayashi-Maskawa (CKM) matrix [12]:

$$\begin{pmatrix} d' \\ s' \\ b' \end{pmatrix} = \begin{pmatrix} V_{ud} & V_{us} & V_{ub} \\ V_{cd} & V_{cs} & V_{cb} \\ V_{td} & V_{ts} & V_{tb} \end{pmatrix} \begin{pmatrix} d \\ s \\ b \end{pmatrix} \tag{2.8}$$

The transition probability of a quark q_i to another quark q_j is proportional to $|V_{q_i q_j}|^2$.

2.1.4 The Higgs mechanism

The fermions and the bosons in the electroweak theory have to be massless in order to keep the local $SU(2)_L \times U(1)_Y$ gauge invariance. However, the W and the Z boson are observed to be heavy particles. To solve this apparent problem of the electroweak theory, a dynamical way of creating the masses was suggested by Higgs [13]: the introduction of a scalar isospin doublet ϕ,

$$\phi = \begin{pmatrix} \phi^+ \\ \phi^0 \end{pmatrix} = \begin{pmatrix} \phi_1^+ + i\phi_2^+ \\ \phi_1^0 + i\phi_2^0 \end{pmatrix}, \tag{2.9}$$

that couples to the gauge bosons.

The only general form, consistent with the gauge symmetry, for the scalar potential V is

$$V(\phi) = \mu^2 \phi^\dagger \phi + \lambda (\phi^\dagger \phi)^2 , \tag{2.10}$$

with $\mu^2 < 0$ and $\lambda > 0$. This potential has a non-vanishing vacuum expectation value of $|\phi| = v := \sqrt{-\mu^2/\lambda}$, which translates into a specific realization of the ground state on the sphere $|\phi| = v$ and therefore a breaking of the symmetry. This behavior is called spontaneous symmetry breaking. The parameter $\sqrt{-\mu^2}$ corresponds to the mass of the scalar Higgs boson and the parameter λ to the Higgs self interaction. The parameter v can be determined from experiments, $v \approx 246$ GeV. However, the mass of the Higgs boson itself is not predicted as it depends not only on v but also on the parameter λ.

The introduction of the scalar isospin doublet ϕ leads to massive gauge bosons through the coupling of ϕ with the gauge bosons:

$$M_W = \frac{1}{2} v g \tag{2.11}$$

$$M_Z = \frac{1}{2} v \sqrt{g^2 + g'^2} \tag{2.12}$$

and the Yukawa interaction of the Higgs field with a fermion f_i gives raise to its mass:

$$m_{f_i} = \frac{1}{\sqrt{2}} \lambda_i v \,, \tag{2.13}$$

where λ_i is the coupling of the fermion i to the Higgs field. These Yukawa couplings are not determined by the theory.

2.2 The top quark

The top quark plays an important role not only since its discovery in 1995 but also before, when its presence could only be inferred from the need for an up-type partner of the b quark. At LEP [2] the electroweak sector of the standard model was extensively tested and even though the top quark is too heavy to be produced at LEP, the results were already influenced by the top quark through higher order corrections.

The gauge, matter, and Higgs sectors of the standard model depend only on the three gauge couplings g_S, g, g', the vacuum expectation value of the Higgs field, v, and the self interaction of the Higgs, λ. The lowest order, i.e. tree level, electroweak quantities even depend on only three of these five parameters: g, g' and v. These three parameters can be determined from the three best measured electroweak quantities [11]:

$$\alpha(Q^2 = 0) = \frac{1}{4\pi} \frac{g^2 g'^2}{g^2 + g'^2} = 7.297352568(24) \times 10^{-3} \tag{2.14}$$

$$G_F = \frac{1}{\sqrt{2} v^2} = 1.16637(1) \times 10^{-5}\ \text{GeV}^{-2} \tag{2.15}$$

$$M_Z = \frac{1}{2} \sqrt{g^2 + g'^2}\, v = 91.1876(21)\ \text{GeV} \,, \tag{2.16}$$

where the uncertainties in the last digits are given in parentheses. Using these quantities, all other electroweak quantities can be predicted. Using the relation between the mass of the Z and the W boson

$$\frac{m_W}{m_Z} = \frac{g'}{\sqrt{g'^2 + g^2}} \equiv \cos\theta_W \,, \tag{2.17}$$

where θ_W is the Weinberg angle, the mass of the W boson can be written as

$$m_W = \frac{\pi \alpha}{\sqrt{2} G_F \sin^2\theta_W (1 - \Delta r)} \,. \tag{2.18}$$

[2] Large Electron Positron collider

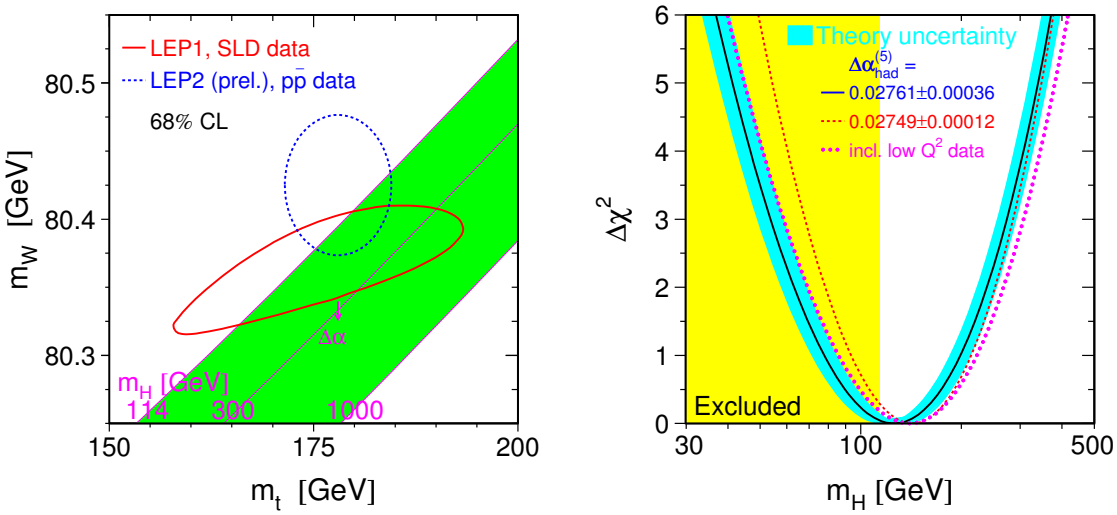

Figure 2.1: Lines of constant Higgs mass on a plot of the W boson mass versus the top quark mass (left) and a χ^2 fit for the prediction of the Higgs boson mass from precision electroweak data (right). Both plots are taken from Ref. [15]

The correction Δr is due to one-loop processes and that is the place where the top quark plays an important role as it contributes to this correction [14]:

$$(\Delta r)_{\text{top}} \approx -\frac{3G_F m_{\text{top}}^2}{8\sqrt{2}\pi^2}\frac{1}{\tan^2\theta_W}\,. \tag{2.19}$$

The top contribution depends quadratically on the top quark mass and has been used to obtain an indirect top mass determination from electroweak measurements [15]:

$$m_{\text{top}} = 179^{+12}_{-9}\ \text{GeV} \tag{2.20}$$

This is in good agreement with the direct measurement of the top quark mass [11]:

$$m_{\text{top}} = 174.3 \pm 5.1\ \text{GeV} \tag{2.21}$$

Not only the top quark contributes to the one-loop corrections of the W boson mass but also the Higgs boson. However, this contribution depends only logarithmically on the mass of the Higgs boson [14]:

$$(\Delta r)_{\text{Higgs}} \approx \frac{11G_F M_Z^2\cos^2\theta_W}{24\sqrt{2}\pi^2}\ln\frac{m_H^2}{M_Z^2}\,. \tag{2.22}$$

Figure 2.1 shows the prediction for the mass of the Higgs boson as function of the mass of the W boson as well as the mass of the top quark. This prediction is much less precise due to the fact that the dependence is only logarithmic.

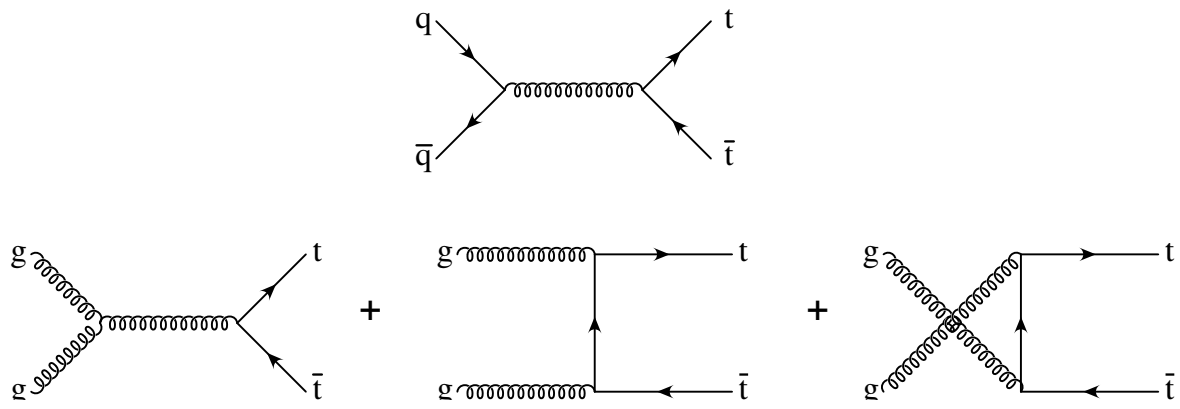

Figure 2.2: Feynman diagrams showing the strong production of top quark pairs at hadron colliders: through quark-antiquark annihilation (top) and gluon-gluon fusion (bottom).

2.2.1 Production of top quarks

The top quark is produced at hadron colliders primarily through the strong interaction via the annihilation of a quark and an antiquark or via the fusion of two gluons. The corresponding Feynman diagrams are shown in Figure 2.2.

Due to the fact, that the partons involved in producing the top quark carry only a fraction x of the momentum of the proton or anti-proton, the contributions from the two processes depend on x and the corresponding parton density functions (PDFs). The typical value of x for $t\bar{t}$ production can be estimated from the mass of the top quark and the center of mass energy $\sqrt{s}$: $x \approx 2m_t/\sqrt{s}$. At a center of mass energy of 1.96 TeV this corresponds to $x \approx 0.18$. This relatively large value for x reduces the contribution from the gluon-gluon fusion process due to the low gluon PDF at this x value to only 15% of the total cross section. The major contribution, 85%, is therefore coming from the quark-antiquark annihilation processes. At a significantly higher center of mass energy of $\sqrt{s} = 14$ TeV this picture will change as there the typical value of x is approximately 0.025 at which the gluon PDF is much higher than the corresponding ones for the quarks.

The prediction of the cross section depends on the mass of the top quark and $\sqrt{s}$. It is calculated at next to next to leading order to be [16]:

$$\sigma_{t\bar{t}}(\sqrt{s} = 1.96 \text{ TeV}) = 6.77 \pm 0.42 \text{ pb} , \tag{2.23}$$

assuming a top quark mass of $m_t = 175$ GeV.

Single top quarks can be produced via the weak interaction. Also here two processes contribute to the overall cross section: production of a top quark through a s-channel

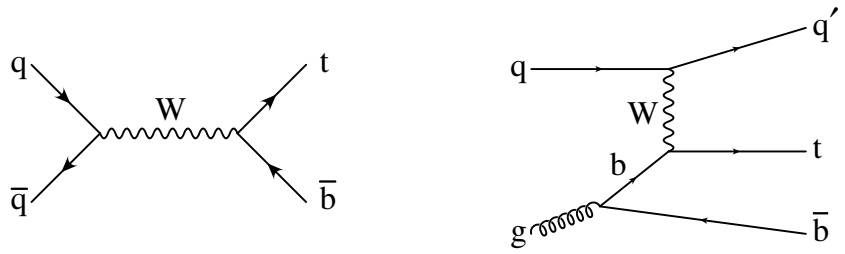

Figure 2.3: Feynman diagrams showing the electroweak production of single top quarks through an s-channel (left) and a t-channel W boson (right), where the initial b quark is produced via gluon splitting.

W boson or through a t-channel W boson. In the t-channel the b quark in the initial state is produced through a gluon splitting into a $b\bar{b}$ pair, producing an additional b quark in the final state. The Feynman diagrams for these two processes are shown in Fig. 2.3.

So far the production of single top quarks could not be observed. The theoretical prediction for the cross section of the two processes in proton-antiproton collisions at next to leading order is [17]:

$$\sigma_s(\sqrt{s} = 1.96 \text{ TeV}) = 0.88 \pm 0.14 \text{ pb} \quad (2.24)$$

$$\sigma_t(\sqrt{s} = 1.96 \text{ TeV}) = 1.98 \pm 0.30 \text{ pb} \quad (2.25)$$

2.2.2 Decay

The top quark decays via the weak interaction. Assuming only three flavors and the unitarity of the CKM matrix, the CKM matrix element V_{tb} is constraint to be close to one: $|V_{tb}| \approx 0.999$. Therefore the top quark is expected to decay almost always to a b quark and a W boson. A $t\bar{t}$ pair will therefore produce two b quarks and two W bosons. Due to the different decay modes of the W boson, the decay channels of the $t\bar{t}$ pair can be classified according to the decays of the W boson:

All hadronic: in this decay mode both W bosons decay into a quark-antiquark pair. This channel has the largest branching fraction of about 46% but suffers from a very large background from multijet production.

Lepton+jets: Here one of the W bosons decays into a charged lepton and a neutrino and the other into a quark-antiquark pair. The decays of the W boson into τ leptons where the τ decays into hadrons is normally not included as it is experimentally challenging to distinguish hadronic decays of the τ from jets. The

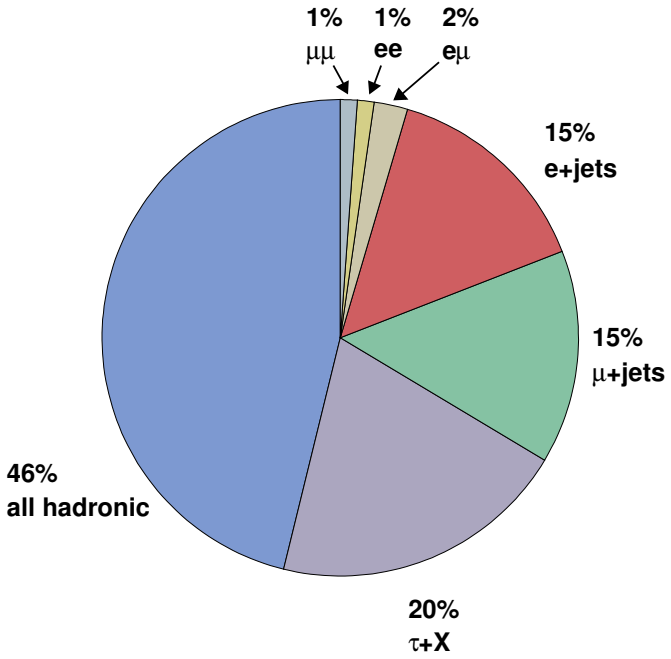

Figure 2.4: Branching fractions of the different final states from the decay of $t\bar{t}$ events. The measured branching fractions of the W boson [11] have been used to derive these numbers.

leptonic decays of the τ are however included as they are experimentally indistinguishable from direct $W \to e\nu$ or $W \to \mu\nu$ decays. Due to the presence of one charged lepton the background contamination in this channel is lower while the branching fraction is still relatively large with about 30% (excluding the decays into a τ). This channel is also referred as the "golden channel" for top physics as it provides enough statistics and a good separation from the background. The presence of only one neutrino in the event still allows for a complete reconstruction of the $t\bar{t}$ system and its decay products.

Dilepton: In this channel both W bosons decay into leptons. This provides a very good separation against the background processes leading to a clean signal. Unfortunately the branching fraction for this channel is only about 5%. The fact that two neutrinos are present in the event does not allow for a complete reconstruction of the $t\bar{t}$ system.

In Figure 2.4 a summary of the branching ratios of the different decay channels is shown.

One of the unique features of the top quark is its extremely short lifetime which is a consequence of its high mass:

$$\Gamma_t^{-1} \approx (1.5\,\mathrm{GeV})^{-1} \approx 0.4 \times 10^{-25}\,\mathrm{s}\,. \tag{2.26}$$

This is considerably shorter than the typical time to form a meson, $\Lambda_{QCD}^{-1} \approx (0.2\,\text{GeV})^{-1}$. At this stage the spin of the heavy quark is still conserved. However, on the order of $(\Lambda_{QCD}^2/m_Q)^{-1} \approx (1\,\text{MeV})^{-1}$, the spin-spin interaction between the two quarks in the meson cause the meson to evolve into a spin-zero state and thereby depolarizing the heavy quark [18]. Among the quarks, only the top decays before it has a chance to depolarize (or even hadronize). Its spin information is therefore transferred to its decay products[3].

2.2.3 Spin correlations

By measuring the spin of the top quark and/or of the top antiquark one can, for instance, check the validity of the $V - A$ expectation for the decay, $t \to Wb$, or search for non-standard CP violations in $t\bar{t}$ production and/or decay. The spin measurement is also useful in the search for new interactions [19].

The top quarks are produced unpolarized [14], however the spin of the top quark is correlated with that of the top antiquark. The strength of the correlation depends on the choice of the spin quantization axis. The following three different spin bases are commonly used:

- in the **beam basis** one of the hadronic beams is used as quantization axis;
- in the **helicity basis** the quantization axis is the direction of flight of the top quark and the top antiquark, respectively;
- in the **off-diagonal basis** [20] an axis is used which is defined by an angle ψ with respect to the beam. ψ is related to the scattering angle θ by

$$\tan\psi = \frac{\beta^2 \sin\theta\cos\theta}{1 - \beta^2\sin^2\theta}\,, \tag{2.27}$$

  where β is the velocity of the top quark and antiquark in the center-of-mass frame.

To leading order α_s, the top quark and the top antiquark produced in $q\bar{q}$ annihilation are 100% correlated in the off-diagonal basis. However, for top quark pairs produced via the fusion of two gluons a basis cannot be constructed in which the correlation is 100%. At next-to-leading order the beam basis yield almost identical results compared to the off-diagonal basis [19].

[3] It should be noted that also the spin of long-lived heavy quarks is observable if the heavy quark hadronizes into a baryon, e.g. a Λ_b.

Particle	Correlation coefficient λ	λ at $m_t = 175$ GeV
l, d or s	1	1
ν, u or c	$\frac{(\xi-1)(\xi^2-11\xi-2)+12\xi\ln\xi}{(\xi+2)(\xi-1)^2}$	-0.31
W^+	$\frac{\xi-2}{\xi+2}$	0.41
b	$-\frac{\xi-2}{\xi+2}$	-0.41

Table 2.3: Correlation coefficients λ for the decay products of a spin-up top quark as a function of $\xi = m_t^2/m_W^2$ assuming $m_b = 0$ [22].

In general the formula for the decay angular distribution of the ith decay product is [21]:

$$\frac{1}{\Gamma}\frac{d\Gamma}{d(\cos\theta_i)} = \frac{1}{2}(1+\lambda_i\cos\theta_i)\ . \tag{2.28}$$

The coefficients λ_i can be computed from the decay matrix element. For a polarized top quark they are essentially determined by the ratio squared of the two masses in the system $(m_t/m_W)^2$ (Table 2.3).

As already mentioned above, the top quarks in $t\bar{t}$ pairs at the Tevatron are essentially unpolarized: spin-up and spin-down top quarks are produced in equal numbers. However, there is an asymmetry if the top and antitop quarks are considered as pair: in general, the number of pairs where both quarks have spin up or spin down is not equal to the number of pairs where one quark is spin up and the other is spin down [21]. In this situation, correlations are visible in a joint distribution: containing one decay angle from the top side of the event and one decay angle from the antitop side of the event:

$$\frac{1}{\Gamma}\frac{d^2\Gamma}{d(\cos\theta_+)d(\cos\theta_-)} = \frac{1}{4}(1-C\cos\theta_+\cos\theta_-)\ , \tag{2.29}$$

where θ_+ and θ_- are the decay angle in the top side and the antitop side of the event, respectively.

The dependency on the chosen spin quantization axis enters in the coefficient C:

$$C = \lambda_+\lambda_-\frac{N(\uparrow\uparrow)+N(\downarrow\downarrow)-N(\uparrow\downarrow)-N(\downarrow\uparrow)}{N(\uparrow\uparrow)+N(\downarrow\downarrow)+N(\uparrow\downarrow)+N(\downarrow\uparrow)}\ , \tag{2.30}$$

where $N(\uparrow\uparrow)$ etc. denote the number of $t\bar{t}$ pairs with t and $\bar{t}$ spin parallel – or antiparallel – to the chosen spin quantization axis (Table 2.4).

From the double differential distribution it is obvious that extracting C is effectively a one-dimensional problem, with $\xi = \cos\theta_+\cos\theta_-$ as a single variable. The spin correlation shows up as an asymmetry in the distribution at $\cos\theta_+\cos\theta_- = 0$.

Spin Basis	LO	NLO
helicity	-0.471	-0.352
beam	0.928	0.777
off-diagonal	0.937	0.782

Table 2.4: Coefficient C in $p\bar{p}$ collisions at $\sqrt{s} = 2$ TeV to leading (LO) and next-to-leading order (NLO) in α_s for three different spin bases [19]. Only double leptonic decays are considered, i.e. $\lambda_+ = \lambda_- = 1$.

The asymmetry can be defined as

$$\begin{aligned} \mathcal{A} &= \frac{1}{N}\int_{-1}^{0} \frac{dN}{d(\cos\theta_+ \cos\theta_-)} d(\cos\theta_+ \cos\theta_-) \\ &\quad -\frac{1}{N}\int_{0}^{1} \frac{dN}{d(\cos\theta_+ \cos\theta_-)} d(\cos\theta_+ \cos\theta_-) \\ &= \frac{C}{4}\,. \end{aligned} \tag{2.31}$$

As can be seen from Equation 2.30, the strength of the spin correlation depends on the correlation coefficients λ_i and is therefore maximal for charged leptons or down type quarks.

2.2.4 *W* boson helicity

The W boson is a massive spin 1 particle and can therefore posses any of the following helicity state: transverse-plus ($\lambda_W = +1$), transverse-minus ($\lambda_W = -1$) and longitudinal ($\lambda_W = 0$). The relative fractions f_i ($i = -, 0, +$) of these helicity states are expressed as ratios of the rates for the production of these states:

$$f_i = \frac{\Gamma(\lambda_W = i)}{\Gamma(\lambda_W = -1) + \Gamma(\lambda_W = 0) + \Gamma(\lambda_W = +1)}\,, \quad i = (-, 0, +)\,. \tag{2.32}$$

The different helicity states reflect themselves in the angular distribution $\omega(\theta)$ of the decay products in the rest frame of the W boson [23, 24, 25]:

$$\omega(\theta) = \frac{m_t^2 \cdot \omega_0(\theta) + 2M_W^2 \cdot \omega_-(\theta) + m_b^2 \cdot \omega_+(\theta)}{m_t^2 + 2m_W^2 + m_b^2}\,, \tag{2.33}$$

where θ refers to the decay angle of the W boson decay products with weak isospin $I_3 = -1/2$ (charged lepton or d, s quark) in the rest frame of the W boson as shown in Figure 2.5.

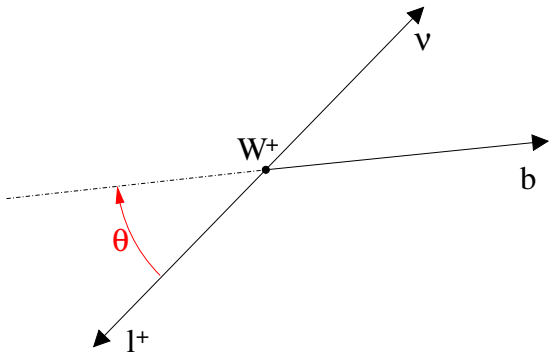

Figure 2.5: Definition of the decay angle $\cos\theta$ in the rest frame of the W boson: θ is the polar angle between the momentum vector of the charged lepton (or d, s quark) and the negative momentum direction of the b quark.

The normalized angular functions $\omega_i(\theta)$ $(i = 0, -, +)$ reflect the angular dependence of the different helicity states:

$$\omega_0(\theta) = \frac{3}{4}\sin^2\theta\,, \tag{2.34}$$

$$\omega_-(\theta) = \frac{3}{8}(1-\cos\theta)^2\,, \tag{2.35}$$

$$\omega_+(\theta) = \frac{3}{8}(1+\cos\theta)^2\,. \tag{2.36}$$

By using the helicity fractions f_i introduced previously, Eq. 2.33 can be rewritten in the following form:

$$\omega(\theta) = \frac{3}{4}(1-\cos^2\theta)f_0 + \frac{3}{8}(1-\cos\theta)^2 f_- + \frac{3}{8}(1+\cos\theta)^2 f_+\,. \tag{2.37}$$

The fraction of W bosons with longitudinal polarization, f_0, is given by [23, 24, 25]:

$$f_0 \approx \frac{m_t^2}{2M_W^2 + m_t^2} = (70.1 \pm 1.6)\,\%\,, \tag{2.38}$$

where the current values [11] for the mass of the top quark, $m_t = 174.3 \pm 5.1$ GeV, and for the mass of the W boson, $M_W = 80.425 \pm 0.038$ GeV, have been used. The mass of the b quark has been neglected in this calculation as it is done only at the Born level ($m_b \to 0$). Due to the fact, that f_0 is defined purely by the masses of the involved particles, it is independent of the exact structure of the weak charged current interaction as long as it is a linear combination of a vector and an axialvector current, e.g. $V-A$ or $V+A$.

In the standard model, i.e. in a pure $V-A$ theory, the fraction f_+ is suppressed by chiral factors of order m_b^2/m_t^2, i.e. f_+ =0 at the Born level. A next to leading order

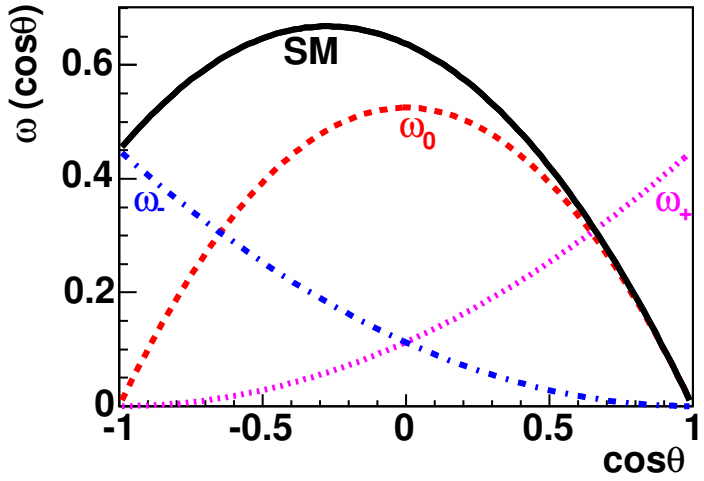

Figure 2.6: Angular functions $\omega(\cos\theta)$ for the different helicity states. The solid line shows the predicted shape of $\cos\theta$ in the standard model while the other lines show the shape from $f_i \cdot \omega_i(\cos\theta)$, $(i = -, 0, +)$ with $f_0 = 0.70$ and $f_+ = f_- = 0.30$.

calculation that includes the small mass of the b quark and radiative corrections of $\mathcal{O}(\alpha_s)$ finds the following value for f_+ in the standard model [26]:

$$f_+ = 3.6 \times 10^{-4}\,. \tag{2.39}$$

This small value for f_+ means that a f_+ value that is larger than 0.01 must originate from non-standard model contributions. As the sum of the f_i needs to add up to 1, f_- is essentially equal to $1 - f_0$.

Figure 2.6 summarizes the information on the distribution in $\cos\theta$ by showing the predicted shape for the individual ω_i as well as the shape expected in the standard model.

Even in scenarios where the weak charged current interaction of the top quark contains a $V + A$ contribution, the value of the fraction of longitudinally polarized W bosons stays unchanged. However, the fraction of left-handed W bosons is reduced in favor of right-handed W bosons. In the extreme scenario of a pure $V + A$ interaction, f_+ would be $1 - f_0$ and f_- would be suppressed by chiral factors of order m_b^2/m_t^2.

A measurement of the W boson helicity, or more precisely a measurement of f_+, can therefore probe the underlying weak interaction of the top quark decay. This measurement can reveal the influence of physics beyond the standard model if f_+ is found to be larger than 3.6×10^{-4}.

2.3 $V + A$ interaction and extensions of the Standard Model

The standard model contains only a pure $V - A$ interaction for the weak charged current interaction and so far no deviation of the $V - A$ structure has been found in any charged current interaction. With the study of the top quark, it is now possible to probe the weak charged current interaction at much higher energies.

In the following different models will be summarized that could lead to a $V + A$ contribution in the $t \to Wb$ decay.

Left-right symmetric models: The simplest way of including a $V + A$ contribution is to explicitly extend the standard $SU(2)_L \times U(1)_Y$ symmetry group to $SU(2)_R \times SU(2)_L \times U(1)_Y$. These models are described in the literature as left-right symmetric models [27, 28]. Due to the success of the standard model in low-energy phenomenology, the masses of the right-handed gauge bosons need to be significantly larger than those of the left-handed gauge bosons. However, the top quark could be heavy enough to be influenced by the right-handed sector of these models.

Supersymmetry in five dimensions: A possible model for supersymmetry (SUSY) in 5 dimensions is the $SU(4)_c \times SU(4)_{L+R}$ model described in Ref. [29]. Unlike the left-right symmetric models the left and the right part are really unified into a $SU(4)$ group.

Minimal SUSY $SO(10)$: This is again a different incarnation of the left-right symmetric model [30]. Here, the fundamental gauge group is $SO(10)$ which contains $SU(2)_R \times SU(2)_L \times U(1)_Y$. This model was developed because it can explain the small neutrino masses via the seesaw mechanism.

These three models are of course just examples of the many more models that exist, e.g. the theory of mirror fermions [31]. All models contain in one way or another just a right-handed extension of the standard model and are therefore not discussed further in this context. The magnitude of the $V + A$ contribution in these theories is essentially a free parameter.

2.4 Limit calculation

In addition to quoting a measured parameter and its uncertainty, it is useful to also give a limit on the presence of new physics that could affect this parameter. This is

especially important if there are physical boundaries on the possible values and the central value of the measurement is outside the physically allowed region.

Two different approaches are commonly used in statistical inference: a frequentist approach and a Bayesian approach. In the first approach probability is interpreted as the frequency of the outcome of a repeatable experiment. In the Bayesian approach the interpretation of probability is more general and includes the concept of *degree of belief*: a required input to the method is the so called *prior*, the a priori degree of belief about the parameters' values i.e. before carrying out the measurement.

For many problems, the frequentist and the Bayesian method are numerically very close if not identical. However, especially for small data samples and for measurements of a parameter near a physical boundary (where the prior vanishes), these methods may give different results [11]. In the following, the application of both methods to the measurement of the W boson helicity will be described.

2.4.1 Frequentist approach from Feldman and Cousins

The confidence interval construction based on the method developed by Feldman and Cousins [32] is an implementation following the frequentist approach. It is one of the procedures recommended by the Particle Data Group for bounded parameters. In the following the application of this method to the measurement of the W helicity is outlined.

The different possible values for f_+ are caused by a mixture of a $V-A$ and a $V+A$ interaction:

$$\alpha \cdot (V-A) + [1-\alpha] \cdot (V+A) \qquad \text{with } \alpha \in [0,1]. \tag{2.40}$$

Values of α outside of the interval $[0,1]$ have no physical meaning.

The measured data in an experiment consists of a histogram $N \equiv \{n_i\}$, together with an assumed known mean expected background $B \equiv \{b_i\}$ and a signal contribution $T \equiv \{\mu_i|\alpha\}$ which depends on α. Each bin i corresponds to a Poisson process:

$$P(n_i|\mu_i) = (\mu_i + b_i)^n \cdot \frac{\exp[-(\mu_i + b_i)]}{n_i!}. \tag{2.41}$$

The distribution finally obtained in the data is just one out of a large number of possible N histograms that can be built from these Poisson processes. To construct the confidence region, the large number of possible N histograms have to be ordered according to the ratio of the probabilities,

$$R = \frac{P(N|T)}{P(N|T_{best})}, \tag{2.42}$$

where $T_{best}(\alpha)$ gives the highest probability for $P(N|T)$ for the physically allowed values of α. By using $\chi^2 = -2\ln(P)$ the following equation is obtained

$$R' = \Delta\chi^2 = 2\sum_i \left[\mu_i - \mu_{best_i} + n_i \ln\left(\frac{\mu_{best_i} + b_i}{\mu_i + b_i}\right)\right]. \tag{2.43}$$

Each possible histogram N corresponds to one specific outcome of the Poisson processes, i.e. for each bin i a random number has to be drawn according to a Poisson distribution with mean $\mu_i + b_i$.

To perform the actual confidence interval calculation the following procedure is used:

- for each α a large number of MC experiments are performed and for each of these experiments $\Delta\chi^2$ is calculated. The MC experiments are fluctuated by the statistical and systematic uncertainty. The statistical uncertainty is represented by the Poisson process and the systematic uncertainty is incorporated by replacing the mean of the Poisson process with a Gaussian whose width corresponds to the systematic uncertainty.
- $\Delta\chi^2_c(\alpha)$ is calculated such that a fraction β of the simulated experiments satisfy $\Delta\chi^2 < \Delta\chi^2_c$. The set $A \equiv \{\Delta\chi^2_c(\alpha)\}$ forms the Monte Carlo acceptance for the confidence level (C.L.) β.
- $\Delta\chi^2$ for the data at each value of α, i.e. $\Delta\chi^2(data|\alpha)$, is compared with the Monte Carlo acceptance and the final confidence interval consists of all points that satisfy

  $$\Delta\chi^2(data|\alpha) < \Delta\chi^2_c(\alpha). \tag{2.44}$$

  This automatically provides the appropriate type of confidence region: a closed interval ($\alpha \in [\alpha_{lo}, \alpha_{up}]$), an upper limit ($\alpha < \alpha_{up}$), or a lower limit ($\alpha_{lo} < \alpha$).

The parameter α has to be varied within the full range of the physically allowed values, i.e. from 0 to 1.

2.4.2 Bayesian approach

The outcome of an experiment to measure the W helicity is a set x of $\cos\theta$ values, whose probability distribution depends on f_+. In Bayesian statistics, all knowledge about f_+ is contained in the posterior probability density function $p(f_+|x)$, which describes the degree of belief for f_+ to take on values in a certain region given the set x. This function can be obtained, as the name of this method already suggests, via Bayes theorem:

$$p(f_+|x) = \frac{\mathcal{L}(x|f_+)\pi(f_+)}{\int \mathcal{L}(x|f'_+)\pi(f'_+)\,df'_+}\,, \tag{2.45}$$

where $\mathcal{L}(x|f_+)$ is the likelihood function as given by the data of the experiment and $\pi(f_+)$ is the prior probability density function which expresses the experimenter's subjective degree of belief about f_+.

The confidence interval $[f_+^{lo}, f_+^{up}]$ with the confidence level β is given by the values for which the relation

$$\beta = \int_{f_+^{lo}}^{f_+^{up}} p(f_+|x)\, df_+ \tag{2.46}$$

is fulfilled.

3 Experimental apparatus

The data for this analysis is provided by two primary instruments at the Fermi National Accelerator Laboratory (FNAL): the Tevatron accelerator and the DØ detector. The Tevatron is currently, until the start of the Large Hadron Collider (LHC), the world's highest energy accelerator. It provides proton anti-proton ($p\bar{p}$) beams colliding at a center of mass energy of 1.96 TeV. The DØ detector measures the final state particles observed in these collisions.

Both instruments have been substantially upgraded since their first running period which lasted from 1988 until 1996. As this analysis is based on data from the new running period (Run II) which started in march 2001, only their current configuration is described in this chapter.

3.1 The Tevatron collider

The Tevatron accelerator is the largest accelerator at Fermilab. It is the last step in a chain that accelerates protons and anti-protons to a center of mass energy of 980 GeV each.

The acceleration chain starts with the Pre-accelerator. Hydrogen gas is used as an ion source: the electrons are first stripped off the hydrogen atoms by an electric field and then captured by the free protons. Only protons which capture 2 electrons (H^- ions) are used in the following steps. They are separated from the remaining hydrogen atoms by a magnetic field and accelerated to an energy of 750 keV using an electrostatic Cockcroft-Walton accelerator.

The next step is to accelerate the H^- ions further to an energy of 400 MeV. This is done inside the 130 m long Linear Accelerator. Afterwards the ions are passed through a thin carbon foil, that strips the electrons off the ions so that only protons remain.

The first synchrotron accelerator in the chain is the Booster. There the protons reach an energy of 8 GeV after about 20,000 revolutions and are passed on to the Main Injector. The Main Injector is also a synchrotron accelerator, whose two main purposes are: delivering protons for the anti-proton production and accelerating both protons and anti-protons to an anergy of 150 GeV.

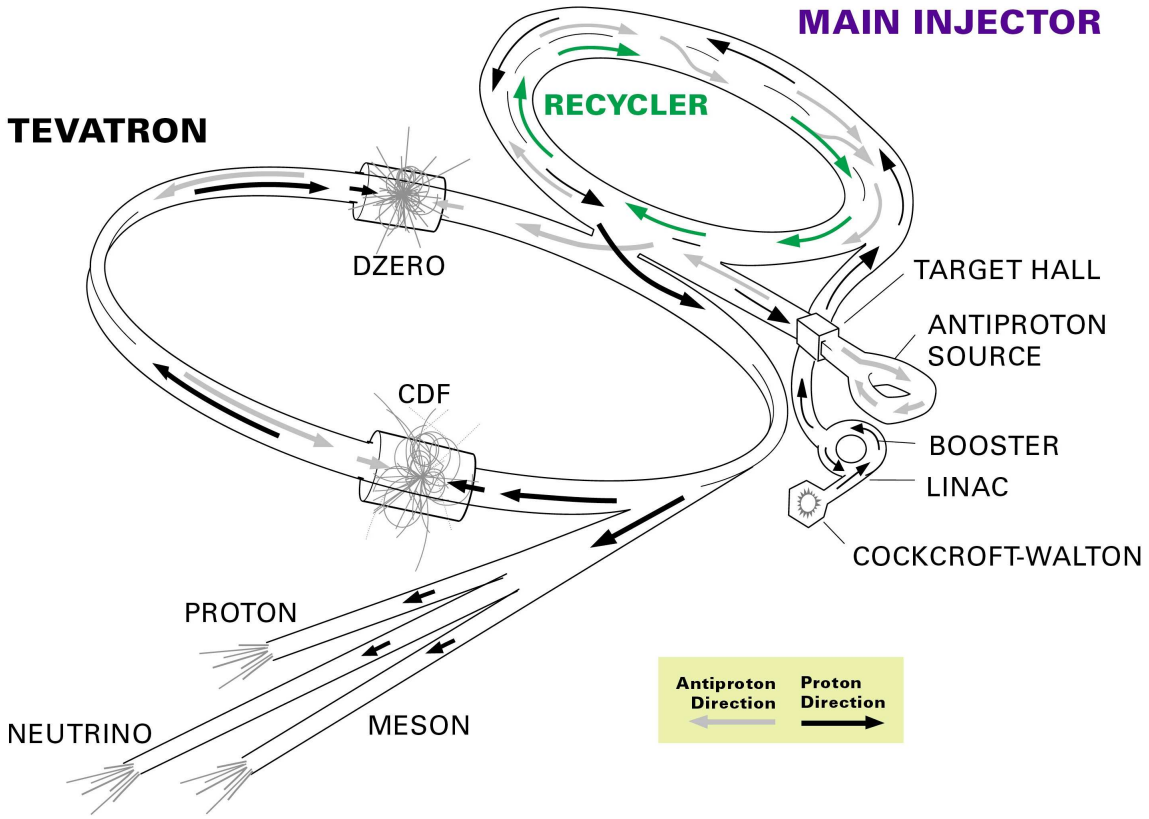

Figure 3.1: Schematic view of the Tevatron accelerator complex.

The anti-protons are produced in the Anti-proton Source. 120 GeV protons from the Main Injector are shot onto a nickel/copper target. The interaction between these protons and the target produces, among other particles, anti-protons[1]. Magnets are used to select the anti-protons which are then transferred to the Accumulator where they are stored. Every time anti-protons are needed they are transferred from the Anti-proton Source to the Main Injector.

The Tevatron receives protons and anti-protons from the Main Injector and accelerates them, in opposite directions, to an energy of 980 GeV. These beams are not a continuous flow of particles but are packed together in so called bunches (groups) of protons and anti-protons. The Tevatron operates with 36 proton and 36 anti-proton bunches.

At two different locations on the ring, called B0 and D0, the bunches of protons and anti-protons cross each other. These are the locations where the two multi-purpose detectors CDF[2] and DØ are installed. At these places the bunches are focused using quadrupole magnets to maximize the instantaneous luminosity. The time between

[1] One million protons produce on average 15 anti-protons
[2] Collider Detector at Fermilab

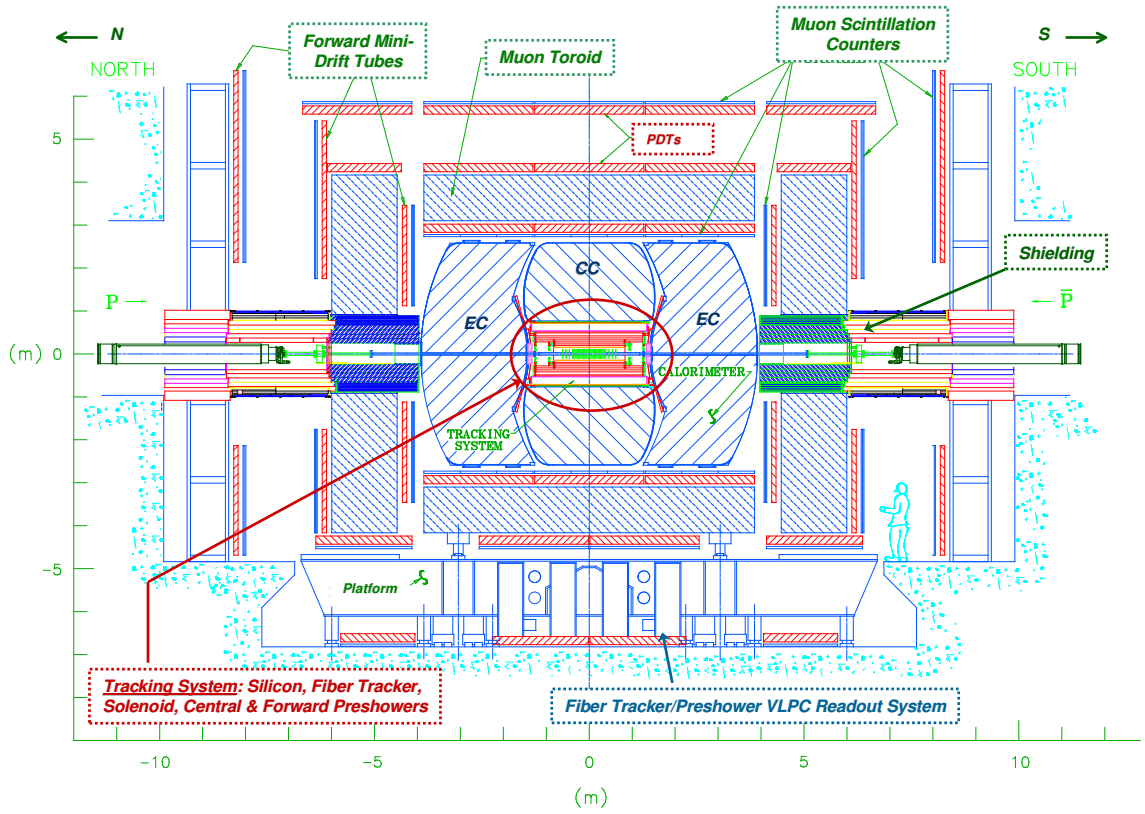

Figure 3.2: Cross section of the DØ detector.

two bunch crossings is 396 ns.

Once the two beams are brought into collision the data taking is started and lasts typically about 20 hours. At the end of the data taking the two beams are dumped intentionally. However, the anti-proton beam still contains a large amount of anti-protons at this stage. As it is tedious and time consuming to produce new ones using the Anti-proton Source the last part of the Tevatron accelerator complex was built: the Recycler. The idea is, instead of dumping the anti-proton beam, to recover the remaining anti-protons, cool them down to 8 GeV, and store them alongside those sent from the Anti-proton Source. The Recycler is currently under testing and not yet ready for normal operation.

3.2 The DØ detector

The DØ detector [33, 34] is a typical representative of multi purpose detectors for a symmetric collider. Figure 3.2 shows a cross section through the DØ detector. Multiple layers of different detector types measure various properties of the particles pro-

duced in high energy collisions. Closest to the interaction region is the tracking system, which measures the three dimensional trajectories of charged particles passing through it. It is located inside a solenoidal magnetic field to allow for momentum and charge measurement of particles. The tracking system is subdivided into two parts: a high resolution silicon vertex detector and an outer tracking system for an efficient track pattern recognition and improved momentum resolution.

The calorimeter surrounds the tracking system and measures the energies of electromagnetic and hadronic particles. It consists of three main parts: a preshower detector to precisely measure the position of the particles after the multiple scattering caused by the passage through the magnet, an electromagnetic calorimeter and a hadronic calorimeter.

Around the calorimeter is the muon system which measures the momentum of charged particles which have escaped the calorimeter and passed through the thick iron toroid magnets.

In the following sections the different subsystems are presented in more detail.

3.2.1 The DØ coordinate system

In the DØ detector a standard right handed coordinate system is used. The $+z$ axis points in the direction of the proton beam, the $+y$ axis points vertically upwards and the $+x$ axis points radially outward from the center of the Tevatron ring. Due to the symmetry of the DØ detector it is convenient to use instead of the Cartesian (x, y, z) coordinates spherical ones (r, ϕ, θ). The angle ϕ is the angle around the $+z$ axis with $\phi = 0$ being the $+x$ direction and $\phi = \pi/2$ the $+y$ direction. The polar angle θ is defined with respect to the $+z$ axis.

In hadron colliders like the Tevatron the center of mass system usually has a boost along the z-axis that is different for each collision. This boost cannot be determined due to the fact that many of the particles produced in the collision, i.e. the proton remnants, escape down the beam pipe. However, the transverse momenta of the particles that escape is negligible. Therefore the conservation of energy and momentum can still be applied in the transverse plane.

It is natural at hadron colliders to use the rapidity y instead of the polar angle θ since the rapidity y is additive in consecutive parallel Lorentz transformations. The rapidity y is defined as:

$$y = \frac{1}{2} \ln \left[\frac{E + p_z}{E - p_z} \right] \tag{3.1}$$

For highly boosted particles, where $m/E \to 0$, the rapidity y can be approximated by

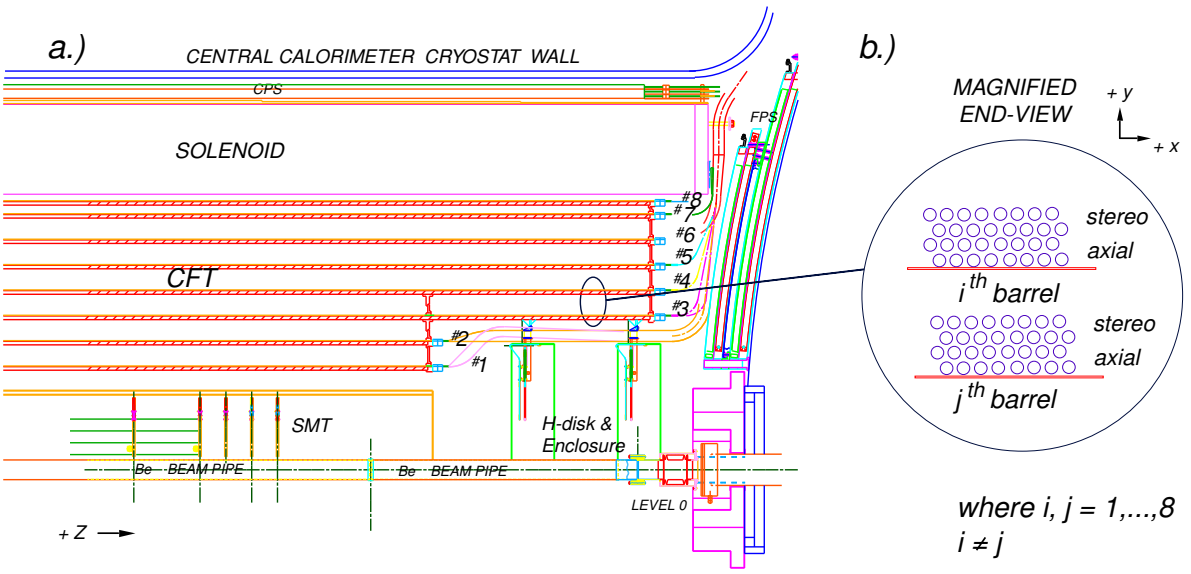

Figure 3.3: a) A quarter view of the inner tracking detectors. b) A magnified $r-\phi$ end view of the two doublet layers per barrel in the Central Fiber Tracker [35].

the pseudo-rapidity η:

$$\eta = -\ln\tan\left[\frac{\theta}{2}\right] = \operatorname{atanh}(\cos\theta) \tag{3.2}$$

3.2.2 Inner detectors

The inner detectors are surrounded by a superconducting solenoid magnet which provides a magnetic field of 2 Tesla. The magnetic field bends the path of charged particles allowing for a momentum and charge measurement. A detailed diagram of the various components of the inner tracking detectors is shown in Figure 3.3.

Luminosity system

The luminosity system measures the instantaneous luminosity being delivered to the experiment. This is done by measuring the rate of inclusive inelastic $p\bar{p}$ scattering. Most of these inelastic scatterings transfer only a small amount of momentum between the proton and the anti-proton. Hence, the resulting particles from these collisions tend to be at large values of $|\eta|$. Therefore they cannot be detected by the other subsystems as these systems measure high-energy $p\bar{p}$ collisions which in general scatter particles at a lower $|\eta|$-range, i.e. at larger angles.

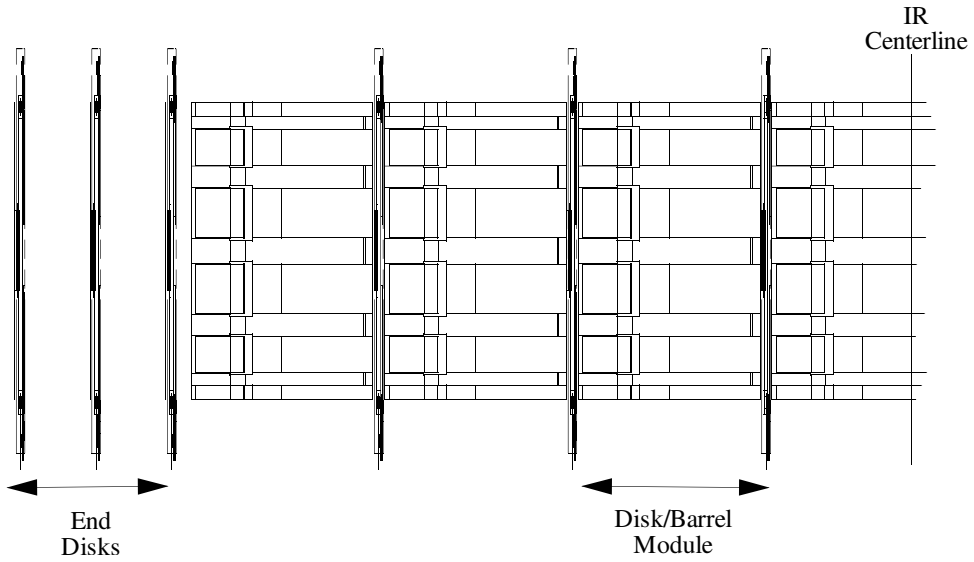

Figure 3.4: SMT interspersed barrel-disk design.

Two sets of plastic scintillator detectors are mounted on the inside face of the end-cap calorimeters, labeled "LEVEL 0" in Figure 3.3. They are arranged symmetrically in ϕ around the beam pipe, covering an $|\eta|$-range from 2.7 to 4.4. These detectors have a time resolution of less than 0.2 ns in order to be able to discriminate between particles originating from the beam halos and those from the interaction region.

Silicon Microstrip Tracker

The Silicon Microstrip Tracker (SMT) [36] is the closest subdetector to the interaction region and provides the highest resolution. Due to the larger width in z of the interaction region compared to x and y ($\sigma_z \approx 25$ cm, $\sigma_x = \sigma_y \approx 30$ μm), the SMT consists of a hybrid system, with barrel detectors measuring primarily the $r - \phi$ coordinates of the charged particles and disk detectors which measure $r - z$ as well as $r - \phi$. Figure 3.4 shows a schematic view of this hybrid system.

The six barrels surrounding the beam-pipe consist of eight layers, which are organized in doublet layers forming four super-layers. The layers have an equal spacing with an inner radius of 2.5 cm and an outer radius of 10 cm. Each barrel has a length of 12.4 cm.

Layers 1 (innermost) and 3 consist of double-sided detectors (axial and 90° stereo strips) in the central four barrel segments and single-sided detectors (axial only) in the outermost barrel segments. Layers 2 and 4 are double-sided detectors (axial and stereo strips with a stereo angle of 2°) in all the segments. Figure 3.5 shows the layout of the SMT barrel detector.

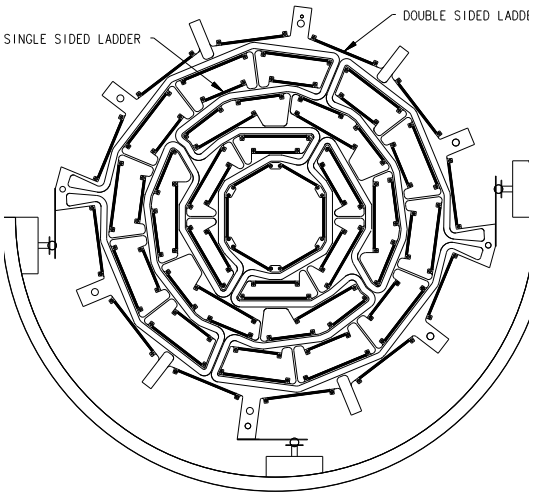

Figure 3.5: Layout of the SMT barrel detector.

Interspersed within the barrels are twelve 8 mm-thick disks ("F-disks"). Each disk consists of twelve overlapping double-sided detector wedges. The readout strips on the two sides are laid out with angles of $\pm 15^\circ$ with respect to the symmetry axis of the wedge. Hence these strips have a relative stereo angle of 30°. There are also two larger disks ("H-disks") placed at each end of the detector. Together these disks greatly extend the $|\eta|$ coverage of the silicon detector, out to about 3.0.

Beryllium bulkheads provide structural support for the detector. They are mounted on carbon fiber half-cylinders for further support. The bulkheads also function as cooling system: a water ethylene-glycol mixture flows through integrated tubes to provide the cooling.

The SMT detector has approximately $793,000$ individually readout channels with a $r - \phi$ hit resolution of approximately 10 μm.

The particle detection in this detector is based on the electron-hole pair production at a p-n junction in silicon when a charged particle passes through. The electron-hole pairs are then separated by an applied voltage and drift towards the conducting strips implanted in the silicon. The charge collected by each strip is stored in a capacitor, until it is read out and digitized by specialized electronics.

Central Fiber Tracker

Surrounding the silicon detector and extending out to the solenoid magnet is the Central Fiber Tracker (CFT) [37]. An important function of the CFT is measuring the p_T

of charged particles passing through the detector. In addition, the CFT also provides fast Level 1 track triggering in the range $|\eta| < 1.6$.

It consists of eight concentric support cylinders occupying the radial space from 20 to 51 cm. The two innermost cylinders are only 1.7 m long while the outer six are 2.5 m long. This is due to the increased space requirements of the silicon H-disks compared to the SMT barrel. Each cylinder of the CFT is totally covered by two doublet layers of scintillating fibers as shown in Figure 3.3.

A doublet layer consists of two mono layers which are displaced by half of the fiber spacing to provide a complete coverage. The innermost doublet layer is mounted along the axial direction and the second doublet layer has a stereo angle of $\pm 3^\circ$. The sign of the stereo angle changes with each cylinder, providing the following layer pattern from the innermost to the outermost barrel: $xu - xv - xu - xv - xu - xv - xu - xv$, where x is an axial layer, and u and v are the stereo layers with $+3^\circ$ and -3° stereo angles, respectively.

In total the CFT consists of 76,800 scintillating fibers. Each scintillating fiber is 835 μm in diameter, composed of a 775 μm scintillating core surrounded by a coating with a high index of refraction providing total internal reflection. They are between 1.66 and 2.52 m long, depending on the cylinder of the CFT. One end is connected to transparent waveguides, which carry the produced photons $8 - 11$ m to the Visible Light Photon Counters (VLPC), where the photons are detected. The other end of each fiber is coated with an aluminum mirror to reflect the photons.

A charged particle passing through a fiber produces on average 10 photons, that are transported via the waveguide to the VLPCs. A VLPC is an arsenic-doped silicon avalanche diode with a quantum efficiency of over 80%. The VLPCs need to be operated at a temperature of 9K. Their fast rise time, the high gain of 50,000 electrons per converted photon and the high quantum efficiency make them ideally suited for this application, for which they were specifically developed [38].

3.2.3 Calorimetry

After the momentum and the charge of charged particles has been measured by the tracking detectors, the energy of particles is measured using the preshower detectors as well as the electromagnetic and hadronic calorimeter. These detectors are located outside the solenoid.

Preshower

The main purpose of the preshower detectors, the Central PreShower (CPS) as well as the Forward PreShower (FPS), is to enhance electron and photon identification

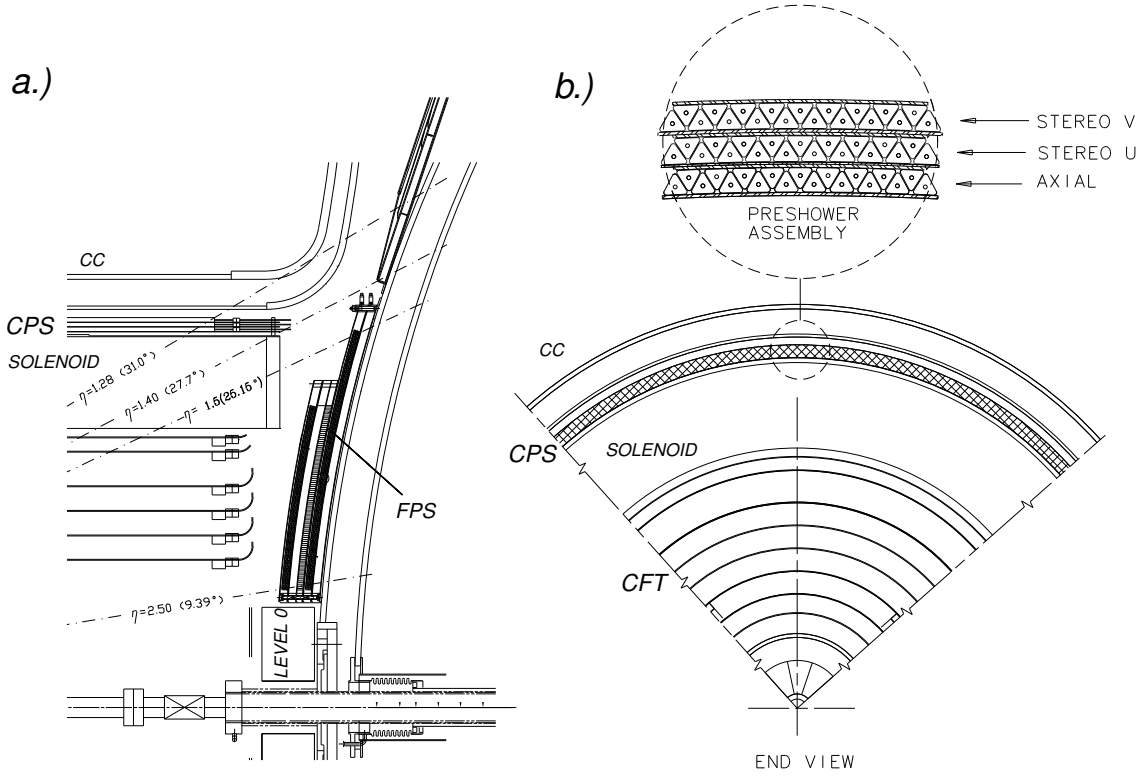

Figure 3.6: a) The location of the preshower detectors CPS and FPS inside the DØ detector. b) An $r - \phi$ view of the CPS with a close-up showing the three layers of triangular shaped scintillating fibers [35].

and to provide early energy sampling for particles having just traveled through the solenoid. Since the solenoid contains large amounts of dense uninstrumented material, the preshower detectors help to account for electromagnetic energy otherwise lost. The energy measurement is not the only task of the preshower detectors. Their position information is precise enough to act as a tracking detector.

The CPS [39] is cylindrical in geometry with a radius of 72 cm and covers the region $|\eta| < 1.2$. It is installed in the 51 mm gap between the solenoid coil and the cryostat of the central calorimeter as shown in Figure 3.6. It consists of three concentric cylindrical layers of triangular shaped scintillating strips. The innermost layer is axially oriented while the two outer layers are arranged at stereo angles of $\pm 23^\circ$. Wavelength shifting fibers embedded in the center of the triangles pass the photons through waveguides to VLPCs. The CPS has a total of 7,680 channels.

The FPS [40] resides in the forward regions at $1.4 < |\eta| < 2.5$. It is the counterpart to the CPS and is mounted on the two inner faces of the end calorimeter cryostat

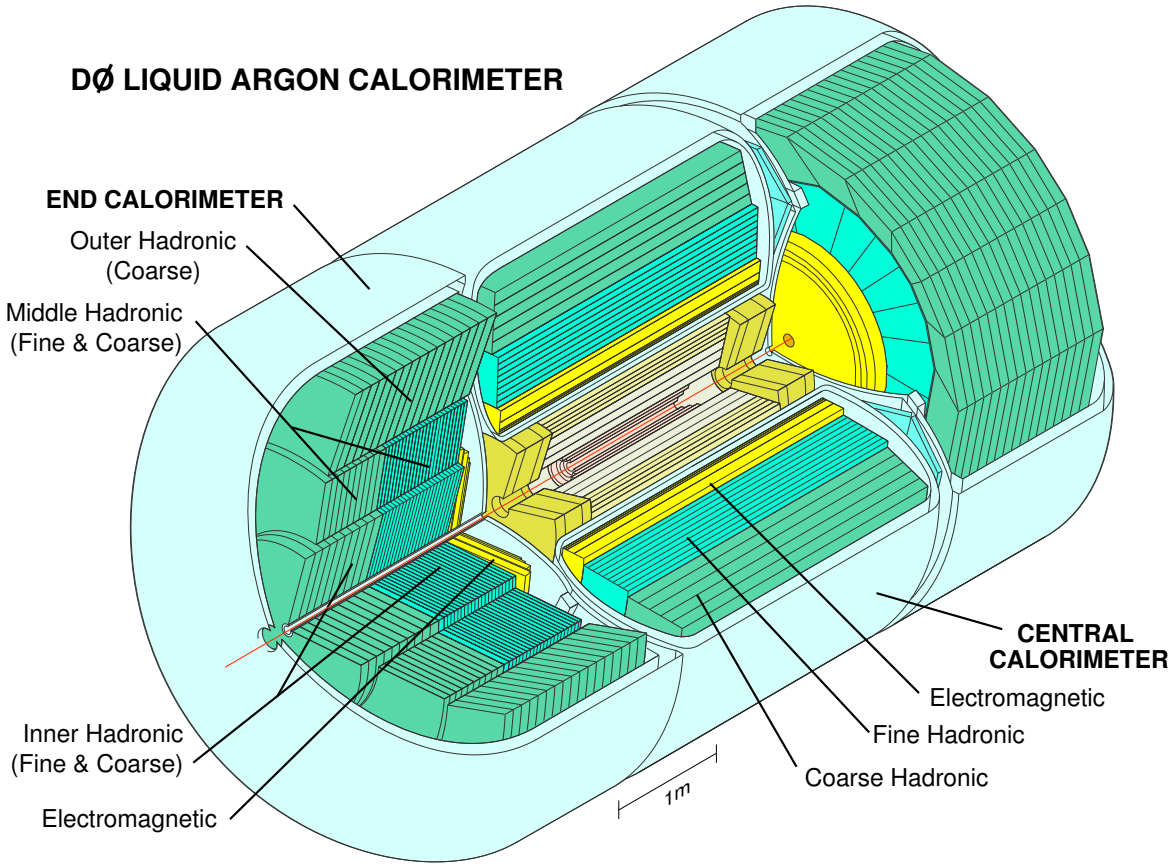

Figure 3.7: Overview of the DØ liquid argon calorimeter.

(Fig. 3.6). It uses the same triangular strips as in the CPS for the active scintillating layers and contains two scintillator planes, each plane consisting of two layers.

Between the two planes is a lead absorber layer of 2 radiation length. The function of the lead absorber is to initiate showers of electrons and photons traversing it.

As in the CPS, clear fibers are connected to the FPS for routing the produced photons to the VLPCs for readout. In total the FPS contains 14,968 channels.

Calorimeter

The DØ calorimeter uses liquid argon as active medium and has a coverage up to $|\eta| \approx 4$. To allow access to the central detector regions the calorimeter is divided into three separate parts: the Central Calorimeter (CC) and the two Endcap Calorimeters (EC). Each part is contained in a separate cryostat. Figure 3.7 shows an overview of the calorimeter. The central calorimeter covers the region of $|\eta| < 1.2$ and the endcaps extend this region up to $|\eta|$ of about 4.

Each part is again divided into three sections: the electromagnetic section (EM) closest to the interaction point, the fine hadronic section (FH) in the middle and the coarse hadronic section (CH) around it.

The DØ calorimeter is a highly segmented sampling calorimeter. The shower development of incident particles is periodically sampled via the ionization of liquid argon. The individual layers are interspersed with layers of depleted uranium 238, copper or steel, used as absorber material. The segmentation of the calorimeter in the transverse and longitudinal directions allows to measure the shape of the shower development.

Between the absorber plates are the readout pads and a gap filled with liquid argon. Figure 3.8 shows the schematic structure of a calorimeter cell. An electric field is created by applying a high voltage of $2.0 - 2.5$ kV between the signal board and the grounded absorbers. Particles passing through the cell shower in the absorber plates and the particles from the shower ionize the liquid argon gap. The liberated electrons drift towards the signal boards where they are detected.

The identification of electromagnetic and hadronic particles is based on the different shapes of the showers created by these objects.

Electromagnetic calorimeter

Electromagnetic particles interact primarily via the following processes: pair production ($\gamma \rightarrow e^+e^-$) and bremsstrahlung ($e \rightarrow e\gamma$). The energy of the original particle is exponentially decreased by a sequence of these processes:

$$E(x) = E_0 \cdot e^{-x/X_0}\,, \tag{3.3}$$

where E_0 is the original energy of the particle, x is the traveled distance and X_0 is the radiation length of the material being passed through.

The whole electromagnetic part of the calorimeter corresponds to a depth of 20 radiation lengths. It is arranged in four layers (EM1 through EM4) of cells with size $\eta \times \phi = 0.1 \times 0.1$, except for the third layer (EM3) which has twice the granularity ($\eta \times \phi = 0.05 \times 0.05$) since the maximum of the electromagnetic shower is expected there. This allows for an improved measurement of the shower shape. In the electromagnetic calorimeter only uranium 238 is used as absorber material.

Hadronic calorimeter

Hadronic particles interact with the uranium nuclei via the strong force. This interaction produces secondary particles, about a third of which are π^0s. Only the π^0s produce photons while all the other particles interact strongly. The showers produced in strong interactions tend to develop over longer distances and are broader than the

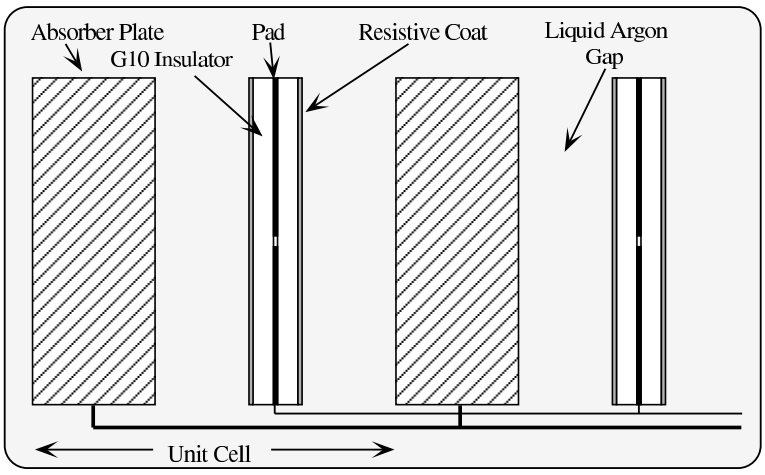

Figure 3.8: Schematic structure of a calorimeter cell.

electromagnetic ones. In analogy to the radiation length for electromagnetic particles, a nuclear interaction length λ_0 is defined for hadronic particles.

The hadronic calorimeter surrounds the EM calorimeter in both regions, CC and EC, and its thickness in nuclear interaction length varies between $7-9$. The central hadronic calorimeter is subdivided into four layers: three Fine Hadronic (FH) and one Coarse Hadronic (CH). The EC is divided into three sections: the Inner Hadronic (IH), the Middle Hadronic (MH) and the Outer Hadronic (OH). Each section is again longitudinally divided into layers: the IH is divided into four FH layers and one coarse hadronic, the MH ring, which surrounds the IH section, consists of four FH layers. Finally the OH ring surrounds the MH ring and contains three layers. The absorber material in the FH layers is uranium 238 while in the CH copper and steel is used.

The transverse segmentation of all hadronic modules is $\eta \times \phi \approx 0.1 \times 0.1$.

Intercryostat detector

The regions between the central and endcap calorimeters contain a large amount of uninstrumented material, e.g. the walls of the cryostats and support structures. To partly compensate for the energy loss in these structures, the InterCryostat Detector (ICD) has been installed [41]. Figure 3.9 shows the location of the ICD between the CC and the EC.

The ICD partly restores the energy resolution by providing an additional sampling in this region. It is made of a single layer of 384 scintillating tiles with a size of $\eta \times \phi = 0.1 \times 0.1$ to match the size of the calorimeter cells. The signal is collected using wavelength shifting fibers and transmitted through clear waveguides to photo-

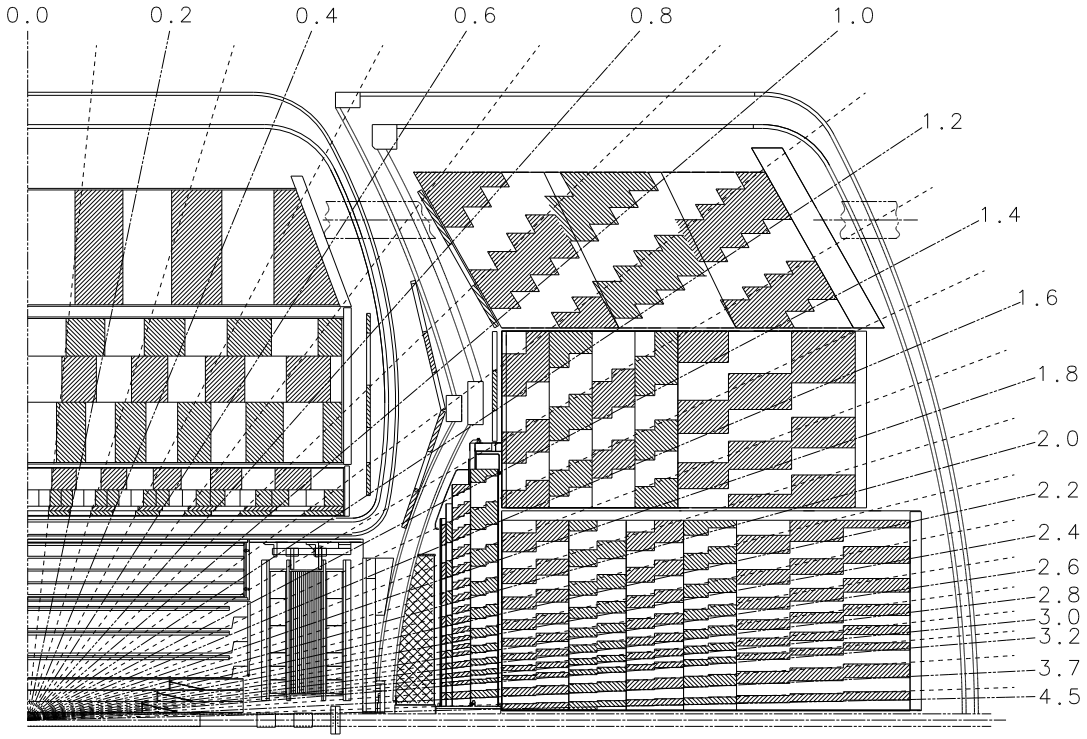

Figure 3.9: A side view of the calorimeters. The central calorimeter extends to $|\eta|$ of about 1.2 and the end-cap calorimeters cover $|\eta|$ up to about 4.0. The regions between the calorimeters, the Inter-Cryostat-Regions (ICR), are covered by special detectors, such that the coverage is nearly hermetic.

multiplier tubes located outside of the magnetic field.

Additionally, there are separate single calorimeter-like readout cell structures, so called massless gap detectors, installed in both the CC and EC calorimeters. Combining the ICD and the massless gap detectors with the CC and the EC, the coverage up to $|\eta| \approx 4$ is nearly hermetic.

3.2.4 Muon system

The outermost and physically largest detector is the Muon System. Figure 3.10 shows the four major parts of the muon detector: a central Wide Angle Muon Spectrometer (WAMUS) covering $|\eta| < 1$, a Forward Angle Muon Spectrometer (FAMUS) covering $1 < |\eta| < 2$, a 1.8 Tesla toroidal iron magnet and shielding material. The actual detector consists of three layers of drift tubes called A,B and C layer (from inside out).

The toroidal magnet separates the A-layer from the B- and C-layers bending the tra-

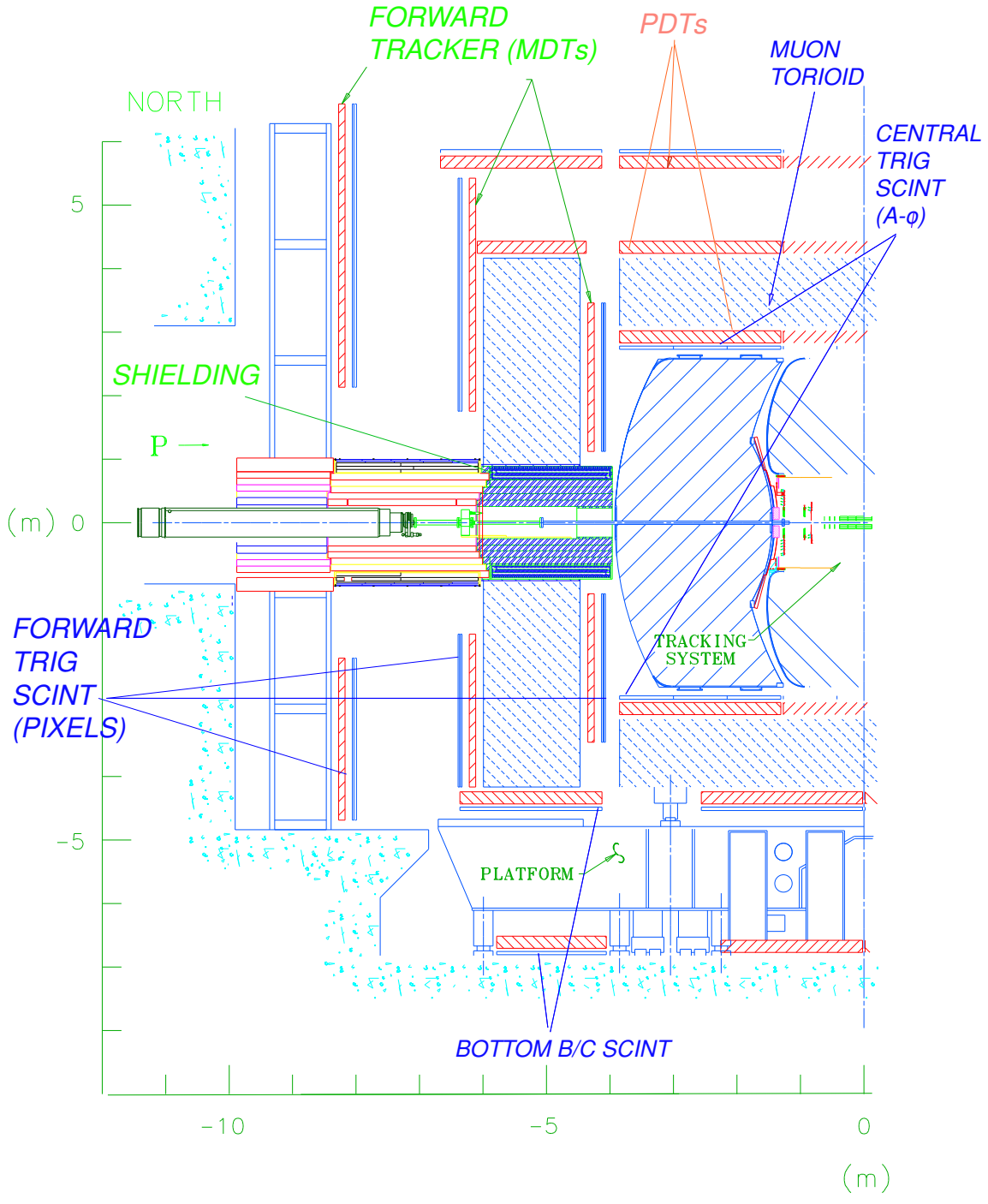

Figure 3.10: $r - z$ view of the DØ muon system [35]

jectories of charged particles in the $r - z$ plane.

Two types of drift tubes are used: proportional drift tubes (PDT) in the WAMUS and mini drift tubes (MDT) in the FAMUS. The drift tubes are filled with gas which is ionized by the particles passing through it. The resulting charge is collected on high voltage sense-wires running through the volume. The wires are oriented along the magnetic field lines in order to provide a position measurement for momentum determination

In addition two layers of scintillator are added inside the A-layer (A $-\phi$ layer) and outside of the C-layer (cosmic cap). The purpose of the A $-\phi$ layer is to provide a ϕ measurement for matching with the tracking detectors and the purpose of the cosmic cap is mainly to identify cosmics.

In the forward region, all the three layers of muon chambers are covered with a layer of scintillating pixels which have a segmentation of $\eta \times \phi = 0.12 \times 0.08$ for the outer nine rows of counters and 0.07×0.08 for the innermost two.

The muon system also contains a series of 50 cm thick iron and 15 cm thick polyethylene shielding with 5 cm thick lead skins. This shielding surrounds the beam pipe in the forward region ($2.5 < |\eta| < 3.6$) behind the cryostat wall of the EC. The purpose of the shielding is to reduce the background from interactions of the beam with the quadrupole magnets and the beam pipe.

The only observable particles which can easily pass large amounts of material are muons. At multi-GeV energies they behave as minimum ionizing particles, leaving a typical signature in the calorimeter: around 3 GeV of energy evenly spread over the path of the muon inside the calorimeter.

To reach the outer muon system particles must traverse the $7 - 9$ interaction lengths of the calorimeter and the $1 - 2$ interaction lengths of the toroid. This reduces the leakage of hadronic particles into the muon system to a very low level.

3.3 The DØ trigger system

As described earlier, interactions occur every 396 ns, which is orders of magnitude faster than events can be readout and stored. The reconstruction and space constraints restrict the data taking rate to about 50 Hz. Therefore a solution is necessary to pick only the potentially interesting events from all the rest.

The DØ trigger system [42] is a combination of hardware and software elements. It is organized in three main levels: Level 1 (L1) and Level 2 (L2) are hardware based while Level 3 (L3) is a software filter. Figure 3.11 shows the information flow in the first two trigger levels.

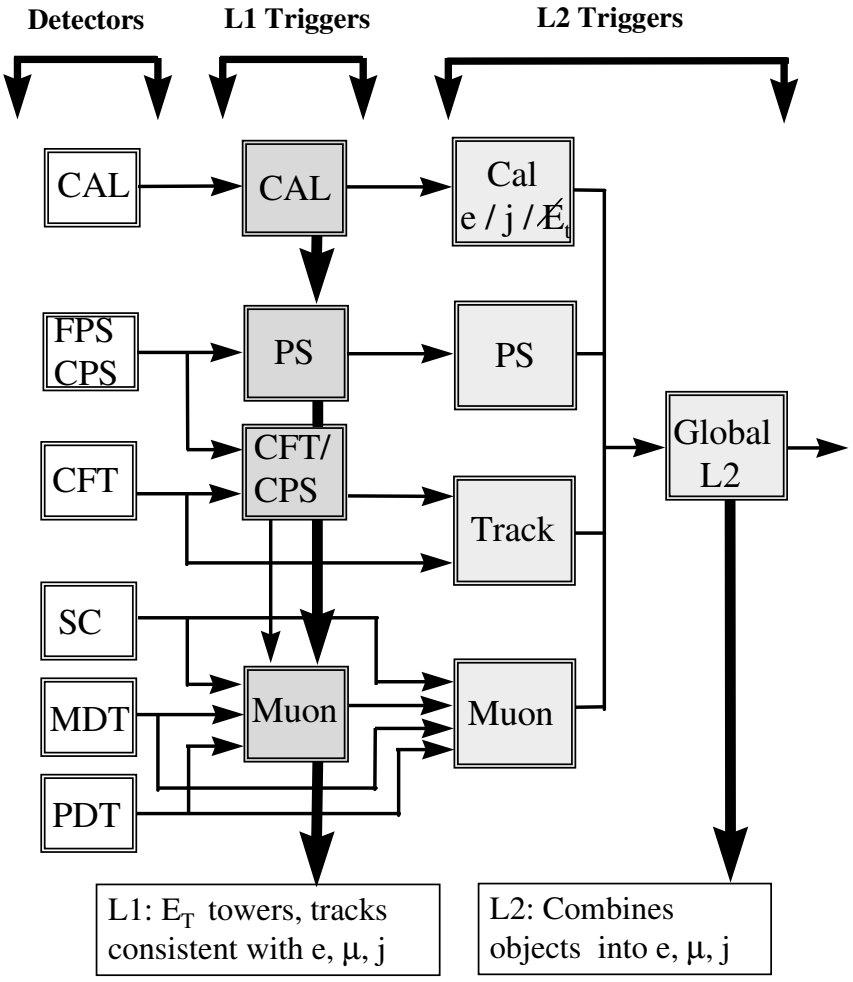

Figure 3.11: Schematic overview over the information flow, indicated by horizontal arrows, in the first two levels of the trigger system [42]

Level 1

The Level 1 trigger system consists of a series of Field Programmable Gate Arrays (FPGAs) which utilizes raw information from the individual subdetectors to decide if an event is accepted or rejected. These decisions are based on the fast readout of the muon system, the calorimeter and, in a later period, the CFT and preshower detectors. Tracks in the muon system or objects in the central tracker and in the calorimeter which are consistent with physics objects are so called L1 And/Or terms. Based on the presence of individual L1 And/Or terms, e.g. the presence of an energy deposition in the calorimeter above a certain energy threshold, the event is sent to Level 2 or discarded. The decision is issued 4.2μs after a beam-beam crossing.

Level 2

The Level 2 trigger reduces the event rate further by using multi-detector correlations of objects found in the event, e.g. spatial correlations between track segments, preshower depositions, and calorimeter energy depositions. The L2 trigger consists of two stages: the preprocessor stage and the global processor stage. Both stages are implemented in software running on dedicated processors, so called alphas or betas.

In the preprocessor stage each detector system separately builds a list of trigger information. The condensation of information, a few hundred to a thousand bytes from each subsystem, allows rapid transmission of the information to the global processor. There a decision to accept or reject an event is made within 100 μs. The event rate is reduced to 1 kHz due to this trigger level.

Level 3 Trigger and data acquisition

The Level 3 trigger [43] is a software based trigger that runs on single board computers, i.e. normal desktop computers shrunk to fit on a single board. This trigger also acts as data acquisition system transporting fully digitized data from the detector subsystems to L3 trigger filter processes running on the L3 trigger farm. There the events are reconstructed using a simplified version of the offline reconstruction software. These reconstructed events are then processed by event filter algorithms to get to the trigger decision.

The accept rate of the L3 trigger system is up to 50 Hz, depending on the chosen trigger list and instantaneous luminosity. The accepted events are then stored on tape, accessible for the offline event reconstruction.

4 Object definition and reconstruction

The events recorded by the DØ detector are initially just a large set of digital and analog signals. These signals need to be processed through higher level algorithms in order to convert them into physics objects which can be used in different analyses. These algorithms are incorporated into the DØ event reconstruction program `dØreco`.

The reconstruction of physics objects can be divided into the following three major steps:

- **Unpacking and hit finding.** In this step the raw data from the detector is unpacked and converted into hits of given spatial location and/or definite energy. These hits can be for example spatial points in the tracking detectors, hits in calorimeter cells leaving certain energy, etc.

- **Formation of lower level physics objects.** Several hits in the same subdetector are combined, e.g. local track finding in the muon system or clustering of energy cells in the calorimeter.

- **Reconstruction of higher level physics objects.** Electrons, muons or jets are identified by combining the lower level physics objects found in the previous step.

In the following sections the reconstruction steps are described starting from tracks over jet finding, particle identification up to the reconstruction of primary and secondary vertices, which allow the tagging of events with one or more b quarks.

4.1 Tracks

The first step in the reconstruction of tracks is the reconstruction of the hits in the individual tracking detectors, followed by the formation of clusters, which are then used by the track finding algorithms.

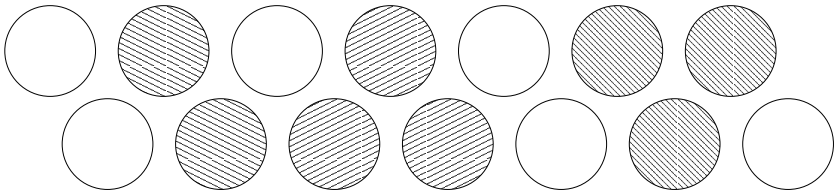

Figure 4.1: Schematic view of one double layer of the CFT showing the offset between the two single layers. The open circles represent non-hit fibers and the hatched circles the fibers that are hit. The different clusters built out of them using the standard cluster algorithm are marked with different hatch styles.

4.1.1 SMT hits and clusters

A hit in the SMT represents the energy deposit above threshold in a single silicon strip. Clusters of SMT hits are formed by combining adjacent SMT hits. The center of the cluster in a coordinate x is defined as the charge-weighted average of the strip positions in the cluster:

$$x = \sum_i x_i \cdot c_i \ , \tag{4.1}$$

where x_i is the position of the center of hit i and c_i is the charge associated with this hit. The sum runs over all hits in the cluster.

4.1.2 CFT clusters

The standard cluster algorithm in the CFT is a simple nearest neighbor algorithm. It starts at a hit fiber and adds all the adjoint hit fibers until a not-hit fiber is found (Figure 4.1).

As part of this Ph.D. thesis an alternative cluster finding algorithm has been implemented [44]. The new algorithm reduces the inefficiencies due to the reconstruction of unphysically large clusters by creating only clusters with a maximum size of two hits (more hits are physically not possible for tracks that pass through the whole CFT). The basic principle is to split up the large clusters into smaller ones. As it is not possible to decide a priori where to split a cluster, all two-hit combinations are considered (Figure 4.2).

In the standard algorithm the cluster position is simply defined as the geometrical center of the cluster. This can be improved for CFT clusters of size two, so called CFT doublets, by using the information about the deposited energy in the single CFT fibers as weights:

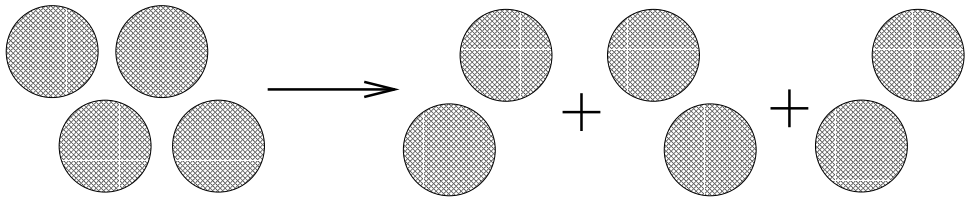

Figure 4.2: A cluster of 4 Fibers in the CFT from the standard cluster algorithm is split into 3 new clusters. The split clusters overlap to keep all possible doublets.

$$x = \frac{\omega(E_l) \cdot x_l + \omega(E_r) \cdot x_r}{\omega(E_l) + \omega(E_r)} \qquad \omega(a) = \sqrt[3]{a} \tag{4.2}$$

where x_l and x_r are the positions of the left and right CFT fiber and E is the deposited energy in the corresponding fiber. Since the energy deposit follows a Landau distribution, it was found that the optimal performance is obtained by using a weighting function ω. Using the new method the position resolution is improved by about 10% [44].

4.1.3 Track reconstruction

The track reconstruction consists of two steps: in the first step clusters are identified which correspond to single particle trajectories (track finding). The second step takes these cluster measurements and determines the kinematic track parameters (track fitting).

The track finding is done using two separate algorithms: a Hough transform based histogramming technique (HTF) and an alternative algorithm (AA). Both algorithms are run individually and the result is later combined removing duplicate tracks.

HTF

The basic idea of the HTF algorithm [45] is the following: for trajectories coming from the interaction region, every pair of points in coordinate space (x, y) corresponds to a compact area in parameter space (ρ, ϕ), where $\rho = qB/p_t$ is the curvature. The size of the compact area is given by the uncertainties of the measurement. Without the uncertainties it would be just a single point in the parameter space.

A 2D histogram representing the parameter space is created and for every pair of hits the contents of cells intersecting with the compact area is increased. Since all hits from the same track refer to the same cell in the histogram, tracks will produce a peak in

the histogram, whereas random combinations of hits will give a randomly distributed background.

HTF uses an improved version of this simple algorithm using Hough transformations to reduce the time consumption of the algorithm.

AA

The second algorithm, AA [46], uses a build-up technique. It starts by constructing all possible track hypothesis using 3 hits in 3 different layers. Given the selected parameters of the algorithm, e.g. the minimum allowed p_T, only those track candidates are kept which match these criteria. These seed tracks are either constructed in the SMT or in the CFT.

In the next step these track candidates are extrapolated to the next layer in the tracking detectors and an expectation window is calculated based on the parameters of the given candidate. Any hit found in this expectation window is associated with this candidate if the resulting increase in the χ^2 of the track fit is below a tunable threshold. If more than one hit per layer can be associated to this candidate then all new resulting candidates are kept.

Kalman track fit

After the final track candidates have been selected by the track finding algorithms a Kalman track fit [47] is performed to determine the final track parameters and errors. The interacting propagator, which knows how to propagate tracks in the DØ tracker (including their uncertainties), taking into account magnetic curvature and interaction with detector material, is the key element of the Kalman track fit.

By using this propagator, the Kalman track fit is able to propagate a given track candidate to the surfaces of the different hits and to properly recalculate the parameter and the error matrix for this track. Once all hits have been added the final track is obtained.

The final output is a list of reconstructed track helices parameterized at the distance of closest approach to the origin (dca). Each track is described by the following parameters:

- distance of closest approach, dca,
- z coordinate at the dca,
- azimuthal angle ϕ at the dca which is defined as the angle between the transverse momentum at the dca and the x-axis,

- dip angle $\tan\lambda$ which measures the slope of the helix: $\pi/2 = \lambda + \cos^{-1}(dz/ds)$ where s is the path length along the helix,
- curvature e/p_T, where e is the charge of the track.

4.2 Vertices

After the tracks have been found, it is possible to reconstruct the origins of these tracks, the vertices. First the so called primary vertices (PVs) are reconstructed. These correspond to the production of particles like the production of $t\bar{t}$ pairs (hard interaction). An important point is to not consider tracks from inelastic $p\bar{p}$ collisions (minimum bias interaction).

After all primary vertices have been found, the reconstruction of secondary vertices (SVs) is performed. These vertices correspond to the decay of particles, e.g the decay of B hadrons. These vertices are produced after the corresponding particle traveled a certain distance. Therefore the secondary vertices can be identified by looking at vertices that are significantly displaced with respect to the primary vertices.

4.2.1 Primary vertex

Two different algorithms [48] are used to reconstruct primary vertices. One is implemented into the global reconstruction program `dØreco` and the other one is in a separate package called `dØroot`. These algorithms share the vertex selection procedure but differ in the track selection and fitting techniques.

The reconstruction of the primary vertex is done in two steps: the first step applies loose track selection cuts and forms a first set of candidate vertices. This set basically determines the position of the beam spot. The second step tightens the cuts on the tracks and refits the vertices based on the location of the beam spot found in the first step.

The `dØroot` algorithm, in addition, uses a z-clustering to identify tracks belonging to different interactions. This clustering is performed before the first step. It starts from the track with the highest p_T and adds the closest track which is within 2 cm from the first one. The position of the cluster of tracks is recalculated with every additional track. The resulting clusters of tracks are then used as input to the two step process described above.

The selection of the hard scatter primary vertex is done using a probabilistic method which assigns a probability that a reconstructed vertex comes from a minimum bias interaction. This probability is calculated from the individual probabilities of the

Track variable	dØreco	dØroot
p_T	$\geq$ 0.5 GeV	$\geq$ 0.5 GeV
SMT hits	$\geq$ 2 (Data) $\geq$ 0 (Monte Carlo)	$\geq$ 2
$dca/\sigma(dca)$	$\leq$ 5.0	$\leq$ 3.0

Table 4.1: Track selection cuts used by the different algorithms for the second step of the vertex reconstruction.

tracks assigned to this vertex. A track from a minimum bias interaction has on average a smaller transverse momentum than a track from a hard interaction.

Table 4.1 lists the track selection cuts used by the different algorithms for the second step of the vertex reconstruction.

The performance of both algorithms has been extensively tested on both Monte Carlo and data [48]. In general data events, the average number of tracks attached to the primary vertex is 20 and the efficiency to find a primary vertex is 98%. Including the measured beam spot size of 37 microns in both x and y, the x,y resolution of the primary vertex is 38 microns. This agrees well with the primary vertex resolutions (excluding the beam spot) found in $t\bar{t}$ Monte Carlo events of 11 microns.

4.2.2 Secondary vertex

The main purpose of secondary vertex reconstruction is to allow for the identification of B hadron decays from the signature of several tracks emanating from a common point displaced from the primary interaction. However, the reconstruction of secondary vertices can also be used to reconstruct other long lived particles like K_S^0 and Λ (usually called V0s).

The secondary vertex algorithm [49, 50, 51] starts by reconstructing track-jets to simplify the search for secondary vertices. Only in these track-jets the secondary vertices are reconstructed.

Track-Jet reconstruction

The motivation to first reconstruct track-jets is the following: first of all it significantly reduces the number of tracks that are fed into the vertex algorithm and it reduces the influence of fake or unrelated tracks. Furthermore the vertex reconstruction is decoupled from the calorimeter information which only provides 2D association between calorimeter jets and tracks. The track-jets are 3D objects and are therefore much less sensitive to minimum bias interactions.

The following algorithm is used to reconstruct track-jets:

- Tracks are clustered into pre-clusters according to their z position of closest approach with respect to $z = 0$. The tracks are ordered by p_T and then, in descending order of p_T, added to the cluster if the Δz between the cluster and this track is less than 2 cm.
- The primary vertex corresponding to this pre-cluster is selected by choosing the one with the highest multiplicity within 2 cm of the pre-cluster. Then the following quality cuts are applied to the tracks (calculated with respect to the selected primary vertex):
  - at least 3 hits in the SMT
  - $p_T > 0.5$ GeV
  - $|dca| < 0.15$ cm
  - $|z_{dca}| < 0.4$ cm
- For every pre-cluster of selected tracks, the tracks are clustered in the (η, ϕ) plane using a simple cone jet algorithm which basically combines in a jet all tracks lying within a πR^2 area in (η, ϕ) space, where $R = 0.5$ is the chosen cone size. Only pre-clusters where the highest track p_T is above 1 GeV are considered. A more detailed description of jet algorithms can be found in section 4.3.2 on page 49.

Vertex finding

The search for a secondary vertex is performed separately for every track-jet with at least two selected tracks. Only tracks with at least 2 hits in the SMT, $p_T > 0.5$ Gev, $|dca| < 0.15$ cm and $|z_{dca}| < 0.4$ cm are used. To be able to reconstruct secondary vertices the tracks from these vertices need to be displaced with respect to the primary vertex. Therefore an additional requirement on the tracks is imposed: the impact parameter significance $S = dca/\sigma_{dca}$ should be larger than three.

The secondary vertex algorithm is a build up algorithm and works as follows:

- Seed 2-track vertices are built by fitting all combinations of pairs of selected tracks in the given track-jet.
- Additional tracks are attached to these seed vertices according to the resulting χ^2 of the vertex.
- The previous step is repeated until no more tracks can be associated to the seeds.

A track is allowed to be attached to more than one seed vertex. Therefore the presence of fake vertices does not impact the vertex finding efficiency.

4.3 Jets

The majority of events produced in $p\bar{p}$ collisions contain collimated sprays of hadrons called jets. These jets originate from quarks and gluons produced in the hard process and subsequent decays, e.g. $t \to Wb$ and $W \to q\bar{q}$. Historically, these jets are measured with the calorimeter only at detectors for $p\bar{p}$ collisions. This is still the case for the analysis presented in this thesis. However, as the charged particles from these jets are also measured with the inner tracking detectors, an improved jet reconstruction can be obtained by using both measurements simultaneously [52].

As jets are objects with a sizeable geometrical spread in the calorimeter, they are also affected by noise effects in the calorimeter. A special algorithm is used which tries to minimize these effects.

The reconstruction of the jets is then done using special jet finding algorithms. These algorithms need to identify the calorimeter cells which belong to a given jet. Two different approaches are commonly used: either select the cells by assuming a conical form of the jets, so called cone algorithms, or select the cells based on their relative transverse momentum k_T with respect to each other, so called k_T algorithms. The cone algorithm is conceptually simpler and is the one that is used for all current analyses at DØ including this one. However, the k_T algorithm is supposed to provide a better jet reconstruction.

Two different effects cause the reconstructed jet energy to be not equal to the original particle energy: detector effects, e.g. noise, can alter the energy of the jets. In addition algorithm inefficiencies, e.g. the limited cone size in case of the cone algorithm, lead to the effect that not all particles from a given jet are really associated to the reconstructed jet. To compensate for these effects, the so called Jet Energy Scale (JES) correction corrects the reconstructed jet energy back to the particle energy, on average.

For some measurements, including the analysis presented in this thesis, a further correction is needed: the so called parton-level corrections. These corrections try to adjust the particle energies obtained by the JES back to the energy of the parton that initiated this jet.

4.3.1 Calorimeter noise and the T42 algorithm

A special algorithm, called T42 algorithm [53], has been implemented to obtain a finer and uniform treatment of the calorimeter noise. It is based on a simple concept: in a

high granularity calorimeter, isolated cells are potentially noisy cells. The isolation is here defined in three dimensions.

The algorithm treats all cells with an energy above 4σ as "signal-like". An isolated cell is considered "noise" if it is not "signal-like" and if it has no "signal-like" 3-d neighbor, or if it has a negative energy. All cells identified as noise are removed by the T42 algorithm. A detailed description of the algorithm can be found in [54].

4.3.2 Jet algorithms

The task of the jet algorithm is to identify the calorimeter cells belonging to the particles from the original parton. This task is very complicated [55]. First, there are theoretical considerations: a jet algorithm should be infrared and collinear safe. This means that no infrared or collinear singularities appear in the calculation, i.e. the found solutions should be insensitive to soft or collinear radiation in the event. Furthermore the algorithm should be insensitive to boosts along the $z-$axis.

The second aspect is based on considerations on the detector effects and implementation of the algorithm. The algorithm should not amplify the resolution smearing effects and the angle biases, it should not be strongly dependent on the luminosity and have an optimal reconstruction efficiency. In addition it should be easy to calibrate the jets and the algorithm itself should make efficient use of computer resources.

Two different algorithms have been proposed [55] based on previous experience: a cone algorithm and a k_T algorithm. As to date only the jet energy scale corrections for the cone algorithm are available, the k_T algorithm cannot yet be used in analyses and will therefore not be discussed further.

Cone algorithm

The jet reconstruction starts by clustering the energy deposited in the calorimeter into seed towers. The E_T of each tower is calculated from its total energy and the polar angle θ between the beam axis and the tower center, as seen from the primary vertex: $E_T = E \cdot \sin\theta$.

The cone algorithm contains two free parameters: the minimal transverse energy of a jet, E_T^{min}, and the cone radius $R = \sqrt{\Delta\eta^2 + \Delta\phi^2}$, where η and ϕ of a jet are defined as the E_T weighted center of the towers i associated with the jet:

$$\eta = \frac{\sum_i E_T^i \cdot \eta^i}{E_T^i} \tag{4.3}$$

$$\phi = \frac{\sum_i E_T^i \cdot \phi^i}{E_T^i} \,. \tag{4.4}$$

The algorithm now works as follows:

- The energy in a cone radius R around each seed tower is calculated and the E_T weighted center of this cone is found. This new center is then used as the cone axis and the energy in the cone radius R is recalculated. This procedure is iterated until a stable cone axis is found. Each stable cone is called proto-jet.
- The mid-points in $\eta - \phi$ space between all proto-jets are used as seed towers if the midpoints are within $\Delta R < 2R$ between previously found proto-jets. The procedure from the previous step is repeated for these seed towers.

  Jets with the same axis, or with an energy below E_T^{min} are removed from the list.
- The second step produced a list of jets which may share energy. These ambiguities are solved with the following split and merge algorithm which is applied only to jets that share energy:
  - These jets are ordered in decreasing order of E_T.
  - Starting with the highest E_T jet, the highest E_T neighbor is found. If the ratio of shared energy over the energy of the neighbor is larger than 50% the two jets are merged otherwise the shared towers are associated to the nearest jet. The new center(s) are then calculated.
  - All jets that do not share energy are removed from the list of jets with shared energy and are kept as final jets. This procedure is repeated until no more jets share energy.

In this analysis the parameters used for the cone algorithm are $R = 0.5$ and $E_T^{min} = 8$ GeV.

4.3.3 Jet energy scale

The task of the Jet Energy Scale (JES) correction is to correct the energy of the jets found by the jet algorithm to the energies of the particle jet before it entered the calorimeter. A detailed description of the procedure can be found in references [56, 57]. It uses events where a photon recoils against a jet and consists of four main steps:

- Subtraction of the offset energy, E_{offset}, which does not originate from the hard interaction. This offset energy is due to noise in the calorimeter and energy from inelastic $p\bar{p}$ collisions (minimum bias interactions) other than the hard-scatter.
- Correction for the response of the calorimeter. The response R_{jet} is the ratio of the measured energy to the true energy deposited in the calorimeter.

- Correction for particles which are outside of the jet cone. This happens due to the geometrical construction of cone jets which does not take into account particles outside the given cone radius. F_S is the fraction of the jet energy contained within the jet cone.
- Proper treatment of muons inside the jets. Muons deposit only a small fraction of their energy (typically around 2 GeV) in the calorimeter. Therefore the jet energy is underestimated by ΔE_{lep} if there are muons present in the jet cone.

Taking these corrections into account the energy at the particle level, $E_{jet}^{particle}$ can be written as

$$E_{jet}^{particle} = \frac{E_{jet} - E_{\text{offset}}}{R_{jet} \cdot F_S} + \Delta E_{lep} \, . \tag{4.5}$$

The dominant part of the JES correction is the response. It is measured with the missing E_T Projection Fraction (MPF) method [56] in $\gamma + jet$ events. In case there are no neutrinos or muons in these events, the missing E_T measures the imbalance of transverse energy in the calorimeter due to differences in response to photons and jets.

The overall JES correction is the dominant systematic uncertainty for many measurements. This uncertainty is dependent on the jet energy and position in η and ranges from a few percent up to about 20% [58].

4.3.4 Parton-level corrections

The last correction that is applied to the jet energies adjusts the energy of the particle jet to equal that of the original parton, on average. This correction is important whenever an analysis requires computing the invariant mass of two or more jets, for example the top quark mass measurement or the analysis presented in this thesis. Determining this parton-level correction requires knowledge of the parton momentum 4-vector and the reconstructed jet momentum. It can therefore only be determined from simulated Monte Carlo events.

The parton-level corrections [59] have been derived as part of this thesis. They are derived as a function of energy for jets originating from the fragmentation of light quarks (u, d, s, c) and heavy quarks (b), and in three pseudorapidity bins. The pseudorapidity bins cover the central calorimeter ($|\eta| < 0.7$), the inter-cryostat region ($0.7 < |\eta| < 1.8$), and the end calorimeters ($1.8 < |\eta| < 2.5$).

Using the information about the generated events, the primary partons from $t\bar{t}$-decay (before radiation) are matched to jets, reconstructed using a cone algorithm with cone size $R = 0.5$. Only uniquely matched jet-parton pairs are used to reduce the contamination from hard gluon radiation that generates two distinct jets or overlap of jets from two or more partons. Figure 4.3 shows the corrections for the central calorimeter.

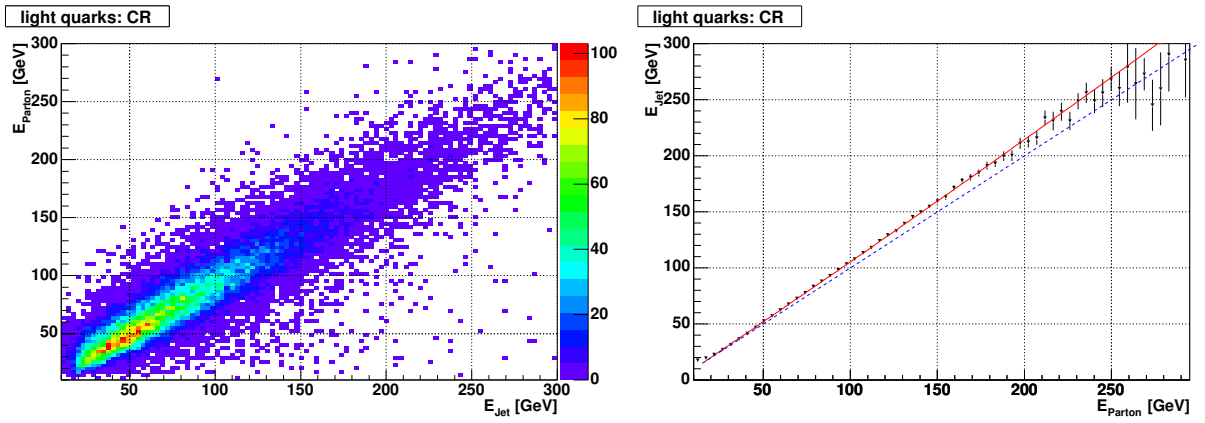

Figure 4.3: Parton energy versus JES corrected energy of jets in the central region matched to light quarks (left) and the average corrected jet energy versus parton energy for light-quark jets in the central region. The superimposed solid line is the polynomial fit and the dashed line is the bisector.

4.3.5 Jet quality selection

To suppress the contribution of fake jets, i.e jets where the cone algorithm clustered calorimeter noise, quality cuts are introduced [60]:

- the ratio of the highest to the next-to-highest transverse energy cell in the calorimeter should be less than 10,
- the number of towers containing 90% of the jet energy is required to be larger than one,
- the energy fraction deposited in the coarse hadronic calorimeter, CHF, should be less than 0.4 and
- the energy fraction deposited in the electromagnetic calorimeter, EMF, should be between 0.05 and 0.95.

In addition, a comparison with the energy measurement from the L1 trigger is made. As the L1 trigger uses a different readout path of the calorimter it provides a good handle on the presence of electronic noise in the precision readout. The scalar sum of the p_T of the trigger towers inside the jet cone, L1SET, should fulfill the following constraint:

$$\frac{\text{L1SET}}{p_{T_{jet}} \cdot (1 - \text{CHF})} > \alpha \,, \tag{4.6}$$

where $\alpha = 0.4$ in the CC and the EC and $\alpha = 0.2$ in the ICD region.

detector region	N/GeV	$S/\sqrt{\text{GeV}}$	C
$0.0 \leq \lvert\eta\rvert < 0.5$	5.05	0.753	0.0893
$0.5 \leq \lvert\eta\rvert < 1.0$	0.	1.20	0.0870
$1.0 \leq \lvert\eta\rvert < 1.5$	2.24	0.924	0.135
$1.5 \leq \lvert\eta\rvert < 2.0$	6.42	0.	0.0974

Table 4.2: Jet resolution constants for data.

4.3.6 Jet energy resolution

The jet energy resolution in data for high energy jets above $p_T \approx 50$ GeV is measured using dijet event samples and for low energy jets below 50 GeV using photon+jets events.

The measurement of the jet energy resolution makes use of the energy conservation in the transverse plane, i.e. in an event with two jets (or one jet and one photon) back to back. In these events the transverse energies of the two objects should be identical.

The resolution is parameterized using the following formula [60]:

$$\frac{\sigma_{p_T}}{p_T} = \sqrt{\frac{N^2}{p_T^2} + \frac{S^2}{p_T} + C^2}\,. \tag{4.7}$$

To incorporate the difference in the calorimeter with respect to $|\eta|$, the values for the parameters N, S and C are measured in bins of η. Table 4.2 lists the obtained values.

4.4 Electrons

Electrons are reconstructed from electromagnetic clusters in the calorimeter [60, 61]. All towers within a cone radius of $R = \sqrt{\Delta\eta^2 + \Delta\phi^2} = 0.2$ around a seed tower above 1.5 GeV are clustered together. The clusters are expected to have a large EM fraction $f_{EM} = E_{EM}/E_{tot}$, where E_{EM} is the energy in the electromagnetic calorimeter and E_{tot} is the total energy in the cone.

Furthermore, the clusters should be isolated, where the isolation is defined as the energy between cone radii of 0.2 and 0.4 divided by the energy in the 0.2 cone:

$$f_{iso} = \frac{E_{tot}(R < 0.4) - E_{EM}(R < 0.2)}{E_{EM}(R < 0.2)}\,. \tag{4.8}$$

Only those clusters with $f_{iso} < 0.15$ are selected.

The next step in the electron identification is the comparison of seven correlated shower shape variables with the expectation for an electron. The variables are the energies deposited at each EM layer (EM1-EM4), the total EM energy, the z-position of the vertex and the transverse shower width in ϕ. The 7x7 covariance matrix is a measure of how similar the shower is to an electron shower. The χ^2_{hmx}, calculated with the inverse of this covariance matrix (called H-matrix), is used to select electron candidates by applying a cut at $\chi^2_{hmx} < 50$.

As electrons are charged particles, at least one reconstructed track is required within a 0.05×0.05 road in $\eta \times \phi$ around the EM cluster.

4.4.1 Electron likelihood

Electron candidates which passed all the cuts so far are so called "loose" electrons. A "tight" electron in addition requires an output of the electron likelihood [62] of > 0.85. The likelihood used contains seven variables: the electromagnetic fraction f_{EM}, the 7 variable H-matrix, the ratio of transverse calorimeter energy over the transverse track momentum E_t / p_T, the number of tracks in a 0.05 cone around the cluster, the total p_T of tracks in a $R < 0.4$ cone around the candidate track, the *dca* of the track and the spatial χ^2 which determines how well the track and the EM cluster are matched in $\Delta\phi$ and Δz, where Δz is the difference in the vertex position calculated from the EM cluster and that from the track.

4.4.2 Energy calibration and resolution

The individual calorimeter channels are calibrated by measuring and equalizing their response to calibration pulses. Non-linearities in the readout electronics are corrected for as described in [63]. In addition the geometrical effects are taken into account as well as the energy lost by electrons in the material in front of the calorimeter [64].

In ϕ there are small cracks between the calorimeter readout modules. Electrons which are reconstructed to be (partially) in these cracks and/or at the edges of the detector in η, i.e. the electron is not in the fiducial region of the detector (CCout), have a different energy resolution than the ones that are in the fiducial region (CCin).

The energy resolution of electrons can be described using the same parameterization as for the jets (Eq. 4.7) by replacing p_T with E:

$$\frac{\sigma(E)}{E} = C \oplus \frac{S}{\sqrt{E}} \oplus \frac{N}{E}\,, \tag{4.9}$$

where C, S and N represent the constant, sampling and noise terms, respectively and the operator $\oplus$ is used as abbreviation for the addition in quadrature. To measure

electron type	Constant term C	Sampling term $S(\sqrt{\text{GeV}})$
CCin	0.044 ± 0.0002	0.224 ± 0.0018
CCout	0.112 ± 0.0011	0.385 ± 0.0125

Table 4.3: Values of the energy resolution parameters C and S for electrons inside (CCin) and outside the fiducial region.

these terms, $Z \rightarrow e^+e^-$ events are used. As the peak and the width of the invariant mass of the Z-boson is slightly different in data and Monte Carlo, the Monte Carlo is corrected for this difference.

The obtained resolution is summarized in Table 4.3. The method used to obtain these values [60] uses only high p_T electrons from 10 GeV up to 200 GeV and is therefore not sensitive to the noise term N.

4.5 Muons

Muons are reconstructed in two different detectors: the inner tracking detectors and the muon system. The information from the muon system is the basis of the muon identification.

Muons in the muon system, so called "local muons", are reconstructed by converting the timing information of the different readout channels into positions and times of hits in scintillators and wires. Then in each layer straight lines ("segments") are reconstructed from these hits. Finally, segments from the A-layer are fitted with segments from the B- and C-layer to measure the momentum of the local muon. Muons used in this analysis are required to have hits in all three layers of the muon system.

The inner tracking detectors reconstruct the muons as all other charged particles using the hits in the corresponding sub detectors as described in section 4.1.

The reconstructed muons are classified into three different quality classes, called "tight", "medium" and "loose" in decreasing order of quality. Their definition is as follows [65]:

- A muon is "tight" if it satisfies the following criteria
  - at least two wire hits and at least two scintillator hits in the A-layer
  - at least three wire hits and at least one scintillator hit in the BC-layers
  - a converged local track fit
- A "medium" muon needs to have

  - at least two wire hits and at least one scintillator hit in the A-layer
  - at least two wire hits in the BC-layers
  - at least one scintillator hit in the BC-layer (except for central muons with less than four BC wire hits)

- A "loose" muon is a medium muon where one of the tests for the medium quality is allowed to fail but there needs to be at least one scintillator hit.

A veto on cosmic muons is applied by requiring the time difference between scintillator hits in B or C and the A layer to be consistent with a muon coming from the interaction region.

The muons for this analysis are further required to be matched to a central track, where the central track needs to meet the following specifications [60]:

- The central track should be well reconstructed, i.e. the χ^2 per degree of freedom from the track fit should be less than 4.
- It should originate from the primary vertex, i.e. $|\Delta z(\mu, PV)| < 1$ cm and a *dca* significance of $dca/\sigma(dca) < 3$, to reject muons from semi-leptonic heavy flavor decays.

In case the central track consists of only hits in the the CFT, the momentum of the central track is refitted using the primary vertex as a constraint [66], i.e. the *dca* after the correction is 0, to improve the momentum resolution.

4.5.1 Muon isolation

Muons from a decay of a W boson tend to be isolated as opposed to muons from a semi-leptonic decay of a B hadron which tend to be reconstructed inside a jet.

A "loose" requirement for the isolation is therefore to require that there are no jets reconstructed in a cone of $R = 0.5$ around the muon. However, due to jet reconstruction inefficiencies, two additional variables have been introduced which make use of the tracking information to ensure the isolation of the muon:

- $Halo(0.1, 0.4)$, which is the sum of the E_T of calorimeter clusters in a hollow cone between $R = 0.1$ and $R = 0.4$ around the muon. Only the energy in the EM and the FH part of the calorimeter is considered in the calculation of this variable. Isolated muons deposit a small amount of energy in the calorimeter (minimum ionizing particle) in a small cone of radius 0.1 around the trajectory of the muon. As the muon is isolated, the amount of energy deposited in a larger cone of radius 0.4 is small.

- *TrkCone*(0.5), which is the sum of the track p_T of all tracks within a cone of radius $R = 0.5$ around the muon. The track matched to the muon is excluded from this sum. This variable therefore measures the amount of track p_T around the muon which, for isolated muons, is small[1].

The muons from the decays of W bosons have a lower value of these variables than the muons originating inside jets. In addition the muon p_T spectrum is different: muons from W boson decays have on average a higher p_T due to the high mass of the W boson. This is incorporated in the "tight" isolation criterion by dividing the isolation variables by the muon transverse momentum p_T^μ.

A muon has a "tight" isolation, if it satisfies the following two criteria:

- $Rat11 = Halo(0.1, 0.4)/p_T^\mu < 0.08$
- $Rattrk = TrkCone(0.5)//p_T^\mu < 0.06$.

4.5.2 Muon p_T resolution

The muon p_T resolution has been studied in Monte Carlo by comparing the p_T of the reconstructed muon to that of the corresponding Monte Carlo muon [60]. As the momentum resolution depends on the number of associated hits in the tracking detectors, the resolution is studied in two separate regions in η: the region of full CFT coverage (i.e. in principle there can be 16 measurement points), $|\eta_{\text{det}}| < 1.62$, and the forward region, $|\eta_{\text{det}}| \geq 1.62$.

The momentum resolution is parameterized using the following functional form:

$$\sigma\left(\frac{1}{p_T}\right) = a \oplus \frac{b}{p_T}\,, \tag{4.10}$$

where the two coefficients are found separately for the two detector regions. Table 4.4 lists the obtained values.

The differences between Monte Carlo and data are studied by comparing the position and width of the $Z \to \mu^+\mu^-$ peak. These differences can be corrected for by scaling the muon p_T and applying an additional smearing in the Monte Carlo:

$$\frac{1}{p_T'} = \frac{1}{\alpha \cdot p_T} + \xi\,, \tag{4.11}$$

where α is a scale factor and ξ is a random Gaussian correction with width σ_ξ. The obtained values are listed in Table 4.5.

[1] It is not zero due to the presence of minimum bias interactions and fake tracks. Also the muon isolation doesn't always have to be larger or equal to 0.5

η range	$\sigma(1/p_T)$ vs. $1/p_T$, 1/GeV
$0 < \lvert\eta_{\text{det}}\rvert < 1.62$	$0.00152 \oplus 0.0279/p_T$
$1.62 \leq \lvert\eta_{\text{det}}\rvert$	$0.00226 \oplus 0.0479/p_T$

Table 4.4: Muon momentum resolution in the Monte Carlo for the two different η regions [60].

η range	α	σ_ξ
$0 < \lvert\eta_{\text{det}}\rvert < 1.62$	0.991	0.0023 1/GeV
$1.62 \leq \lvert\eta_{\text{det}}\rvert$	0.999	0.0047 1/GeV

Table 4.5: Correction factors for the Monte Carlo muon momentum for the two different η regions [60].

4.6 Neutrinos

Neutrinos cannot be directly detected with the DØ detector. They escape the detector region without interacting with the detector material. However, it is still possible to infer the presence of neutrinos from the imbalance of the event.

The longitudinal boost of an event is not known, but the transverse momentum of the initial particles from the hard interaction is negligibly small and therefore the event should be balanced in the transverse plane, i.e. the vector sum over all particle energies in the transverse plane should be zero. An imbalance can then be interpreted as being caused by at least one neutrino in the event. The transverse energy that is missing to balance the event is called missing transverse energy, $\not\!\!E_T$:

$$\not\!\!E_{Tx,y} = 0_{x,y} - \sum_{i}^{\text{particles}} E^i_{x,y} \tag{4.12}$$

$$\not\!\!E_T = \sqrt{\not\!\!E_{Tx}^2 + \not\!\!E_{Ty}^2} \tag{4.13}$$

It is a measure for the x and y components of the neutrino energy, in case there is only one neutrino, or the sum of the x and y coordinates of the neutrinos if there are more than one.

To calculate the missing transverse energy, the following procedure is used:

- Calorimeter cells surviving the T42 algorithm are used to calculate the raw $\not\!\!E_T$. This does not include all cells in the coarse hadronic layer due to the higher level of noise in these cells. Only those coarse hadronic cells within reconstructed jets are used in the calculation.

- The difference in response for isolated electromagnetic particles and for jets are taken into account by the jet energy scale correction. These corrections applied to all good jets need to be subtracted from the raw $\not\!\!E_T$.
- As muons deposit only a small amount of energy in the calorimeter, its presence leads to an overestimation of the $\not\!\!E_T$. To correct for this, the momentum of all muons matched to central tracks is added up and from this sum the average amount of energy deposited by a muon in the calorimeter times the number of muons is subtracted. The resulting energy is subtracted from the missing transverse momentum vector.

4.7 b-tag using secondary vertices

The presence of a secondary vertex in the event is a hint towards particles with a longer lifetime. By requiring certain criteria on the quality and distance of these secondary vertices, events which contain a b quark can be selected.

The description of the tracking detectors in the Monte Carlo simulation is not perfect, especially the inefficiencies due to dead SMT strips and the detector material are not yet completely simulated. Therefore the b-tag algorithm cannot be applied directly to the Monte Carlo events, but the b-tag and mistag efficiencies need to be measured in data and parameterized. These parameterizations are then applied to the Monte Carlo to get a good description of the b-tag.

4.7.1 b-tag algorithm

The b-tagging procedure relies on the fact that B hadrons are relatively long lived particles that decay after traveling an average of about 5 mm at a p_T of 50 GeV/c. This decay produces on average about 5 charged particles [67]. These particles form a secondary vertex which can be found by the algorithm described in section 4.2.2.

Different operating points for the b-tag have been studied [68]. They differ in the misidentification (mistag) rate for light quarks, e.g. how often a vertex is tagged as coming from a b quark while in reality it is produced by light quarks. These operating points are called "loose", "medium" and "tight" and provide a mistag rate of 1%, 0.5% and 0.25% respectively.

The b-tag first applies vertex selection criteria to ensure vertices of good quality. In addition a procedure called V0 removal is applied to reduce the number of vertices from non-B hadrons: two-track secondary vertices which are consistent with being from a K^0_S, Λ or a photon conversion are removed. This is done by looking at the invariant mass and the angle between the two tracks.

Variable	"loose"	"medium"	"tight"
Track cuts			
$\|dca\|$	≥ 0.15 cm	≥ 0.15 cm	≥ 0.15 cm
$\|zdca\|$	≥ 0.4 cm	≥ 0.4 cm	≥ 0.4 cm
$\|dca\|/\sigma_{dca}$	≥ 3.0	≥ 3.5	≥ 3.5
χ^2	< 10	< 10	< 3
p_T	> 1.0 GeV	> 1.0 GeV	> 1.0 GeV
Number of hits in the SMT	≥ 2	≥ 2	≥ 2
Vertex properties			
vertex multiplicity	≥ 2	≥ 2	≥ 2
χ^2/dof for attaching tracks to vertex	< 15	< 15	< 15
vertex χ^2/dof	< 100	< 100	< 100
vertex decay length $\|\vec{L}_{xy}\|$	≤ 2.6 cm	≤ 2.6 cm	≤ 2.6 cm
vertex collinearity $\vec{L}_{xy} \cdot \vec{p}_T / \|\vec{L}_{xy}\|\|\vec{p}_T\|$	≥ 0.9	≥ 0.9	≥ 0.9
decay length significance $L_{xy}/\sigma(L_{xy})$	≥ 5.0	≥ 6.0	≥ 7.0

Table 4.6: Selection cuts for the different operating points of the b-tag: cuts on the tracks that enter in the reconstruction of the vertices (upper half) and cuts on the vertices themselves (lower part)

Table 4.6 lists all the cuts applied to select good secondary vertices for the different operating points. Among the variables are the transverse vertex decay length, $|\vec{L}_{xy}| = |\vec{r}_{SV} - \vec{r}_{PV}|$, and the collinearity angle which is defined as the inner product of $\vec{L}_{xy}$ and the total vertex transverse momentum computed as the sum of the momenta of all attached tracks. It measures how well the secondary vertex points back to the primary.

The key variable which distinguishes between secondary vertices from b hadrons and other secondary vertices is the decay length significance $|L_{xy}/\sigma(L_{xy})|$ which measures how significant the distance between the primary and the secondary vertex is.

The calorimeter jets are then associated with the secondary vertices if the difference in (η, ϕ) is less than 0.5: $\Delta R(SV, jet) < 0.5$. A jet is tagged as b-jet if it has at least one secondary vertex with a decay length significance above the cut value from Table 4.6. Depending on the sign of L_{xy} the jets are called "negative tagged" ($L_{xy} < 0$) or "positive tagged" ($L_{xy} < 0$). Negative tags originate purely from resolution effects while positive tags originate in addition from the presence of long lived particles.

The analysis presented in this thesis uses the b-tag in the "tight" configuration to ob-

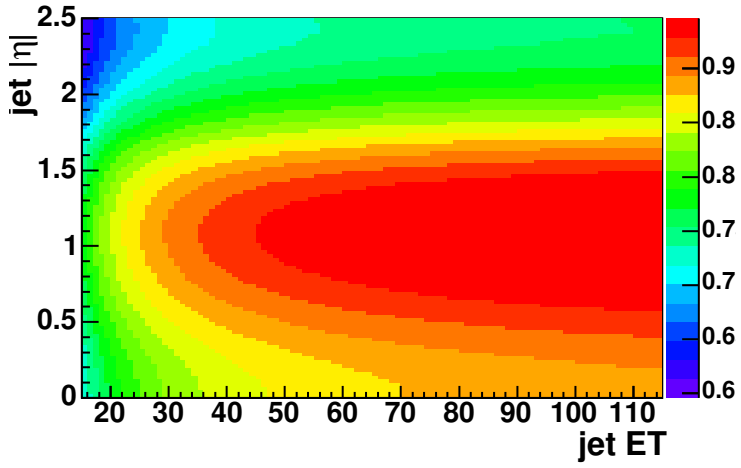

Figure 4.4: Parameterization of the taggability obtained in data.

tain a high purity of the sample.

4.7.2 b-tag parameterization

Ideally, the b-tag algorithm described above could be applied in the same way as for the data to Monte Carlo events. However, the simulation of the tracking detectors is not yet good enough. Therefore the b-tag and mistag efficiencies are measured in data and Monte Carlo separately and scale factors are calculated to match the results from Monte Carlo to the data [69].

The b-tag and mistag efficiencies are split up into two parts:

- the "taggability", which is the efficiency for a jet to meet the minimal requirements necessary to tag a jet and
- the efficiency to tag a "taggable" jet.

This separation largely decouples the tagging efficiency from issues related to tracking inefficiencies and/or calorimeter problems.

A calorimeter jet with $E_T > 15$ GeV and $|\eta| < 2.5$ is taggable if it is matched with a track-jet within $\Delta R < 0.5$. The taggability per jet is measured in data as a function of jet E_T and η. Figure 4.4 shows the obtained parameterization.

b-tagging efficiency and scale factors

To measure the b-tagging efficiency in data, a sample which is enriched with b quarks needs to be selected. As roughly 10% of all B hadrons produce muons, a sample with events where at least one jet contains a muon with large transverse momentum relative to this jet is selected. Using this sample, the b-tagging efficiency for semi-leptonic b decays, $\epsilon^{data}_{b\to\mu}$, can be derived depending on the E_T and η of the jet.

The same efficiency can be determined on Monte Carlo, $\epsilon^{MC}_{b\to\mu}$. In addition the inclusive b-tagging efficiency, ϵ^{MC}_{b}, can be obtained in Monte Carlo as the jet flavor can be determined by matching the direction of the reconstructed jet with B hadrons. As also jets from c quarks produce displaced secondary vertices, the inclusive c-tagging efficiency, ϵ^{MC}_{C} is also measured in Monte Carlo.

In order to calibrate the b-tagging efficiency in Monte Carlo to that measured in data, a scale factor is calculated:

$$SF_{b\to\mu}(E_T,\eta) = \frac{\epsilon^{data}_{b\to\mu}(E_T,\eta)}{\epsilon^{MC}_{b\to\mu}(E_T,\eta)} \,. \tag{4.14}$$

Assuming that the scale factor for inclusive b decays is the same as for semi-leptonic ones, $SF_b = SF_{b\to\mu}$, the calibrated Monte Carlo b-tagging efficiency, $\epsilon_b(E_T,\eta)$, can be obtained:

$$\epsilon_b(E_T,\eta) = \epsilon^{MC}_{b}(E_T,\eta)\cdot SF_b(E_T,\eta) \,. \tag{4.15}$$

To be able to calculate $\epsilon_c(E_T,\eta)$ using the same procedure, the c-tagging efficiency needs to be measured in data. However, this is not straightforward and it is just assumed, that the scale factor for c quarks is the same as for b quarks, $SF_c = SF_b$. This leads to the calibrated c-tagging efficiency:

$$\epsilon_c(E_T,\eta) = \epsilon^{MC}_{c}(E_T,\eta)\cdot SF_c(E_T,\eta) \,. \tag{4.16}$$

efficiency for light flavor jets

Track misreconstruction and resolution effects can cause light-flavor jets (from u,d,s quarks or gluons) to be tagged. These effects are expected to contribute symmetrically to both positive and negative tags. It can therefore be measured in data by looking at the negative tagging efficiency, ϵ^{data}_{-}, for taggable jets.

The obtained efficiency does not represent the real efficiency for light flavor jets because the inclusive negative tag rate contains contamination from heavy flavor jets. In addition, the assumption that the positive tag efficiency and the negative tag efficiency are equal for light flavor jets is invalidated by the presence of long lived parti-

cles which enhances the positive tagging efficiency if these particles are not completely removed by the b-tag algorithm (e.g. if one of the two tracks is not reconstructed).

Both effects are corrected for by calculating appropriate scale factors, SF_{hf} and SF_{ll}, using inclusive QCD Monte Carlo. This leads to the final efficiency $\epsilon_l(E_T, \eta)$ for light quark jets:

$$\epsilon_l(E_T, \eta) = \epsilon_-^{data}(E_T, \eta) \cdot SF_{hf}(E_T, \eta) \cdot SF_{ll}(E_T, \eta) \tag{4.17}$$

Figure 4.5 shows a comparison of the semi-leptonic b-tagging efficiency obtained in data with the inclusive b- and c-tagging efficiencies in Monte Carlo and the efficiency parameterization for light quark jets.

4.8 $t\bar{t}$ reconstruction

An essential point of this analysis is the reconstruction of the four-vectors of the initial partons: top and anti-top quark, the two W bosons and the two b quarks. This is necessary to reconstruct the decay angle $\cos\theta$ in the rest frame of the W boson.

The reconstruction is based on the SQUAW [70] kinematic fitting algorithm which has been successfully used in the measurement of the top mass in RunI [71]. It is implemented in a package called `HitFit`.

The task of this package is the following: given a measured lepton, 4 or more measured jets and the missing energy the four-vectors of the initial partons should be reconstructed taking into account one or more imposed constraints.

This problem can be expressed in the following formula:

$$\chi^2 = (\mathbf{x} - \mathbf{x^m})^T \mathbf{G} (\mathbf{x} - \mathbf{x^m}) \ , \tag{4.18}$$

where $\mathbf{x}$ is the vector of the fitted values, $\mathbf{x^m}$ is the vector of the measured values and $\mathbf{G}$ is the inverse error matrix. The variables entering this equation are the energy and momentum of the lepton and the jets and the transverse missing energy. All the errors on these quantities are assumed to be uncorrelated, i.e. $\mathbf{G}$ is diagonal.

This χ^2 should be minimized such, that the following constraints are met:

$$m_{W_{lep}} = m_{W_{had}} = 80.4 \text{ GeV}/c^2 \tag{4.19}$$

$$m_{t_{lep}} = m_{t_{had}} = m_{t_{ext}} \ , \tag{4.20}$$

where $m_{t_{ext}}$ is an optional parameter. In measurements of the top quark mass this parameter will not be set and the two top quarks only need to have the same mass while in other measurements this can be set to a specified mass, e.g. the world average of the top quark mass.

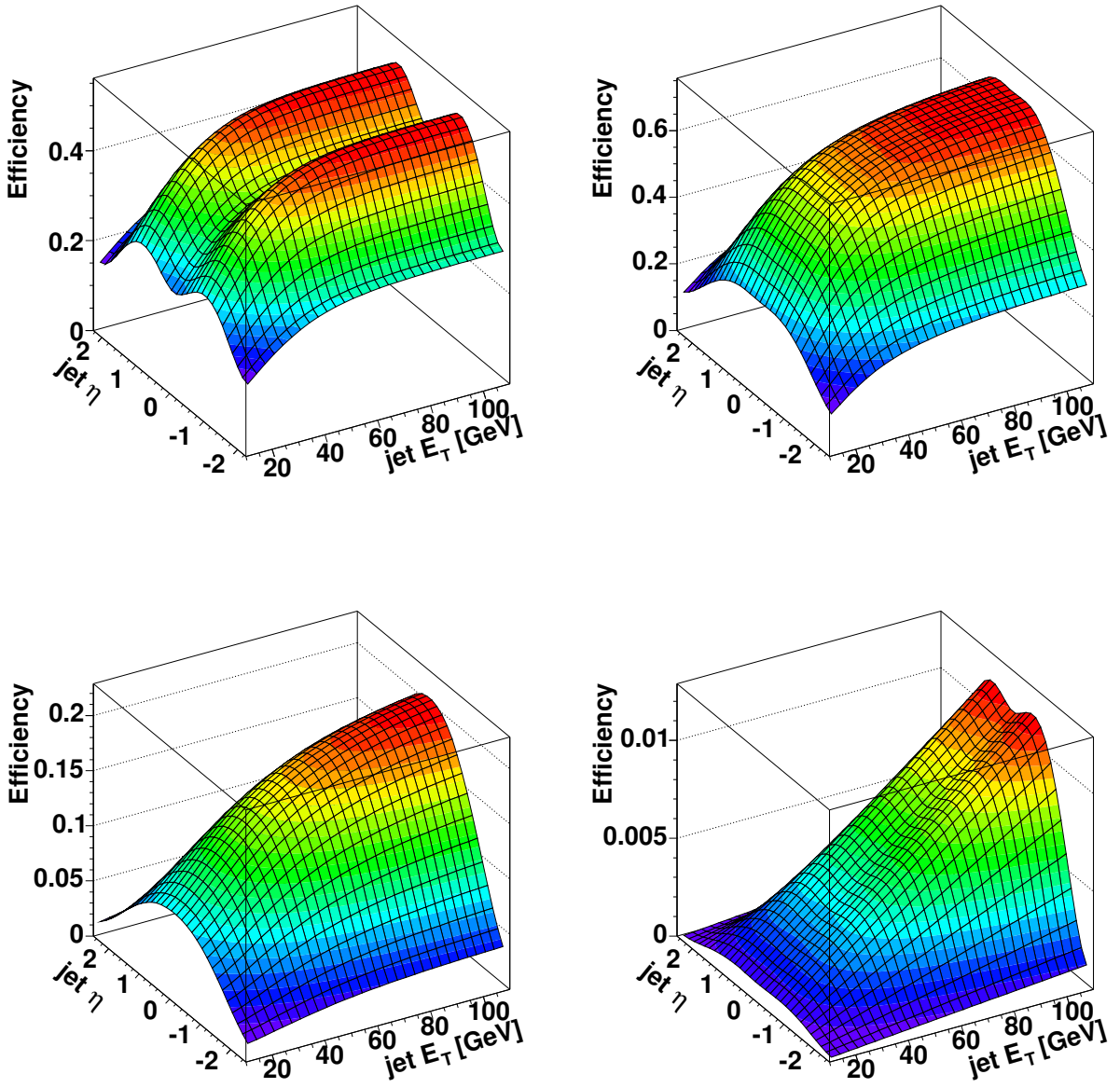

Figure 4.5: Comparison of the semi-leptonic b-tagging efficiency obtained in data (top left) with the inclusive b- (top right) and c-tagging efficiencies (bottom left) in $t\bar{t}$ Monte Carlo. The negative tag rate parameterization is shown in the bottom right plot. These plots are taken from [69].

To be able to calculate the constraints an additional parameter is needed: the z component of the neutrino momentum.

The estimate of the neutrino z component, p_z^ν is based on the knowledge, that both top quarks have the same mass. This leads to the following quadratic equation for p_z^ν:

$$0 = \left[(p_z^c)^2 - (E^c)^2\right](p_z^\nu)^2 + \alpha p_z^c p_z^\nu - (E^c p_T^\nu)^2 + \frac{\alpha^2}{4} \quad \text{with} \tag{4.21}$$

$$\alpha = m_t^2 - m_c^2 + 2\vec{p_T}^{\,\nu} \cdot \vec{p_T}^{\,c} \tag{4.22}$$

where the four-vector c is the sum of the four-vectors of the lepton and the b-jet.

In case of two solutions for p_z^ν both values are tried as starting value and the one leading to the lower χ^2 is kept. As p_z^ν is not used in the calculation of χ^2 it can only influence which local minimum is found.

A priori the jet-parton association is not known. In case of only four jets present in the event, this leads to $4! = 24$ possible jet combinations. As there is no need to distinguish between the jets from the W decaying into two jets this number can be reduced to 12.

If there are more than four jets in the event only the four highest E_T jets are considered. A correct implementation of the treatment of initial and final state radiation has not yet been implemented due to the complexity of the problem, i.e. the increased number of possible combinations.

5 Data sample and event selection

The only available source of $t\bar{t}$ events to date is the Fermilab Tevatron accelerator. One of the two detectors that record such events is the DØ detector described previously. The events used in this analysis have been recorded starting June 2002 until March 2004.

Besides $t\bar{t}$ events, the DØ detector records events originating from a wide range of other physics processes. A preselection of events to be used in this analysis is therefore made demanding events compatible with the topology of top events. This selection is based on the trigger decision. Since the luminosity is calculated separately for each trigger decision, this procedure leads to slightly different luminosities depending on the trigger.

Furthermore quality cuts were applied to the data in order to reject data for which the detector was not properly functioning, e.g. some of the subdetectors were failing or noise was present in the calorimeter.

At the end of this chapter the general event preselection for $t\bar{t}$ analyses is presented. This preselection selects a sample that is enriched in $t\bar{t}$ events by requiring the presence of objects expected in $t\bar{t}$ events decaying into exactly one charged lepton, a neutrino and several jets.

Monte Carlo simulation is used to model the expected properties of the different physics processes relevant to this analysis, the $t\bar{t}$ signal as well as the background processes that contain a W boson.

5.1 Trigger

This analysis uses $t\bar{t}$ events where one of the two W bosons from the decay of the top quarks decays into two quarks and the other W boson decays into either an electron and an electron neutrino or into a muon and a muon neutrino. The decay of the W boson into τ and a τ neutrino is only considered if the τ decays into an electron or muon, making the decay indistinguishable from a direct W boson decay into an electron or muon.

Therefore the corresponding trigger requirements are based on the presence of a charged

lepton, electron or muon, with certain properties and the presence of one or more jets.

The instantaneous luminosity changed during the data taking period and also the trigger system and algorithms changed with time. These changes are reflected in different versions of the trigger list. To account for these changes, the criteria on the leptons and jet candidates in the triggers have been changed.

The criteria for choosing the specific selection cuts in the triggers depend on the limited available bandwidth for the three different trigger levels. Ideally all events would be recorded. However, only 50 events per second can be written to tape and reconstructed. Choosing these criteria is therefore a compromise between the selection efficiency of these cuts and the rate of events that pass these selections. In the following the selection cuts used in the triggers for this analysis are summarized.

5.1.1 Electron channel

Initially (up to trigger list version 11), the trigger demanded the following conditions at Levels 1 to 3 ("`EM15_2JT15`"):

Level 1: one calorimeter EM trigger tower with $E_T > 10$ GeV and two jet towers with $E_T > 5$ GeV;

Level 2: one EM candidate with $E_T > 10$ GeV and EM fraction of > 0.85 and two jet candidates with $E_T > 10$ GeV;

Level 3: one electron candidate with an E_T of at least 15 GeV and two jet candidates with $E_T > 15$ GeV.

In trigger version 12 these requirements have been replaced with the following criteria ("`E1_SHT15_2J20`"):

Level 1: one calorimeter EM trigger tower with $E_T > 11$ GeV;

Level 2: no requirements;

Level 3: one tight electron candidate with $E_T > 15$ GeV and two jet candidates with $E_T > 20$ GeV.

5.1.2 Muon channel

Trigger lists up to version 11 use the following requirements ("`MU_JT20_L2M0`"):

Level 1: one muon scintillator trigger and one calorimeter jet trigger tower with an E_T of at least 5 GeV;

Level 2: one medium muon;

Level 3: at least one jet with $E_T > 20$ GeV.

In trigger version 12 the Level 1 and Level 3 requirements have been replaced with the following criteria ("`MU_JT25_L2M0`"):

- one muon scintillator trigger and one calorimeter jet trigger tower with an E_T of at least 3 GeV at Level 1;
- at least one jet with $E_T > 25$ GeV at Level 3.

5.2 Data quality

The quality of the data used in this analysis is ensured by applying a quality selection based on runs[1] and luminosity blocks[2]. The run based selection uses the information stored in the run quality database. This database contains information about the status of the main subdetectors (SMT, CFT, calorimeter, muon system). It is set up based on information from the shifters in the control room and from the individual subdetector experts. This analysis requires that no subdetector has a status labeled "bad" and the status of the muon system should be at least "reasonable"[3]. This ensures that the subdetectors were in the readout and had no obvious problems.

The quality of the calorimeter information is checked based on time intervals given by luminosity blocks. Two kinds of effects are detected:

- Grounding problems in the calorimeter can cause signals faking an inhomogeneous ring of energy in ϕ ("Ring of Fire"). This leads to a large missing energy signature. The events are scanned for the specific pattern of this effect and the corresponding luminosity blocks are removed from the analysis.
- Files consisting of approximately 20 luminosity blocks are scanned for an abnormal behavior in the missing energy: if the missing energy is shifted by more than 6 GeV from 0, or the RMS of the missing energy is larger than 20 GeV, or the average scalar E_T is larger than 60 GeV, all luminosity blocks in this file are marked as bad and removed from the analysis.

[1] A run is a continuous data taking period of up to 4 hours without any change to the configuration of the detector.

[2] A luminosity block is the smallest unit for which the integrated luminosity is calculated.

[3] The reason why the muon system should be flagged "reasonable" and not just "not bad" is to avoid to pick up special runs for the muon system (like runs where the magnets were turned off). For the other subdetectors these special runs are already flagged as "bad".

Trigger list	Muon channel		Electron channel	
	Delivered	Reconstructed	Delivered	Reconstructed
v8.2	29.4	21.3	29.4	20.7
v9	40.5	21.4	40.5	21.4
v10	18.3	15.7	18.3	15.6
v11	68.7	58.3	68.7	55.9
v12	137.1	112.4	137.2	112.7
total	294.0	229.1	294.0	226.3

Table 5.1: Integrated luminosity separately for each trigger list version. The first number is the delivered luminosity by the Tevatron and the second number is the luminosity in the reconstructed data sample after all data quality criteria have been applied.

A detailed explanation of the data quality requirements can be found in [61] and [66]. Table 5.1 shows a breakdown of the luminosity for the different trigger list versions in each of the two channels.

5.3 Monte Carlo samples

The properties of the $t\bar{t}$ signal and the $W+$ jets and single top backgrounds are studied using Monte Carlo simulation. The simulation of an individual event is done in the following sequence:

- In the first step the leading order matrix element of the given process is used to simulate the four-vectors of the hard interaction. This is done using the ALPGEN [72] simulation program. The CTEQ5L [73] parameterization of the parton density function (PDF) for the proton and the anti-proton has been used.

- These four-vectors are then fed into PYTHIA [74] which simulates the fragmentation and hadronization and also the underlying event due to the proton and anti-proton fragments. The same parameterization for the PDF has been used as in the first step.

  The output of PYTHIA is again a list of four-vectors, this time containing all stable[4] particles in the event.

[4]Stable here refers to particles that have a lifetime which is large enough to reach elements of the detector.

- The interaction of these particles with the material of the detector is modeled using the GEANT [75] simulation package. It is responsible for tracing the trajectories of these particles as well as their decay (if applicable) inside the detector elements and calculating the energy deposition in the individual detector elements. The output of this program are the trajectories of the particles as well as their energy depositions in the detector elements.

- A simulation of the detector response due to these energy depositions is then used to transform the output of GEANT into the same format as real data events. This program, called `DØSim`, also combines the energy depositions of multiple events. This is needed to correctly address the fact, that (depending on the instantaneous luminosity) not only the hard interaction but also several minimum bias interactions can take place at the same time.

  For the dataset used in this analysis, on average 0.5 minimum bias events have to be overlaid over the hard interaction. This is done by drawing a random number according to a Poisson distribution with mean 0.5 for each Monte Carlo event. The resulting number is the number of minimum bias events that are overlaid over this event.

- At this point the Monte Carlo events look identical to real data events and can be treated by the same version of the reconstruction software as the data. The only difference is that these events contain no trigger information as the triggers have not been simulated. This has to be taken into account later in the analysis: the efficiency for each trigger has been measured in data as a function of the lepton and jet energies and directions. The `top_trigger` [76] package uses these informations to calculate a probability for each event to pass the trigger requirements.

  Events from Monte Carlo simulations also contain the full decay chain of the simulated events together with the true four-vectors of all particles.

A more detailed description of the concept and challenges of Monte Carlo simulation at hadron colliders and the various event simulation programs can be found in Ref. [77]. In the following the specific samples used in this analysis will be explained.

5.3.1 $t\bar{t}$

The main $t\bar{t}$ samples have been generated using a top quark mass of 175 GeV, in agreement with the world average value for the top quark mass [11] at the point in time when this analysis started. One of the two W bosons produced in the decay of the $t\bar{t}$ pair was forced to decay into a charged lepton and a neutrino and the other one into a pair of quarks.

Process	f_+	m_t [GeV]	Number of events
$t\bar{t} \to \ell$+jets	0.00	175	204,700
	0.05	175	23,450
	0.10	175	23,450
	0.15	175	24,450
	0.20	175	23,950
	0.25	175	23,950
	0.30	175	204,700
$t\bar{t} \to \ell$+jets	0.00	170	48,250
	0.00	180	48,000
	0.30	170	47,250
	0.30	180	48,000
$t\bar{t} \to \ell\bar{\ell}$	0.00	175	47,000
$t\bar{t}$ + jet $\to \ell$+jets	0.00	175	48,500

Table 5.2: $t\bar{t}$ Monte Carlo samples that are used in this analysis for the different values of f_0, different values of the top mass and different decay modes: either exactly one W boson was required to decay into a lepton and neutrino, $t\bar{t} \to \ell + jets$, or both W bosons were required to decay leptonically, $t\bar{t} \to \ell\bar{\ell}$.

To simulate the different values for the fraction of W bosons with positive helicity, f_+, the $V - A$ charged current interaction in ALPGEN has been replaced with a linear combination of a $V - A$ and a $V + A$ interaction. Seven different values for f_+ have been simulated with most of the statistics accumulated at the two extreme values of f_+, corresponding to a pure $V - A$ and a pure $V + A$ interaction.

To study systematic effects related to the uncertainty on the top quark mass, additional samples have been generated where the top quark mass has been set to 170 GeV and 180 GeV respectively.

The default samples contain only pure $t\bar{t}$ events without additional gluon radiation simulated in the hard interaction, i.e. in the leading order matrix element. To address the issue of additional gluon radiation in $t\bar{t}$ events a special $t\bar{t}$ +jets sample has been generated where in the leading order matrix element one additional jet has been required.

Finally also samples where both W bosons decay into a lepton and a neutrino have been generated to estimate the background from these events.

Table 5.2 shows a summary of all the $t\bar{t}$ Monte Carlo samples that have been used and the corresponding values for the top quark mass and the fraction W bosons with positive helicity.

Process	σ [pb]	Scale Q^2	Number of events
$Wjjjj$	49.5	$m_W^2 + \sum m_T^2$	413,100
$Wcjjj$	3.15	$m_W^2 + \sum m_T^2$	438,250
$Wccjj$	5.83	$m_W^2 + \sum m_T^2$	379,600
$Wbbjj$	2.36	$m_W^2 + \sum m_T^2$	421,900
$Wjjjj$	49.5	$\langle p_T \rangle^2$	92,200

Table 5.3: $W+$jets Monte Carlo samples that are used in this analysis together with their theoretical cross-section and the chosen parameterization for the scale Q^2.

5.3.2 W+jets

The main background to the top event topology consists of W boson production with additional jets from initial state radiation. With the ALPGEN generator it is possible to simulate the various combinations of quark flavors produced in addition to the W boson.

Only samples with exactly 4 additional jets in the leading order matrix element have been generated. This translates into the following possible quark flavor samples: $Wjjjj$, $Wcjjj$, $WccJj$, $WbbJj$, $Wcccc$, $Wbbcc$ and $Wbbbb$, where j represents either a u, d or s quark or a gluon. J can in addition also stand for a c quark. The cross-sections for the processes with more than three c or b quarks are negligible and therefore these samples, $Wcccc$, $Wbbcc$ and $Wbbbb$ have not been generated.

The parameterization for the factorization scale Q^2 has been set to $Q^2 = m_W^2 + \sum m_T^2$, where m_T is the transverse mass defined as $m_T^2 = m^2 + p_T^2$. The sum $\sum m_T^2$ extends to all final state partons (including the heavy quarks but excluding the W decay products). At the generator level no cuts on the charged lepton or neutrino have been applied but there are cuts on the light quarks in the event: the minimum p_T for the quarks has been set to 8 GeV and the quarks are required to be within $|\eta| < 3.5$. In addition the separation between each light quark and any other quark should be at least $\Delta R > 0.4$.

During the processing of the events inside PYTHIA additional jets can be radiated. No cuts on these extra radiated jets have been applied. This also implies that there is no parton-matching applied at the generator level. This will be taken care of in the analysis of these events by matching the initial quarks produced by ALPGEN with reconstructed jets. Only those events where the initial quarks could be matched to reconstructed jets are used in the analysis to avoid double counting.

Table 5.3 lists the $W+$jets Monte Carlo samples that are used in this analysis together with their theoretical cross section.

5.3.3 Single top

Unlike the $t\bar{t}$ and the $W+$jets samples, ALPGEN cannot be used to model the electroweak production of top quarks. Instead a dedicated Monte Carlo generator for single top production, SingleTop, is used which is based on the CompHEP [78] package for symbolic and numerical calculations in high energy physics. The four-vectors produced by the SingleTop generator are then passed to PYTHIA just like for the other processes and the remaining steps are identical.

Only the t-channel process for single top production is considered as the s-channel has a factor of two lower theoretical cross-section and also a lower jet multiplicity. This leads to a very small contribution from the s-channel which has been neglected in this analysis. The Monte Carlo sample used was generated with a top mass of 175 GeV and contains 33,000 events.

5.4 Preselection

The event preselection is designed to select a data sample enriched in $W+$jets and $t\bar{t}$ events. To accomplish this, the preselection aims to select charged leptons, electrons or muons, from W boson decays in addition with four or more jets and high $\not\!\!E_T$. Tables 5.4 and 5.5 list the individual cuts for each channel together with the cumulative selection efficiency.

The selection starts by requiring four or more jets in the event. This rejects nearly 50% of the signal events but it is unavoidable for the reconstruction of the $t\bar{t}$ system with the kinematic fit described in section 4.8. In principle using a lower cut on the jet p_T would regain efficiency. However, the high threshold of 8 GeV at the reconstruction level which, after applying the jet energy scale correction, leads to jet energies of around 12 GeV, does not leave much room for improvement. In addition the $W+$jets Monte Carlo samples have been generated with a cut on the p_T of the light quarks of 8 GeV. Therefore it was decided that a lower cut on the jet p_T is not feasible.

In the next step exactly one tight high p_T charged lepton is required. The muon channel uses the full coverage of the muon system, $|\eta_\mu| < 2.0$, whereas the electrons are only accepted if they are reconstructed in the central calorimeter, $|\eta_e| < 1.1$, as the electrons in the *ICD* and *EC* regions of the detector are not well enough understood. In the muon channel, an additional veto on the invariant mass of the selected muon and any other loose muon in the event is applied, $70\text{GeV} < m_{\mu\mu} < 110\text{GeV}$. This was found necessary to reduce the background from $Z \to \ell\bar{\ell}$ events, where one of the two muons failed a stronger muon selection requirement.

The cut on the missing transverse energy accounts for the presence of the neutrino. It has been optimized to reject as much background from multijet production as possible

Object	Selection Cut (μ+jets)	Efficiency [%]
Jets	≥ 4 jets with $p_T > 15$ GeV and $\lvert\eta\rvert < 2.5$	54.93 ± 0.30
Muon	medium muon quality $\lvert\eta_\mu\rvert < 2.0$ satisfies cosmic veto tight isolation $p_T > 20$ GeV no second medium muon with $p_T > 15$ GeV Z mass veto	18.52 ± 0.23
Missing E_T	$\not{E}_T > 20$ GeV $\Delta\phi(\mu, \not{E}_T) > 0.1 \cdot \pi - 0.1 \cdot \pi \cdot \not{E}_T/50$ $\Delta\phi(\mu, \not{E}_T) < 0.8 \cdot \pi + 0.2 \cdot \pi \cdot \not{E}_T/30$	16.56 ± 0.22
Electron	no electron with $p_T > 15$ GeV	16.54 ± 0.22
Primary vertex	≥ 3 tracks attached $\lvert z_{PV}\rvert < 60$ cm	16.15 ± 0.22
Event	μ+jets trigger requirement	14.06 ± 0.19

Table 5.4: Preselection cuts applied in the muon channel together with the cumulative efficiencies [69]. The uncertainties on the efficiency result from the limited Monte Carlo statistics used to derive these. A top mass of 175 GeV has been used in the simulation.

while still retaining high efficiency for $t\bar{t}$ events [61, 66].

A good quality of the primary vertex is not only needed for a confirmation that the charged leptons originate from the primary vertex but even more for the application of the b-tag. Events without a good reconstructed vertex are therefore discarded.

The last step in the preselection is the trigger selection. The data samples mentioned earlier in this chapter already contain the trigger selection. In the Monte Carlo events this trigger selection is taken into account by weighting each event with the probability that this individual event passes the trigger requirement. In addition differences between the selection efficiencies in the Monte Carlo and the data, e.g. the efficiency to reconstruct a tight muon given its momentum, are taken into account.

The final selection efficiency for $t\bar{t}$ events with $m_{\text{top}} = 175$ GeV in the muon channel is 0.1406 ± 0.0019 and the corresponding efficiency in the electron channel is 0.1419 ± 0.0018. The uncertainty on these efficiencies includes only the uncertainty due to the limited Monte Carlo statistics used to derive them.

Object	Selection Cut (e+jets)	Efficiency [%]
Jets	≥ 4 jets with $p_T > 15$ GeV and $\lvert\eta\rvert < 2.5$	53.16 ± 0.30
Electron	only 1 *tight* electron with $p_T > 20$ GeV $\lvert\eta_{\text{detector}}\rvert < 1.1$ Likelihood $L > 0.85$, i.e. tight electron	20.80 ± 0.24
Missing E_T	$\not\!\!E_T > 20$ GeV $\Delta\phi(e, \not\!\!E_T) > 2.2 - \not\!\!E_T \cdot 2.2/48.9$	17.56 ± 0.23
Muon	no tight muon with $p_T > 15$ GeV	17.55 ± 0.23
Primary vertex	≥ 3 tracks attached $\lvert z_{PV}\rvert < 60$ cm	17.36 ± 0.22
	matched to central track $\lvert\Delta z(e, PV)\rvert < 1$ cm	
Event	e+jets trigger requirement	14.19 ± 0.18

Table 5.5: Preselection cuts applied in the electron channel together with the cumulative efficiencies [69]. The uncertainties on the efficiency result from the limited Monte Carlo statistics used to derive these. A top mass of 175 GeV has been used in the simulation.

6 Measurement of the W boson helicity

The analysis of the W boson helicity in $t\bar{t}$ decays works as follows: at the beginning additional preselection cuts are applied to significantly reduce the background contamination and to ensure that the $t\bar{t}$ system can be reconstructed.

The remaining background is further suppressed by forming a discriminant out of several variables that exploit the difference in event topology between the $t\bar{t}$ signal and the background events. This discriminant is then used not only to separate signal from background events but also to measure the sample composition. The final event selection is completed by a cut on the discriminant. This cut is optimized to yield the minimal expected statistical uncertainty on the measurement.

An important part of the analysis is the correct modeling of the remaining background events. Here not only the overall normalization of the background is important but also the shape of the distributions, especially the distribution of the cosine of the decay angle θ to avoid an unwanted bias in the measurement.

Having the final dataset selected, the actual measurement of the fraction of positive helicity W bosons can be performed. Templates of the $\cos\theta$ distribution, i.e. the variable that yields a separation between the different helicity states, are formed for the $t\bar{t}$ signal as well as all background processes. The signal templates are constructed by exploiting the negligible interference term between $V-A$ and $V+A$ [79], leading to a linear dependence on f_+. These templates are then compared to the data by calculating a Poisson likelihood. The minimum and the width of the resulting negative log likelihood curve indicates the f_+ value in the data and the corresponding statistical uncertainty. The performance of this analysis has been evaluated by means of ensemble tests, where the templates have been used to analyze mock data sets created using Monte Carlo events.

The dominant systematic uncertainties of the measurement are the uncertainty on the jet energy scale and the uncertainty on the value of the top quark mass. These, as well as many other systematic uncertainties, have been studied using ensemble tests and the combined systematic uncertainty has been taken into account in the final measurement.

The last step of the measurement is the calculation of an upper limit on the fraction

of positive helicity W bosons. This is done using both a frequentist and a Bayesian approach.

6.1 Additional preselection cuts

This analysis makes use of the reconstructed decay angle $\cos\theta$ measured in the W boson rest frame. Therefore the four-vectors of the W boson decaying into a charged lepton and a neutrino as well as of the b quark from the parent top quark must be known. This is achieved by using the minimal χ^2 solution provided by the kinematic fit described in section 4.8. Events where the kinematic fit does not converge are rejected. This corresponds to an inefficiency of about 0.5%.

The additional cut on the b-jet identification greatly reduces the contamination from background events. This is achieved by requiring at least one of the jets to be tagged as b-jet by the presence of a secondary vertex with a decay length significance of more than seven ("tight" b-tag as described in section 4.7). Figure 6.1 shows the strong reduction in the background rate due to this cut. The efficiency for $t\bar{t}$ events to have at least one jet tagged as b-jet is 0.600 ± 0.001 in the electron channel and 0.590 ± 0.001 in the muon channel.

6.2 Background description

Not only $t\bar{t} \to \ell$+jets events pass the preselection but also events from other processes. The dominant source of background events is the production of a W boson associated with four or more jets. Also pure multijet ("QCD") events can pass the preselection under certain circumstances. There is even a background from $t\bar{t}$ production itself: $t\bar{t}$ events decaying into two leptons can produce the same final state due to additional initial and final state radiation.

Even though the electroweak production of single top has not been experimentally observed yet, these events are also expected to pass the preselection. The cross-section for the t-channel production is a factor of two larger compared to the s-channel production. Furthermore the jet multiplicity in the t-channel is higher, leading to a higher efficiency to produce four or more jets as required by the preselection. Therefore only events produced in the t-channel are considered. The expected rate from s-channel production after the preselection of about 0.1 events per lepton channel has been neglected.

There are many more processes, that could potentially produce events passing the preselection, for example the production of diboson events. However, as their rate is

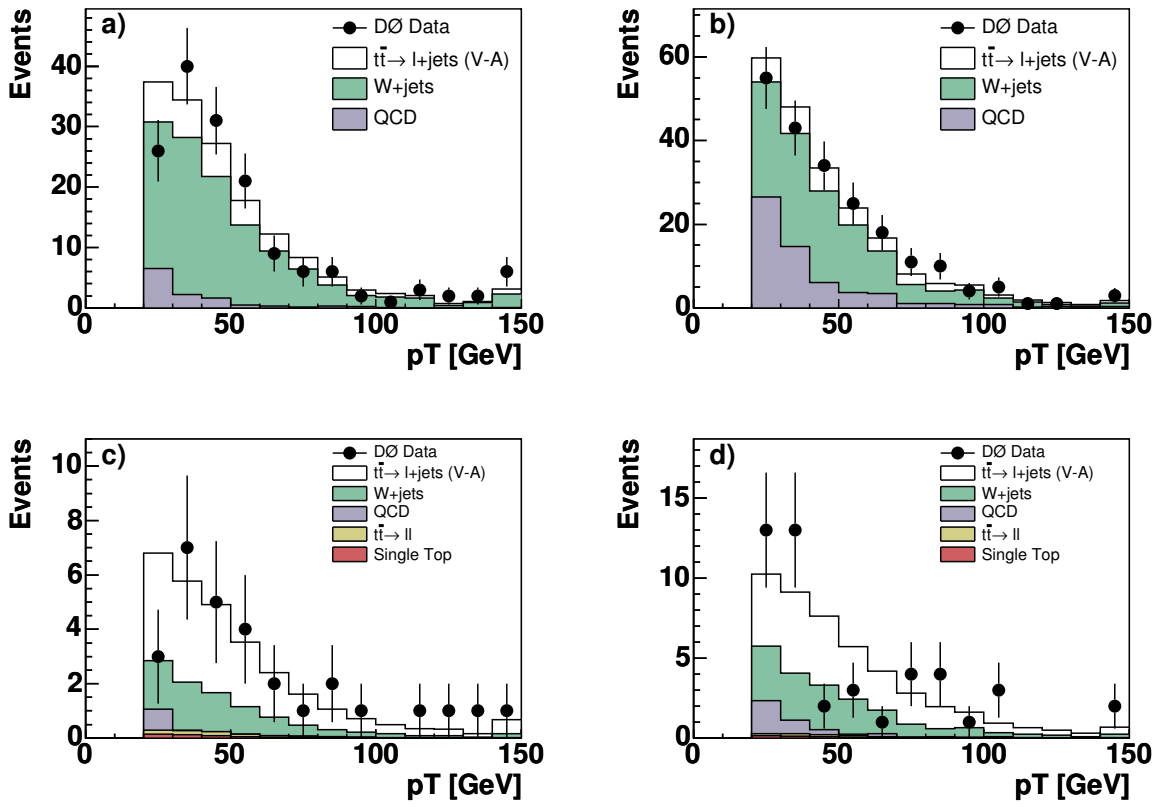

Figure 6.1: a) muon p_T and b) electron p_T before the b-tag requirement, c) muon p_T and d) electron p_T after the b-tag requirement. The usage of the b-tag information provides a large reduction in the number of background events while keeping more than 50% of the $t\bar{t}$ events.

expected to be less than 0.1 events per channel [69], these background processes are not considered in this analysis.

The determination for the two most important background processes, $W+$jets and QCD, are described in detail in the following two subsections. The background events from $t\bar{t} \to \ell\bar{\ell}$ and from t-channel single top production are estimated from the theoretical cross-section for these processes, $\sigma_{t\bar{t}} = 7$ pb and $\sigma_t = 1.98$ pb, and the corresponding preselection efficiencies.

6.2.1 Multijet production

The background due to multijet production is estimated based on real data events. This is necessary because of the huge cross-section for this process and the fact, that events passing the preselection are in general special events. These are often located in

the tails of distributions and imperfectly modeled by the Monte Carlo simulation. One example being the hard fragmentation of a b quark into a muon, leaving not enough energy for other particles to be reconstructed as jet and therefore faking an isolated lepton. Or a jet can have a high electromagnetic fraction and a low multiplicity of charged particles and only one of these charged particles is reconstructed. This could fake an electron candidate.

It is impossible to generate enough Monte Carlo events to simulate all these effects and to verify that the tails are correctly modeled. Therefore this background is studied in data. This has the advantage, that the systematic uncertainties due to this background are smaller. However, a disadvantage is the increase of the statistical uncertainty due to the limited data statistics.

Two methods to estimate the multijet background in data that are used are explained in the following paragraphs: the Matrix Method [80, 81] and a method which explicitly selects multijet events before applying the b-tag. These events are then reweighted to account for the influence of the b-tag on the jet energy and η distributions.

Matrix Method

The main idea behind the Matrix Method is to select two samples of events, a loose sample and a tight sample, the latter being a complete subset of the first. The samples differ in the selection of the lepton. The tight sample is obtained after the full preselection, whereas for the loose sample the cuts on the muon isolation or the electron likelihood have not been applied. This enriches the loose sample in multijet events.

The number of events in the loose and the tight sample, N_{loose} and N_{tight}, can now be expressed by the number of multijet events, N_{QCD}, and the sum of $t\bar{t}$ and $W+$jets events, N_{W+tt}:

$$\begin{aligned} N_{loose} &= N_{QCD} + N_{W+tt} \\ N_{tight} &= \epsilon_{QCD} \cdot N_{loose} + \epsilon_{sig} \cdot N_{tight} \,, \end{aligned} \tag{6.1}$$

where ϵ_{sig} and ϵ_{QCD} are the relative efficiencies for real isolated leptons from a decay of a W boson and for jets faking an isolated lepton, respectively. The efficiency ϵ_{sig} for $t\bar{t}$ and $W+$jets events is measured using Monte Carlo, whereas the efficiency ϵ_{QCD} for multijet events is measured in an independent data sample where the $\not\!\!E_T$ is required to be less than 20 GeV to enhance the multijet contribution and to ensure the orthogonality to the dataset used in the analysis. Table 6.1 lists these efficiencies for both channels.

The equation system 6.1 can now be solved separately for each bin i of any given distribution yielding the shape of the multijet events and the overall normalization by

Channel	ϵ_{QCD}	ϵ_{sig}
μ+jets	0.082 ± 0.047	0.806 ± 0.008
e+jets	0.16 ± 0.01	0.817 ± 0.011

Table 6.1: Efficiencies for the tight selection in both channels. ϵ_{QCD} is the efficiency for QCD events to pass the tight selection and ϵ_{sig} is the efficiency for real leptons from $W+$ jets and $t\bar{t}$ events to pass the tight selection. These numbers are derived in [61] for the electron channel and in [66] for the muon channel.

integrating over all bins i:

$$N^i_{QCD} = \frac{\epsilon_{sig} N^i_{loose} - N^i_{tight}}{\epsilon_{sig} - \epsilon_{QCD}} \tag{6.2}$$

For the dataset used in this analysis this yields the following numbers for the normalization of the multijet background: 3.7 ± 1.8 multijet events in the electron channel and 0.7 ± 0.6 in the muon channel. The corresponding number of tight (loose) data events used in this calculation are: 29 (44) events in the muon channel and 46 (75) events in the electron channel.

The low number of events in the loose and tight samples give rise to large uncertainties on the predicted shape and normalization for the multijet events. Therefore the matrix method will only be used in this analysis to constrain the normalization of the multijet events but not for the shape. The prediction for the shape of these events is done using the method explained in the next paragraph.

Reweighting untagged QCD events

In order to reduce the statistical uncertainty on the shape of the multijet distributions a different approach is used. Instead of using the Matrix Method to estimate the shape from two different data sets, a real selection of QCD events from the dataset is performed. The same selection as for the data is used with two exceptions:

- the selected events need to fulfill the loose lepton selection but fail the tight selection. This provides a high purity for QCD events.
- the b-tag requirement is not applied to increase the selection efficiency for QCD events.

This procedure results in 169 events in the muon channel and 340 events in the electron channel. As these events are selected before requiring any b-tag in the event, they need to be reweighted to account for the p_T and η dependence of the b-tag.

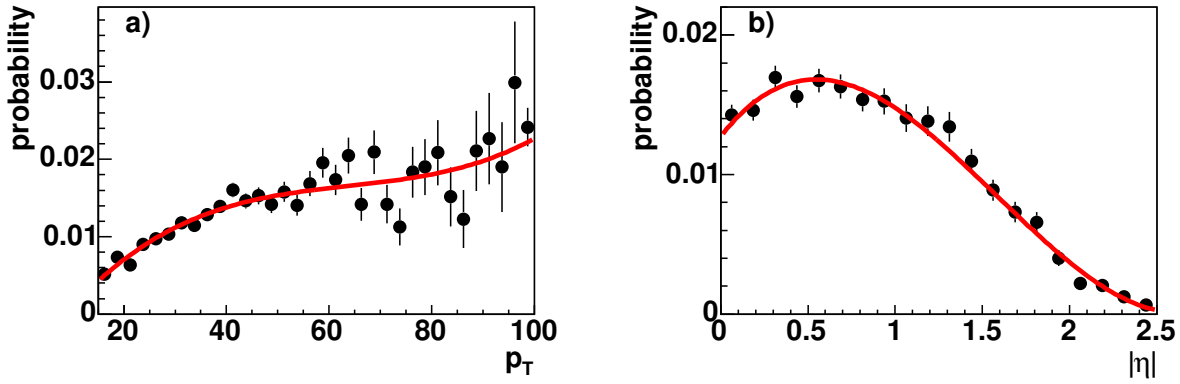

Figure 6.2: Tag rate functions for the QCD background derived in the electron channel: versus jet p_T (left) and versus the detector η of the jet (right).

This reweighting is performed in a similar way as the application of the b-tag on the Monte Carlo events as described in section 4.7.2. However, the parameterization is not split into a taggability part and a b-tag part but instead an inclusive parameterization is derived.

Only the electron channel is used to derive the b-tag parameterization as there the statistics is higher and the muon channel can be used to cross check the parameterization. The events are selected using the same preselection as for the signal sample except for the following changes:

- there should be less than four jets,
- the kinematic fit does not need to converge,
- the $\Delta\phi$ cut between the electron and the missing E_T is removed as well as the cut on $\not\!\!E_T$ itself and
- the cut on the electron likelihood is reversed.

These changes ensure that the sample contains dominantly QCD events. The selected events are split into two samples, untagged and tagged, depending on the presence of at least one b-tag in the event. By dividing the tagged by the untagged distributions and fitting the result with a third order polynomial, the parameterization is obtained as shown in Figure 6.2.

6.2.2 W+jets

The W+jets background is taken from Monte Carlo simulation. The samples described in section 5.3.2 are mixed according to their theoretical leading order cross

section (Table 5.3 on page 73). Only the relative cross section is used because the overall normalization is later determined using data. As already mentioned only events are used where the original partons produced by ALPGEN could be matched to reconstructed jets in order to avoid double counting. Table 6.2 lists the relative fractions of the different $W+$ jets samples after the preselection but before requiring at least one b-tag, and after the b-tag requirement.

After the b-tag requirement the $W+$ jets background is dominated by events containing b quarks (WbbJj) while before the light quark contribution dominates.

6.3 Signal to background discrimination

The cuts applied so far are designed to select events with a real W boson, heavy flavor jets and an event topology compatible with a $t\bar{t}$ event with $m_t = 175$ GeV. The last requirement is not a very strong one as almost all $W+$ jets events have at least one jet combination which leads to a successful kinematic fit.

Since the signal to background ratio is only about 1 in both channels, a further reduction of the dominant background, $W+$ jets, is desirable. This is done by combining several variables that provide a distinction between $t\bar{t}$ and $W+$ jets into a likelihood discriminant.

6.3.1 Input variables

Based on the experience from previous top quark measurements [82, 83] performed on Run I data, ten possible input variables are considered. To reduce the dependence on systematic uncertainties from the modeling of soft radiation, e.g. the underlying event, only the four leading jets in p_T are used in the calculation of these variables.

Two out of the ten variables are based on the normalized quadratic momentum tensor

Channel	before b-tag				after b-tag			
	$Wjjjj$	$WbbJj$	$WccJj$	$Wcjjj$	$Wjjjj$	$WbbJj$	$WccJj$	$Wcjjj$
μ+jets	80.9%	5.7%	9.2%	4.2%	17.7%	51.8%	23.6%	6.9%
e+jets	80.9%	5.7%	9.2%	4.2%	17.7%	51.5%	24.0%	6.8%

Table 6.2: Expected fraction of each W+jets flavor after preselection for each channel before (left) and after (right) requiring at least one b-tag in the event. In the above tables j is any of u, d, s, g and J is any of u, d, s, c, g partons.

$\mathcal{M}$ defined as

$$\mathcal{M}_{ij} = \frac{\Sigma_o p_i^o p_j^o}{\Sigma_o |\vec{p^o}|^2}, \tag{6.3}$$

where $\vec{p^o}$ is the momentum-vector of a reconstructed object o, and i and j are Cartesian coordinates. The objects included in the sum are the jets and the lepton from the W boson decay. These have the best discrimination power between $t\bar{t}$ and W+jets events. By standard diagonalization of $\mathcal{M}_{ij}$, three eigenvalues $\lambda_1 \geq \lambda_2 \geq \lambda_3$ are found, with $\lambda_1 + \lambda_2 + \lambda_3 = 1$.

The ten input variables are the:

Sphericity, defined as:

$$S = \frac{3}{2}(\lambda_2 + \lambda_3) \, . \tag{6.4}$$

The sphericity is essentially a measure of the summed $p_\perp^2$ with respect to the event axis; a 2-jet event corresponds to $S \approx 0$ and an isotropic event to $S \approx 1$. $t\bar{t}$ events are quite isotropic as is typical for the decay of a heavy object produced close to threshold. W+jets and QCD events are less isotropic, primarily due to the fact that the jets in these events arise from initial and final state radiation.

Aplanarity is a measure of the flatness of the event and is defined as

$$\mathcal{A} = \frac{3}{2}\lambda_3 \, , \tag{6.5}$$

Due to the arguments given for the sphericity large values of $\mathcal{A}$ are an indication of spherical events, whereas small values correspond to more planar events.

$\boldsymbol{H_T}$ is the sum of the transverse jet energies

$$H_T = \sum_{jet=1}^{N_{jets}=4} E_T(jet) \, . \tag{6.6}$$

It is a measure of the transverse hadronic energy in the event: due to the high mass of top quarks this variable will on average be higher for top events than for background events.

$\boldsymbol{H_T^W}$ is a measure of the total transverse energy in the event. It is defined as the sum of the transverse jet energies plus the transverse energy of the W boson

$$H_T^W = E_T(W) + \sum_{jet=1}^{N_{jets}=4} E_T(jet), \tag{6.7}$$

$\boldsymbol{H_T^3}$ is defined as

$$H_T^3 = H_T - E_T(jet1) - E_T(jet2), \tag{6.8}$$

where $jet1$ and $jet2$ are the leading and second-leading jets, respectively.

$\boldsymbol{H'_{T2}}$ is a H_T based variable which is modified to make it less sensitive to the jet energy scale by dividing by the sum of longitudinal jet, lepton and neutrino energies:

$$H'_{T2} = \frac{H_T - E_T(jet1)}{p_z(l) + p_z(\nu) + \sum_{jet=1}^{N_{jets}=4} p_z(jet)} \,. \tag{6.9}$$

Centrality is the ratio of transverse and total sum of the jet energies:

$$C = \frac{H_T}{H_E} = \frac{\sum_{jet=1}^{N_{jets}=4} E_T(jet)}{\sum_{jet=1}^{N_{jets}=4} E(jet)}, \tag{6.10}$$

where H_E is the total jet energy in the event. The top quarks are produced nearly at rest and the decay of the top quarks will produce spherical events with a higher transverse energy compared to the background.

$\boldsymbol{K'_{Tmin}}$ provides a measure of the minimum jet p_T relative to another and is defined as the distance in $\eta - \phi$ space between the closest pair of jets, ΔR_{jj}, multiplied by the p_T of the lowest-p_T jet in the pair, $p_T^{\min}$, and divided by the transverse energy of the reconstructed W boson:

$$K'_{Tmin} = \Delta R_{jj}^{\min} \cdot \frac{p_T^{\min}}{E_T^W} \,. \tag{6.11}$$

$\boldsymbol{m_{jj}^{min}}$ is the smallest invariant mass of any two jets in the event. In $t\bar{t}$ events without additional initial-/final state radiation this mostly corresponds to the mass of the W boson decaying into a quark and an antiquark. In W+ jets and QCD events this mass is lower as there the jets arise from initial and final state radiation.

HitFit $\boldsymbol{\chi^2}$ is the χ^2 from the kinematic fit described in section 4.8. It provides a measure on how consistent the event is with the hypothesis of a $t\bar{t}$ event with a top quark mass of 175 GeV.

6.3.2 Optimization of the likelihood discriminant

To obtain the optimal separation between $t\bar{t}$ and W boson multijet production every possible combination of up to seven input variables, i.e. nearly 1000 different combinations, has been tested using efficiency times purity as figure of merit.

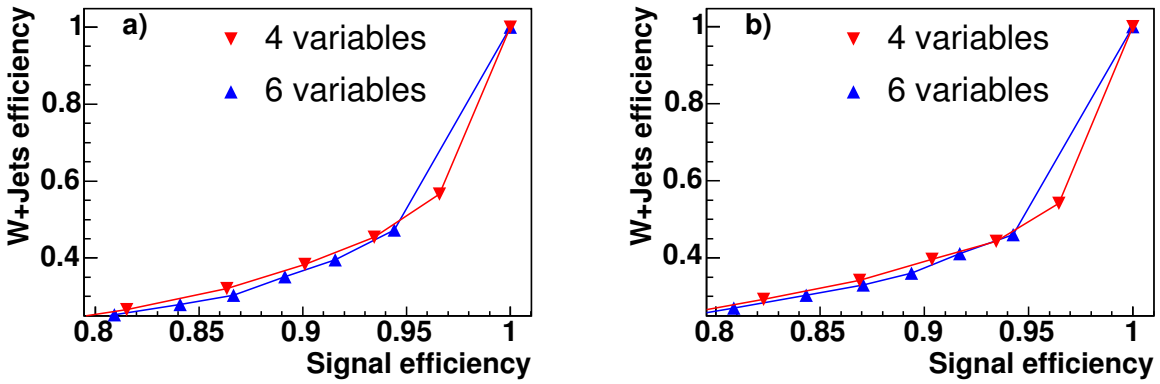

Figure 6.3: Comparison of the likelihood discriminants in the muon (a) and the electron channel (b). For each likelihood discriminant the efficiency for $WbbJj$ is plotted versus the $t\bar{t}$ efficiency. The differences between the two likelihood discriminants is very small. The lines connecting the points are just to guide the eye and are not meant as interpolation (especially not at efficiencies close to unity).

The best separation is obtained by a likelihood discriminant using six input variables: Aplanarity, minimal dijet mass, HitFit χ^2, H_T, H_T^{20} and H'_{T2}. Here three out of six variables are H_T based variables and therefore sensitive to the jet energy scale. The second best likelihood discriminant contains only four variables: H_T, centrality, minimal dijet mass and the χ^2 from HitFit. The separation power of this likelihood discriminant is very close to the optimal discriminant as can be seen in Figure 6.3. This fact together with the potentially higher jet energy scale systematic uncertainty of the likelihood discriminant with six input variables led to the decision to use the likelihood with only four input variables.

A data to Monte Carlo comparison of the four selected input variables can be seen in Figure 6.4: the agreement between data and Monte Carlo is very good. Also the remaining six input variables that have not been used in the discriminant show a good agreement as can be seen from Figure 6.5.

To make sure that the likelihood discriminant does not introduce a bias in the measurement, the correlations between the chosen input variables and the sensitive variable $\cos\theta$ should be small. Table 6.3 lists these correlations and as can be seen, none of the input variables shows a strong correlation with $\cos\theta$.

6.3.3 Construction of the discriminant

The likelihood discriminant is built in the following way:

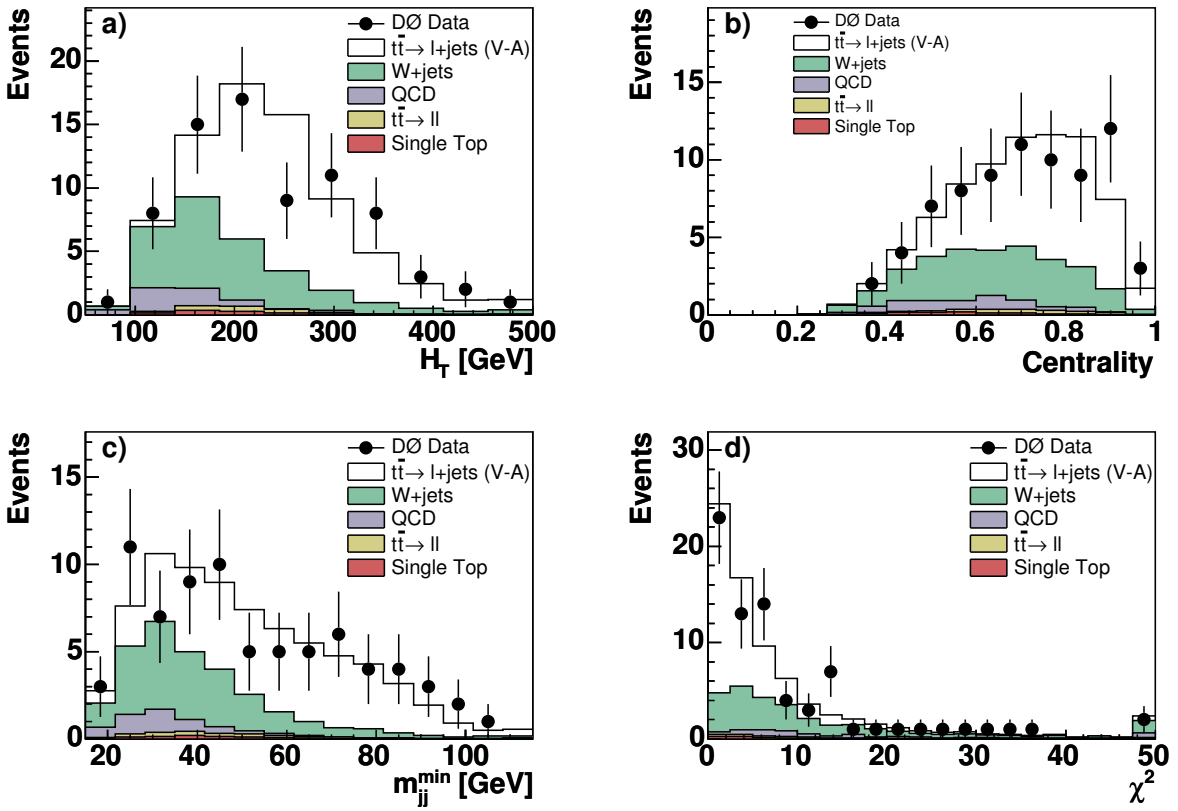

Figure 6.4: Input variables used in the likelihood discriminant after all preselection cuts and after requiring at least one b-tag: a) H_T, b) centrality, c) minimal dijet mass, and d) the χ^2 from the kinematic fit. Both channels, muon and electron, are added in these plots.

Variable	Centrality	H_T	m_{min}	χ^2	$\cos\theta$
Centrality	—	0.320	-0.012	0.008	-0.022
H_T	0.343	—	0.410	0.061	0.065
m_{min}	-0.002	0.413	—	-0.007	0.052
χ^2	0.004	0.121	-0.023	—	0.078
$\cos\theta$	-0.034	0.088	0.062	-0.006	—

Table 6.3: Correlation coefficient between the input variables for the likelihood discriminant and the cosine of the decay angle. Values above the diagonal are for the muon channel and values below the diagonal are for the electron channel.

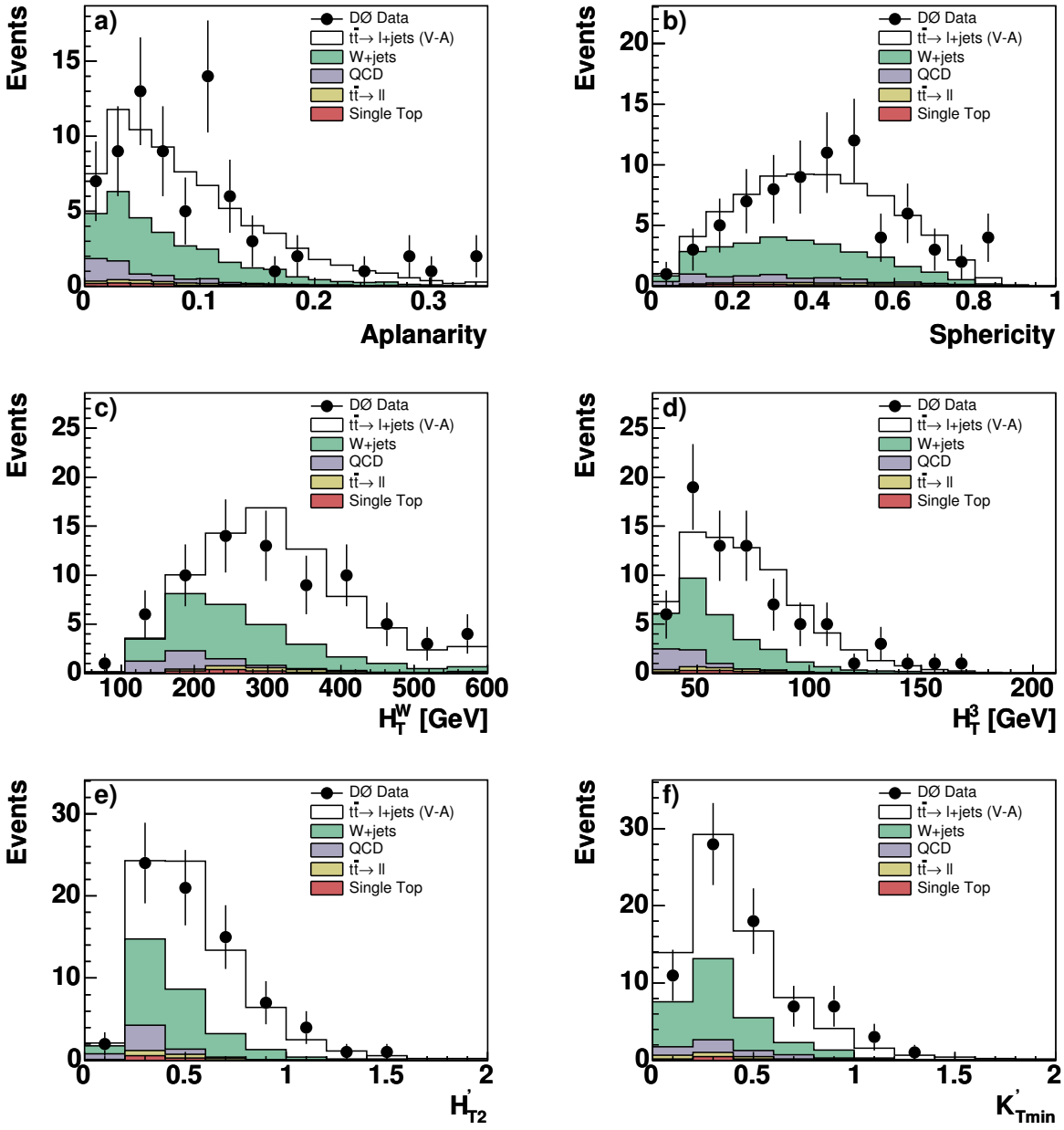

Figure 6.5: Possible other input variables for the likelihood discriminant after all preselection cuts and after requiring at least one b-tag: a) aplanarity, b) sphericity, c) H_T^W, d) H_T^3 e) H'_{T2}, and f) K'_{Tmin}. Both channels, muon and electron, are combined in these plots.

- The variables are transformed using arbitrary functions in order to allow for a convenient fit of the logarithm of S/B with a polynomial function [84]. The functions used are:
  - $\exp(-2 \cdot C)$
  - $\ln(H_T)$
  - $\sqrt{m_{min}}$
  - $\ln(\chi^2)$
- The distributions are normalized to unity and the ratio of signal ($t\bar{t}$) over background (W+jets) is built for each of the four distributions. Only the $W + b\bar{b}$ sample is used as background in this construction as it is the dominant background source after the b-tag requirement. This does not reduce the performance of the likelihood discriminant: even though the likelihood is built to discriminate only against $W + b\bar{b}$ events, it rejects also the other W+jet events with nearly the same efficiency.

  This is the only part of the analysis where only one W+jet flavor is used. All other plots and templates contain the full set of W+jets samples.
- The logarithm of the ratios is built and fitted with a polynomial. Fitting the logarithm simplifies the fit function and symmetrizes the errors on the points.
- The data in the tail of a distribution is consolidated including over- and underflow bins.
- The likelihood discriminant $\mathcal{D} = S/(S+B)$ can be written as

$$\mathcal{D} = \frac{\exp\left(\sum_i (\ln \frac{S}{B})^i_{\text{fitted}}\right)}{\exp\left(\sum_i (\ln \frac{S}{B})^i_{\text{fitted}}\right) + 1}\,, \tag{6.12}$$

  where $(\ln \frac{S}{B})^i_{\text{fitted}}$ is the fit to $\ln(\frac{\mathcal{P}^i_{\text{t}\bar{\text{t}}}}{\mathcal{P}^i_{\text{W}}})$ for each variable i that is used to build the discriminant, $\mathcal{P}^i_{\text{t}\bar{\text{t}}}$ and $\mathcal{P}^i_{\text{W}}$ are the probabilities for the variable i to be $t\bar{t}$ signal and W+jets background, respectively.

Figure 6.6 shows the normalized distributions of the input variables and the fit to the ratio of signal to background in the electron channel. The corresponding plots for the muon channel are very similar and are therefore not shown.

The resulting distributions of the discriminant for the three main event classes, $t\bar{t}$, $W+$jets and QCD, are shown in Figure 6.7 for the muon channel. The plots for the $t\bar{t}$ and $W+$jets events in the electron channel are not shown as they are nearly identical. In addition a comparison between the reweighted untagged QCD events is shown

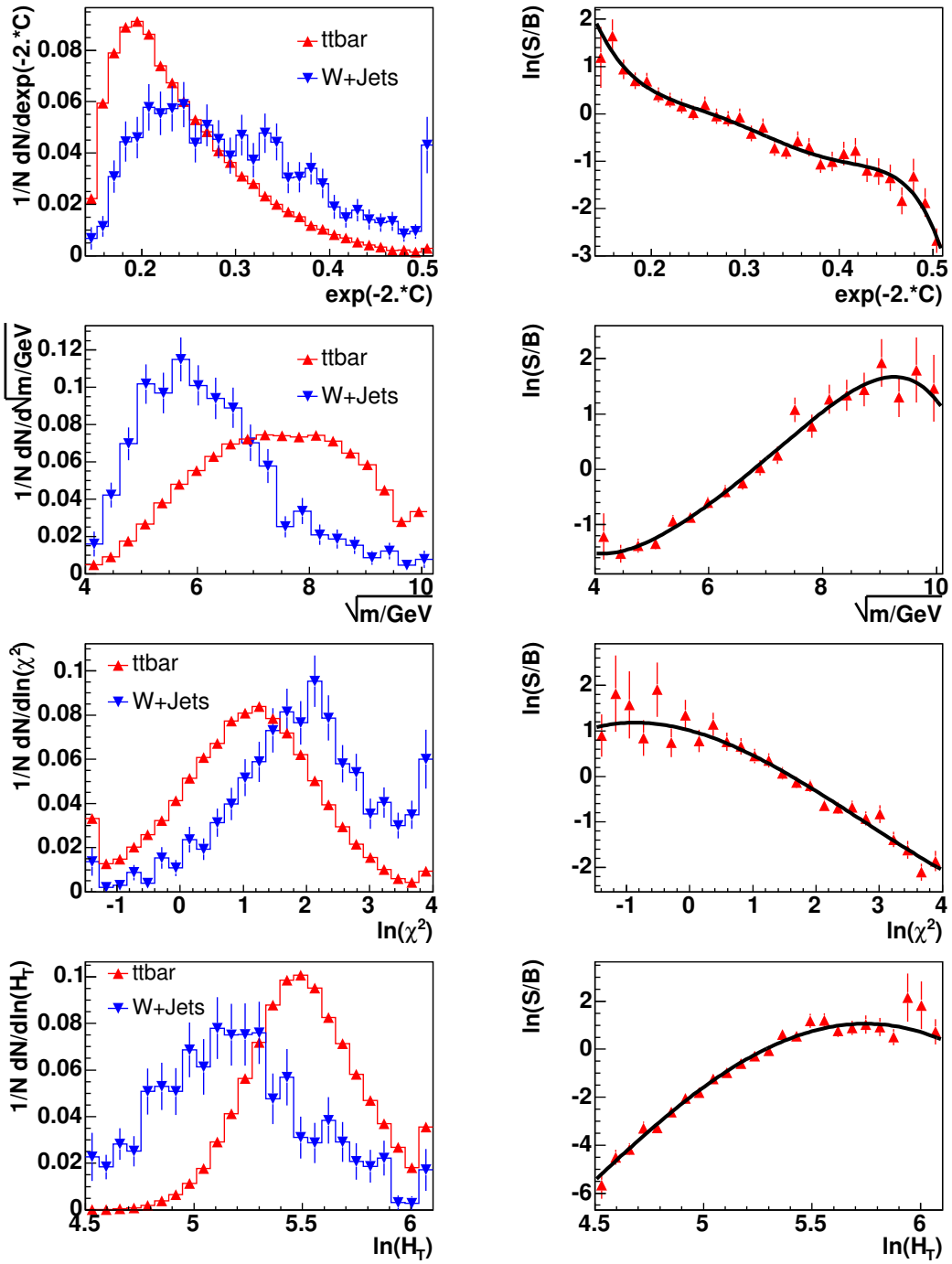

Figure 6.6: Normalized distributions for the input variables used in the likelihood discriminant (left) and the fit to the logarithm of signal over background (right) in the electron channel after all preselection cuts and after requiring at least one b-tag. From top to bottom: centrality, minimal dijet mass, the χ^2 from the kinematic fit and H_T. The first and last bin are under- and overflow bins, respectively.

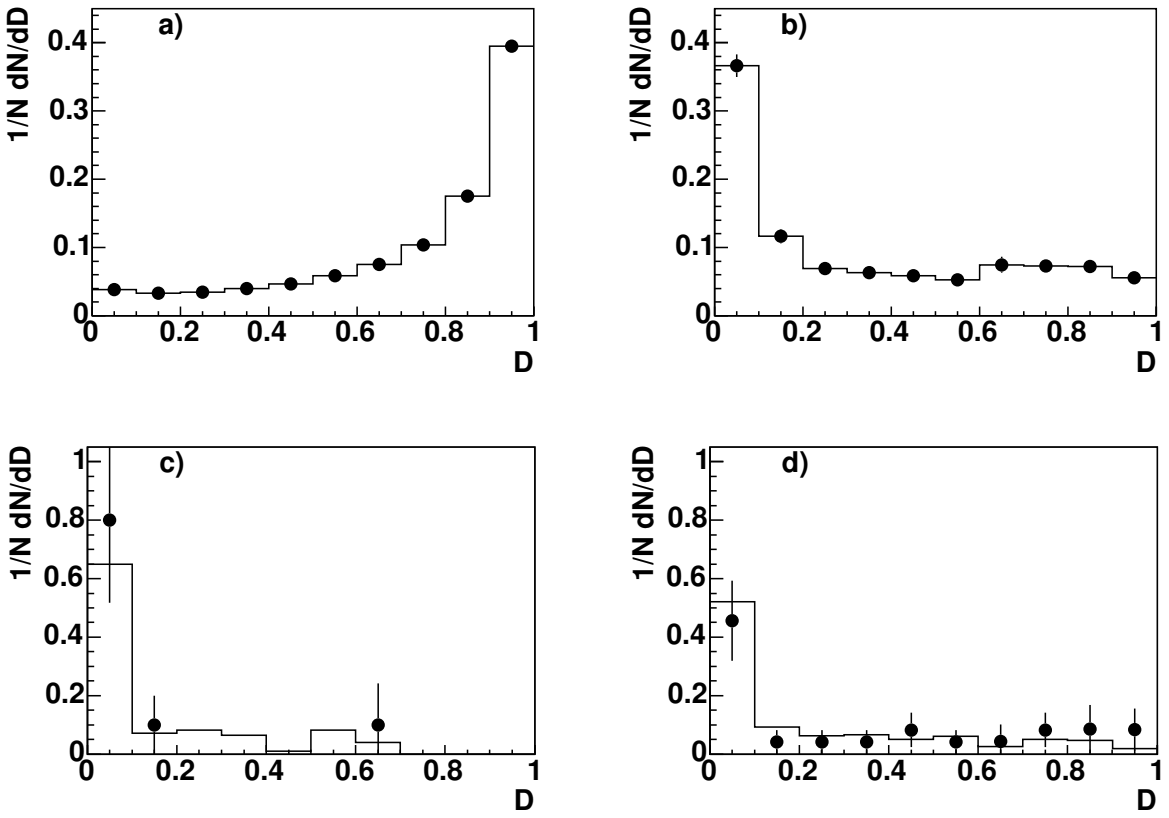

Figure 6.7: Templates of the likelihood discriminant for the muon channel (top). The distribution on the left refers to $t\bar{t}$ and the one on the right to W+jets. On the bottom the likelihood discriminant for QCD events is shown: in the muon channel (left) and in the electron channel (right). The histograms correspond to the reweighted untagged QCD events. For comparison the tagged QCD events are shown as dots.

with the tagged events. The agreement there is very good and gives confidence that the method described in section 6.2.1 gives an accurate description of the QCD background.

6.3.4 Measuring the sample composition

The composition of the dataset can now be derived by performing a fit to the likelihood discriminant. Since the sum of W+jets and $t\bar{t}$ events is already known from the matrix method a likelihood $\mathcal{L}_D$ can be constructed containing this constraint [66].

Channel	$t\bar{t} \to \ell$+jets	W+jets	QCD	$t\bar{t} \to \ell\bar{\ell}$	single top
μ+jets	18.8 ± 5.3	8.0 ± 4.5	0.8 ± 0.4	0.73 ± 0.02	0.50 ± 0.02
e+jets	25.8 ± 7.1	15.6 ± 7.1	3.7 ± 1.1	0.70 ± 0.02	0.52 ± 0.02

Table 6.4: Fitted number of events for the different signal and background samples in each of the two channels. Only $t\bar{t} \to \ell$+jets, W+jets and QCD is fitted. The other samples are kept at the predicted values assuming the theoretical cross sections.

This is realized by defining the likelihood as follows:

$$\mathcal{L}_{\mathcal{D}}(N_{t\bar{t}}, N_W, N_{\text{QCD}}) = \left[\prod_i P(n_i^{\text{obs}}, \nu_i)\right] \cdot P(N_{\ell-t}^{\text{obs}}, N_{\ell-t}) \tag{6.13}$$

where $P(n, \nu)$ generically denotes the Poisson probability density function for n observed events given an expectation of ν. The product in the first term of Eq. (6.13) runs over all bins, i, in the likelihood discriminant. The second term of Eq. (6.13) is a Poisson constraint on the observed number of events in the loose sample minus the number of events in the tight sample, $N_{\ell-t}^{\text{obs}} = N_\ell - N_t$. $N_{\ell-t}$ is the predicted number of events in the "loose-tight" sample. This effectively incorporates the Matrix Method into the likelihood: it constrains the number of QCD events to the prediction from the Matrix Method. This is necessary as the shapes for QCD and W+jets are similar and the likelihood discriminant therefore cannot distinguish between those two. Having the Matrix Method inside the fit instead of externally calculating the number of QCD events has the advantage that the fit can still change this number slightly in order to improve the agreement between data and Monte Carlo in the distribution of the likelihood discriminant.

The contribution from single top production and from $t\bar{t}$ pairs decaying into two leptons are too small to be fitted. Instead these contributions are fixed using the theoretical cross sections for these processes.

Figure 6.8 shows the distribution of the likelihood discriminant obtained in data after all preselection cuts. There are 46 data events in the electron and 29 data events in the muon channel. The result from the fit is summarized in Table 6.4.

As a cross-check that the likelihood discriminant has a reasonable Monte Carlo description, it has been applied to the data before requiring at least one b-tag. Figure 6.9 shows that the agreement between data and Monte Carlo is reasonable.

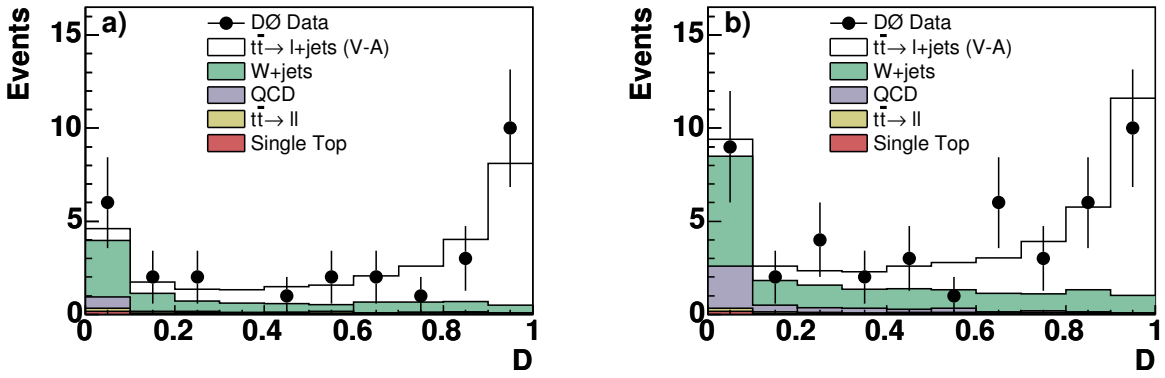

Figure 6.8: Likelihood discriminant after all preselection cuts in a) the muon channel and b) the electron channel. The $t\bar{t}$, $W+$jets and QCD samples are normalized to the result from the fit to the likelihood discriminant whereas the $t\bar{t}$ decaying into two leptons as well as the single top events are normalized using the theoretical cross section for these processes.

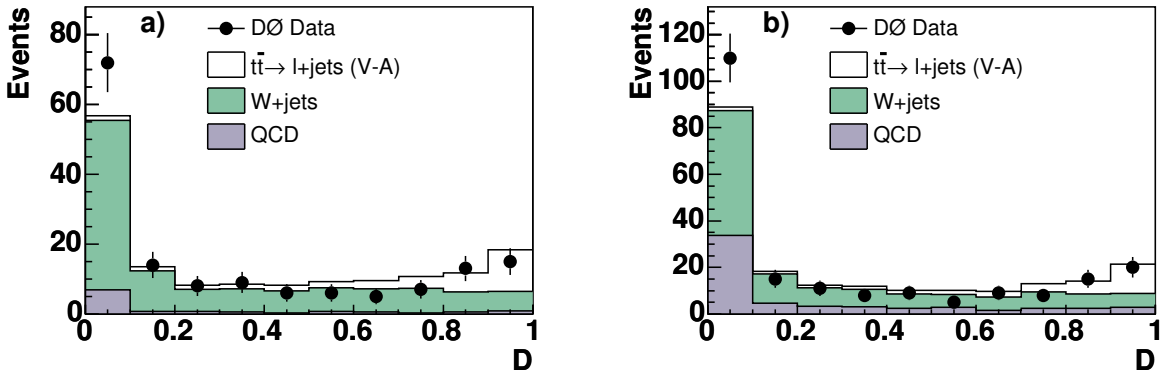

Figure 6.9: Likelihood discriminant after all preselection cuts except for the b-tag requirement in a) the muon channel and b) the electron channel. The distributions show a reasonable agreement between data and Monte Carlo. The $W+$jets Monte Carlo has been normalized to the data minus the estimated QCD contribution obtained from the matrix method and minus an expected $t\bar{t}$ contribution of 7 pb.

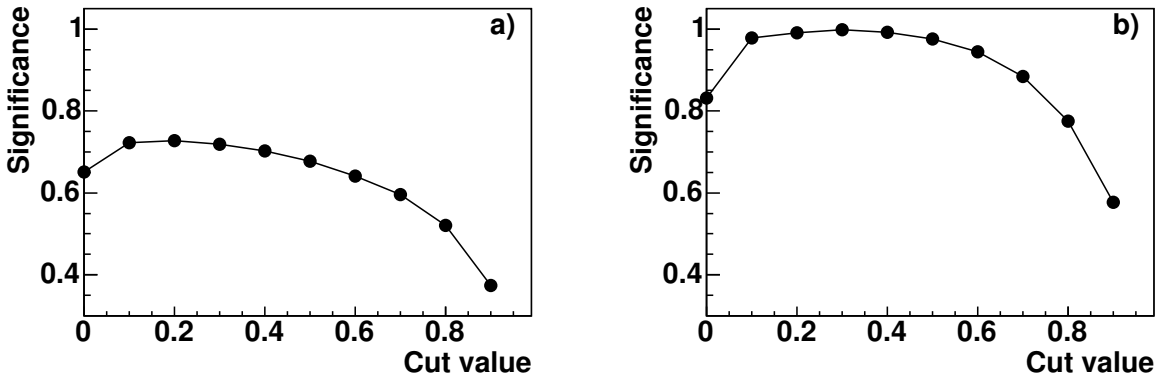

Figure 6.10: Optimization of the cut on the likelihood discriminant in the muon (left) and electron channel (right). The optimal cut values are: $\mathcal{L} \geq 0.2$ in the muon and $\mathcal{L} \geq 0.3$ in the electron channel.

6.4 Final selection

The likelihood discriminant can not only be used to measure the sample composition but it also provides a tool to further reduce the background contamination by applying a cut on the output of the likelihood discriminant.

To maximize the performance of the analysis, this cut needs to be tuned to optimize the statistical sensitivity of the analysis. One possible criterion for this optimization is the statistical significance between the V+A and the V-A scenarios, where significance is defined here to be

$$S = \sum_{i=1}^{N_{bins}} \frac{(n_{i,V-A} - n_{i,V+A})^2}{n_{i,V-A} + n_{i,V+A}}. \tag{6.14}$$

The sum runs over all bins in the decay angle histogram and n_i is the content of bin i after adding up signal and background.

Figure 6.10 shows the significance versus the likelihood cut. In the muon channel the optimal cut is at $\mathcal{L} \geq 0.2$, whereas in the electron channel the optimal cut is at $\mathcal{L} \geq 0.3$. To keep the analysis similar for both muon and electron channel a cut at $\mathcal{L} \geq 0.25$ is chosen for both channels.

Another way of optimizing the cut is to perform the whole analysis for each chosen cut value and compare the expected statistical uncertainty or the expected limit obtained. This procedure has also been carried out and the result is identical to the one obtained with the previously described method: the optimal cut is at $\mathcal{L} \geq 0.25$.

The corresponding efficiencies are listed in Table 6.5. The Monte Carlo normalization after this cut is based on the numbers obtained from the fit to the likelihood discriminant and the efficiencies of this cut. Table 6.6 summarizes the predicted number of

Channel	V-A	V+A	$t\bar{t}$ combined
μ+jets	0.916 ± 0.012	0.909 ± 0.011	0.912 ± 0.008
e+jets	0.919 ± 0.012	0.916 ± 0.011	0.917 ± 0.008

Channel	$Wjjjj$	$WbbJj$	$WccJj$	$Wcjjj$
μ+jets	0.64 ± 0.07	0.41 ± 0.04	0.45 ± 0.06	0.47 ± 0.04
e+jets	0.63 ± 0.10	0.46 ± 0.04	0.51 ± 0.06	0.46 ± 0.04

Channel	QCD	$t\bar{t} \to \ell\bar{\ell}$	single top
μ+jets	0.28 ± 0.14	0.64 ± 0.05	0.49 ± 0.04
e+jets	0.35 ± 0.09	0.65 ± 0.05	0.52 ± 0.03

Table 6.5: Efficiencies for the likelihood cut in both channels for the signal and the different background samples. The V-A and the V+A efficiencies agree within their statistical uncertainty. Therefore all seven signal samples are combined to reduce the uncertainty on the $t\bar{t}$ efficiency.

Channel	$t\bar{t} \to \ell$+jets	W+jets	QCD	$t\bar{t} \to \ell\bar{\ell}$	single top
μ+jets	17.1 ± 4.8	3.7 ± 2.1	0.2 ± 0.2	0.47 ± 0.03	0.26 ± 0.01
e+jets	23.7 ± 6.5	7.8 ± 3.5	1.3 ± 0.5	0.46 ± 0.03	0.27 ± 0.01

Table 6.6: Predicted number of events for the different signal and background samples in each of the two channels after the cut on the likelihood discriminant.

events for each sample. In the data 19 events remain in the muon channel and 33 events in the electron channel.

As the distributions of the input variables to the likelihood discriminant are well described in the Monte Carlo and also the likelihood discriminant itself shows a good agreement with the data, it is not expected that the cut on the likelihood discriminant disturbs this good agreement. To confirm this statement, the agreement between data and Monte Carlo has been checked after the final event selection as can be seen in Fig. 6.11.

6.5 Analysis method

In principle, the $\cos\theta$ distribution obtained in data could be fit with the theoretical expectation as discussed in section 2.2.4. However, due to reconstruction and acceptance effects the $\cos\theta$ distribution is distorted. Instead of correcting the data back to the parton level and fitting the corrected $\cos\theta$ distribution after background subtraction, this analysis uses templates in $\cos\theta$ after the full reconstruction and selection

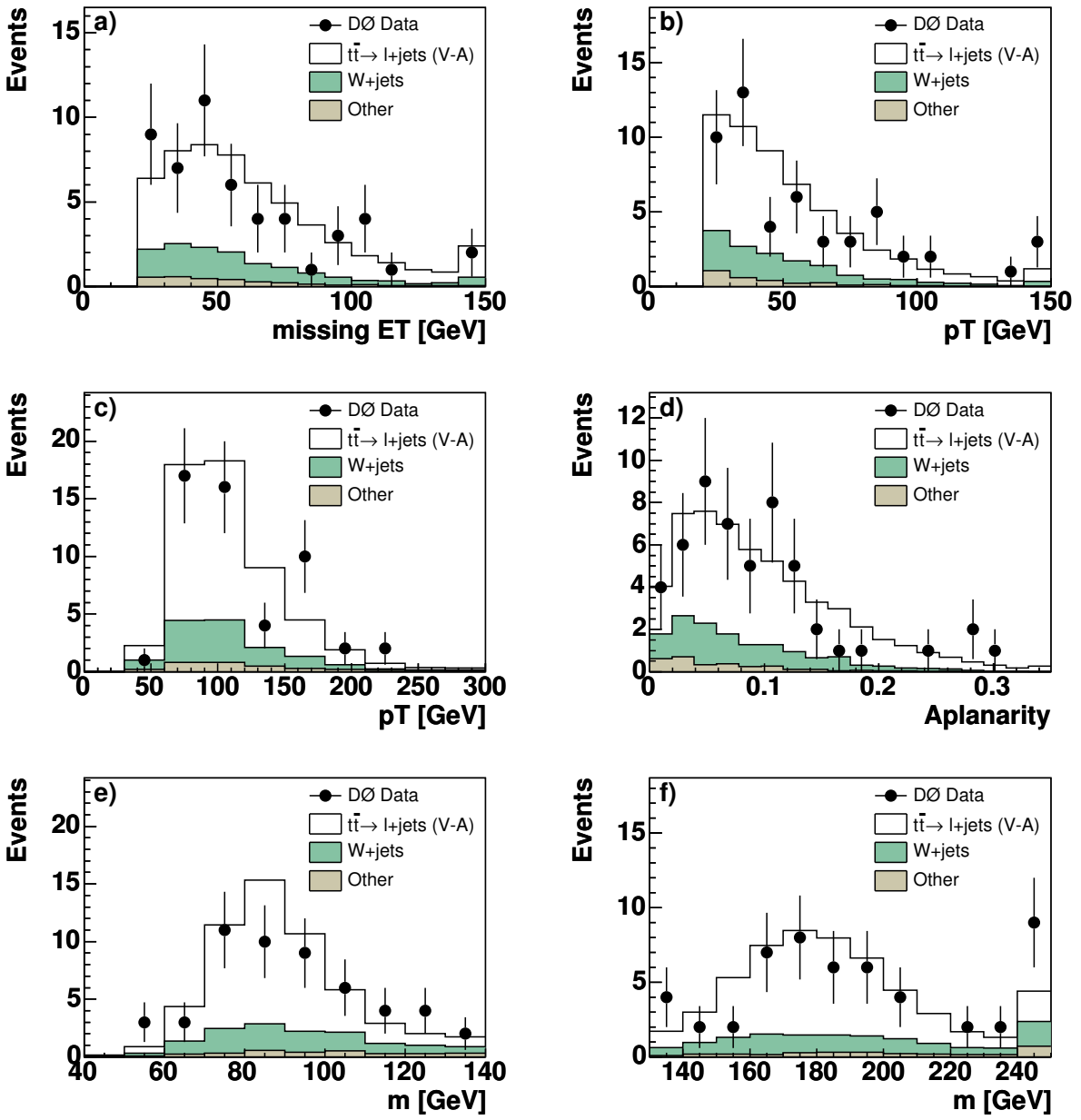

Figure 6.11: Comparison between data and Monte Carlo after the final selection. The electron and the muon channel are combined in these plots: a) missing transverse energy in the event; b) the p_T of the lepton; c) the p_T of the leading jet in the event; d) the aplanarity; e) the invariant mass of the two jets associated by the kinematic fit to the W boson decaying into a quark-antiquark pair and f) the invariant mass of the three jets associated by the kinematic fit to the top quark decaying into three jets. In the last two plots the kinematic fit was only used to select the jets and not to make a kinematic constraint on the W boson or top quark mass.

and compares these with the one obtained in data.

The decay angle templates are created by using the output from the kinematic fit to calculate $\cos\theta$. For the signal templates, an interpolation technique can be used to improve the statistical precision of these templates.

The performance of this analysis method can then be tested by performing a large number of toy experiments, so called ensemble tests.

6.5.1 Top quark mass constraint

The kinematic fit, `HitFit`, described in section 4.8 is used to obtain the jet-parton association as well as the four vectors of the $t\bar{t}$ system and its decay products. Both informations are needed for the calculation of $\cos\theta$: $\cos\theta$ is calculated in the rest frame of the W boson that decays into a charged lepton and a neutrino using the four vector of the b quark from the same parent top as well as the four vector of the charged lepton.

In contrast to the usage of `HitFit` in top mass analyses [85, 86], it is possible in this analysis to constrain the mass of the top quark to the measured value of about 175 GeV [11]. On the one hand this of course introduces a systematic uncertainty as described later but on the other hand it improves the resolution in $\cos\theta$ and increases the fraction of correct jet-parton associations.

Figure 6.12 compares the resolution in $\cos\theta$ and the fraction of correct permutations for the two cases: without and with the additional top quark mass constraint. The resolution improves by about 10%. The Figure also shows the increase in the fraction of correct permutations: it increases from about 54% to about 66%. A permutation is considered correct, if the b-quark from the semi-leptonic top quark decay is correctly identified.

6.5.2 Decay angle templates

The decay angle templates for the signal and the W+jets background sample are taken from Monte Carlo, while the template for the QCD background is derived from the untagged data by reversing the tight criteria for the isolation in the muon channel and for the electron likelihood in the electron channel, and by applying the tag rate function as described in section 6.2.1 on page 81.

The seven different signal templates have partially a sizable statistical uncertainty. To reduce this uncertainty the seven templates are interpolated to create just two templates: a template with pure $V-A$ interaction and a template with pure $V+A$ interaction. This is possible because the interference term between V-A and V+A is negligible [79]. Therefore all f_+ fractions can be reproduced by a linear combination

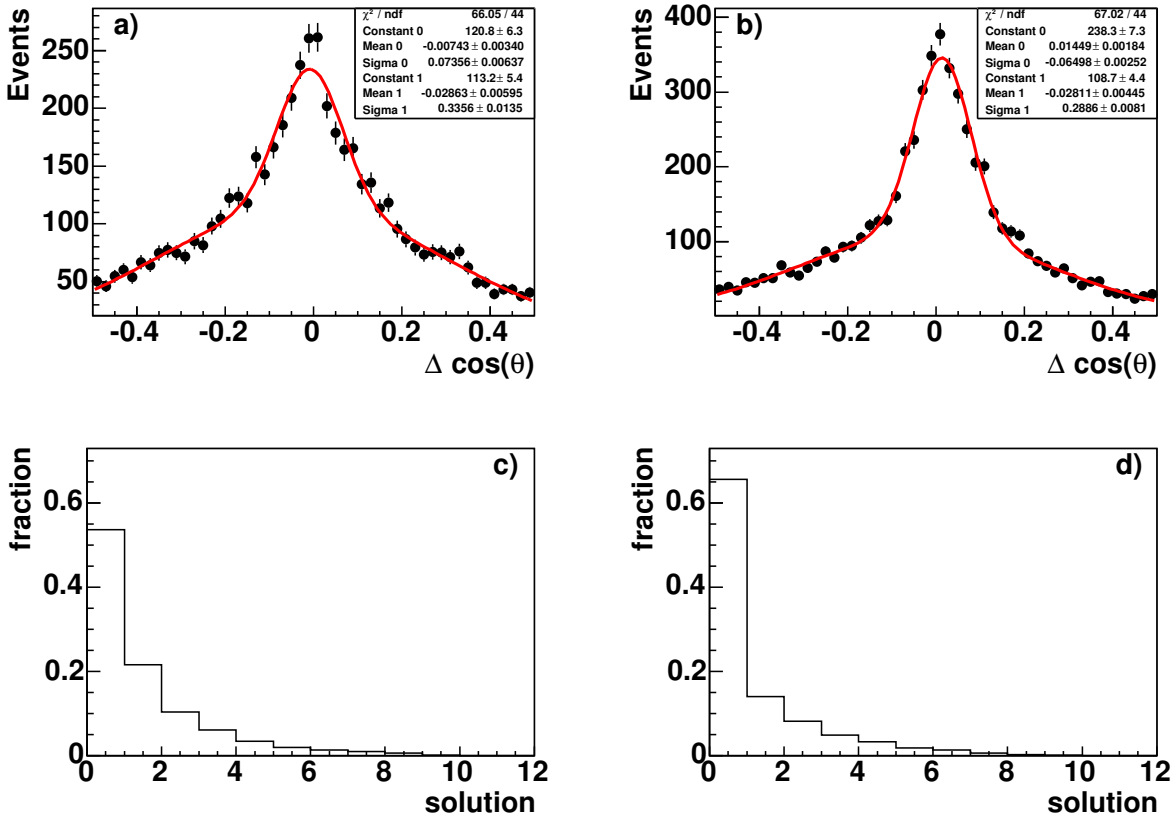

Figure 6.12: Resolution of the reconstructed decay angle without the top quark mass constraint (a) and constraining the top quark mass to be 175 GeV (b). Both distributions are fitted with a double Gaussian. With the top quark mass constraint, the resolution improves by about 10%. The bottom two plots show the fraction of correct permutations for the χ^2 ordered HitFit solutions, i.e. 0 corresponds to the minimal χ^2 solution, in case the top quark mass is unconstrained (c) and constraint to 175 GeV (d). Constraining the top quark mass significantly improves the fraction of correct permutations.

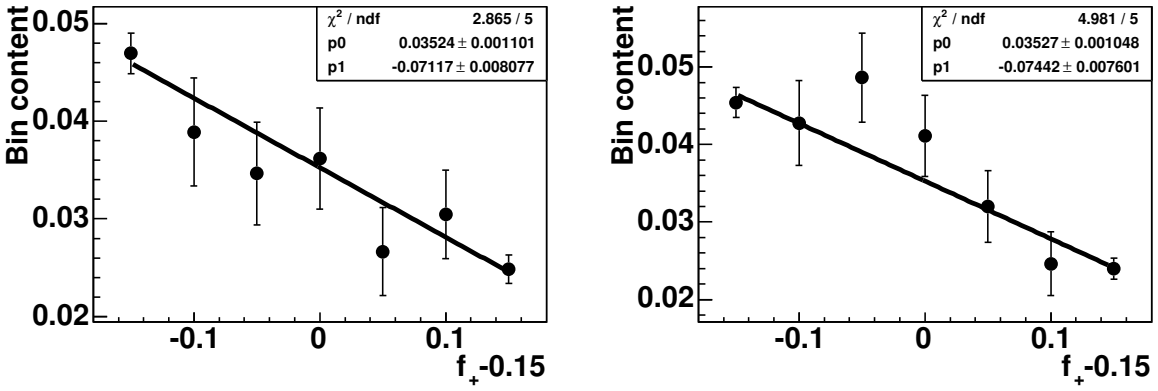

Figure 6.13: Interpolation of the signal templates in the muon channel (left) and the electron channel (right) for the $\cos\theta$ bin covering $\cos\theta \in [-1; -0.8[$. Each point corresponds to one of the seven signal Monte Carlo samples. The new templates are then constructed using the parameters and the uncertainties from the fit.

of the $V-A$ and the $V+A$ templates.

The templates are interpolated in the following way:

- for each of the seven signal samples the decay angle distribution is plotted into a histogram;
- the content of each bin i of these histograms is plotted against the corresponding V+A fraction;
- the resulting graph is fitted with a straight line;
- the templates for V-A and for V+A are created using the parameters and uncertainties from the fit.

Figure 6.13 shows the fit to the bin content for one of the bins in the decay angle template. The bin width in the $\cos\theta$ histogram is set to $\Delta\cos\theta = 0.2$ taking into account the experimental resolution for $\cos\theta$ and the number of events remaining after all cuts.

Figure 6.14 shows the signal decay angle templates for the two extreme cases, a pure $V-A$ (i.e. $f_+ = 0.00$) and a pure $V+A$ (i.e. $f_+ = 0.30$) interaction. For comparison both the parton level and the detector level are shown after the full event selection. In addition also the templates for the most important background, W+jets, and for QCD are shown.

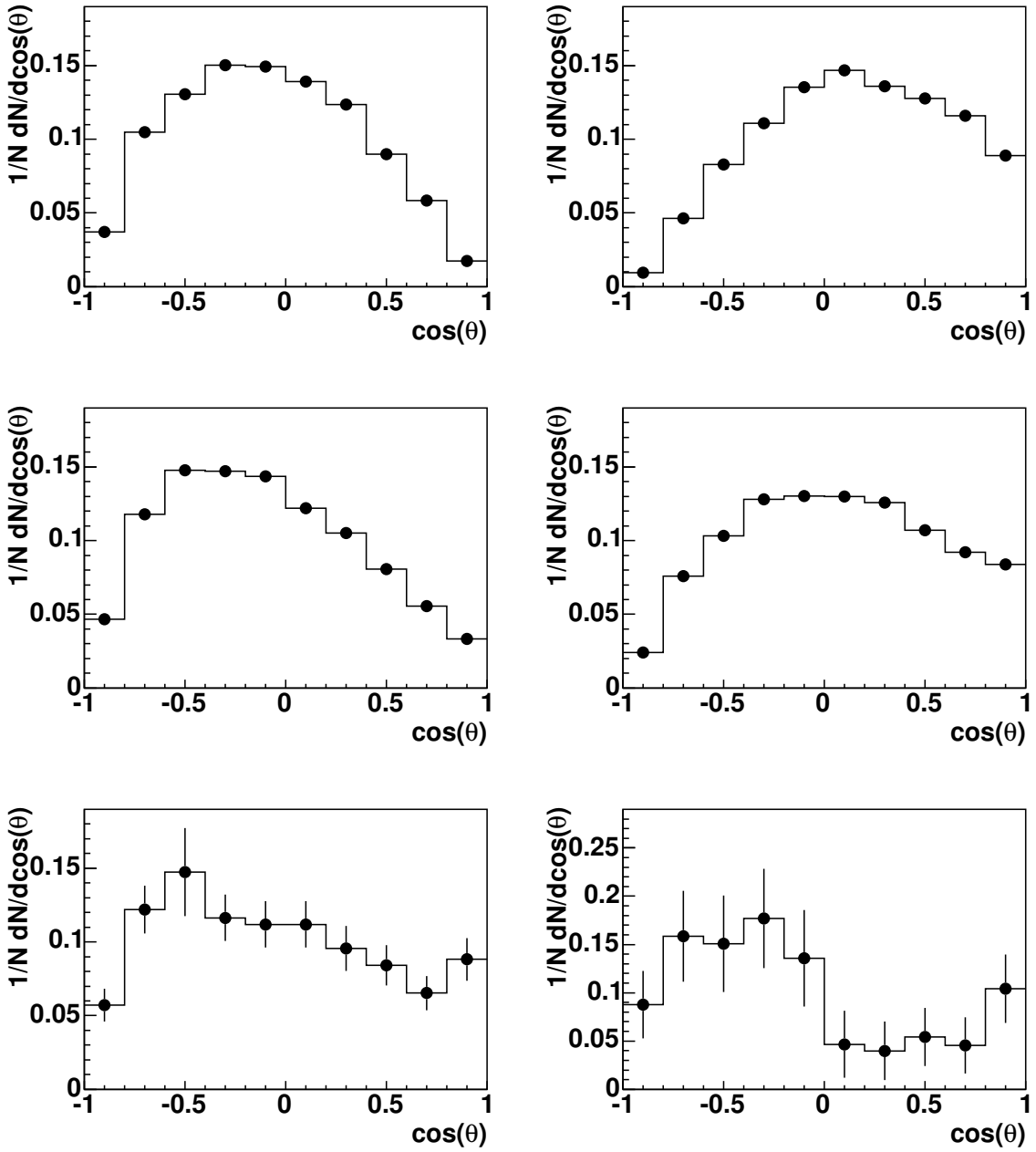

Figure 6.14: Templates of the decay angle in the electron channel after all selection cuts: $t\bar{t}$ at parton level with $f_+ = 0.0$ (top left), $t\bar{t}$ at parton level with $f_+ = 0.3$ (top right),$t\bar{t}$ at detector level with $f_+ = 0.0$ (middle left), $t\bar{t}$ at detector level with $f_+ = 0.3$ (middle right), W+jets background (bottom left) and QCD background (bottom right). The statistical precision on the signal templates is very good but the background templates have a sizable statistical uncertainty. The corresponding templates for the muon channel are very similar and are therefore not shown.

6.5.3 Extraction of f_+

A binned maximum likelihood fit is used to extract the value of f_+ using the decay angle templates for the interpolated signal templates and the various background templates. The likelihood is constructed by multiplying the Poisson probabilities of each template bin:

$$\mathcal{L}(f_+) = \prod_{i=1}^{N_{bins}} (\mu_i(f_+) + b_i)^{n_i} \cdot \frac{\exp[-(\mu_i(f_+) + b_i)]}{n_i!} \,, \tag{6.15}$$

where n_i is the number of data events in the ith data bin, b_i is the predicted background contribution and $\mu_i(f_+)$ is the predicted signal contribution given the f_+ value.

For each value of f_+ the negative logarithm of the likelihood is calculated. The resulting distribution of $-\ln\mathcal{L}$ points versus f_+ is fitted with a parabola to get the likelihood as a function of f_+. Due to the interpolation of the signal templates these $-\ln\mathcal{L}$ are correlated.

6.5.4 Ensemble tests

In order to study the properties of this analysis, so called ensemble tests are performed. In these tests, the data sample is replaced by Monte Carlo events forming mock data samples. These mock data samples are created using the following method:

- Each physics process ($t\bar{t}$, W+jets, ...) is described by a Poisson distribution where the average is fixed to the expected amount of events for this process after the full selection as given in Table 6.6 on page 95. However, as most of the these tests are made to study systematic biases or problems, the overall normalization is scaled up by a factor of 100 to reduce the statistical uncertainties in these ensemble tests.

- The $\cos\theta$ histogram of this mock data sample is then built by generating random numbers that follow the shape of the decay angle templates of the individual processes. Here the value of f_+ can be set to the desired value by interpolating the signal templates accordingly.

This method of creating the mock data samples has the advantage over the normal method, where real simulated Monte Carlo events are randomly picked to create the mock data sample, that the generation of the random numbers is faster than reading existing events. In addition the only limiting factor here is the precision of the decay angle templates, which in case of the signal templates could be improved by the interpolation procedure.

The analysis can now be studied in detail by creating a large number of these mock data sets and analyzing them. One important cross check is of course to verify that the chosen method for the extraction of f_+ really works. Figure 6.15a shows the reconstructed f_+ value versus the input f_+ value: a fit to the data points shows a nice linearity with a slope close to one.

Expected performance

To get an impartial view of the true performance of this analysis, ensemble tests have been performed assuming the standard model prediction of $f_+ = 0$ and using the actual normalization as obtained in data.

Figure 6.15b shows the difference between the measured f_+ value and the true f_+ value in a large number of ensemble tests. The RMS of this distribution is a measure of the expected statistical uncertainty of the measurement: $\Delta f_+ \approx 0.16$.

6.6 Systematic uncertainties

Systematic uncertainties can affect the analysis in two ways: the normalization can be affected and also the shape of the decay angle templates. To evaluate the magnitude of the various systematic uncertainties, ensemble tests as described in the previous section, are used.

The ensembles are build in the following way: first the templates for the likelihood discriminant are rederived for the given systematic effect, e.g. the jet energy scale variation, and the fit is redone. This provides the changed normalization of the ensembles. The change in shape is then taken into account by generating random numbers that follow the distorted decay angle distributions for the given systematic. The analysis itself is not changed, i.e. the decay angle templates used to analyze the mock data sets are the nominal decay angle templates.

Tables 6.7 and 6.8 list the magnitude of the change in the normalization for the two dominant systematic uncertainties.

The following sources of systematic uncertainties have been studied:

Uncertainty associated to the top quark mass The mass of the top quark enters into the kinematic fit as a constraint ($m_{top} = 175$ GeV). In addition a different top quark mass also changes the distribution of kinematic variables which are used in the event selection.

To study the systematics due to the uncertainty on the top quark mass, signal templates with $m_{\text{top}} = 170$ GeV and $m_{\text{top}} = 180$ GeV, respectively, have been

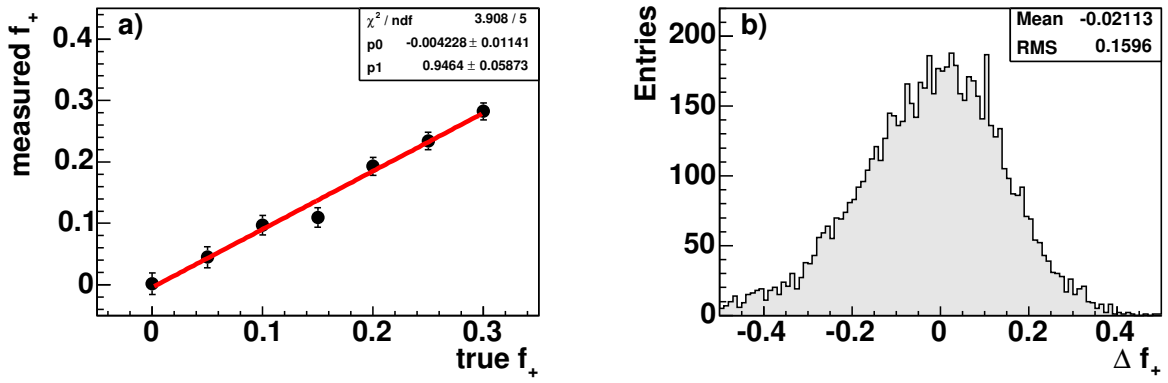

Figure 6.15: a) Measured f_+ values as a function of the input f_+ value. For each point ensembles from the corresponding signal and background samples have been created and the average measured f_+ is plotted. The error bars correspond to the RMS of the measured f_+ distribution. In these tests the statistics is increased by a factor of 100 in order to be less sensitive to statistical fluctuations in the individual ensembles. b) Difference between the measured and the true f_+ value obtained from ensemble tests. The RMS of the distribution corresponds to the expected statistical uncertainty of this measurement.

Channel	$m_{top} = 170$ GeV			$m_{top} = 180$ GeV		
	$t\bar{t}$	W+jets	QCD	$t\bar{t}$	W+jets	QCD
μ+jets	17.2 ± 4.9	3.5 ± 2.1	0.2 ± 0.2	16.7 ± 4.8	4.0 ± 2.1	0.2 ± 0.2
e+jets	24.5 ± 6.6	7.2 ± 3.6	1.3 ± 0.5	22.5 ± 6.4	8.6 ± 3.5	1.3 ± 0.5

Table 6.7: Predicted number of events obtained by varying the top quark mass by ± 5 GeV around the nominal top quark.

Channel	JES -1σ			JES $+1\sigma$		
	$t\bar{t}$	W+jets	QCD	$t\bar{t}$	W+jets	QCD
μ+jets	16.5 ± 4.9	3.8 ± 2.2	0.2 ± 0.1	14.6 ± 4.7	6.1 ± 2.7	0.2 ± 0.2
e+jets	26.3 ± 6.7	5.8 ± 3.3	1.3 ± 0.5	19.0 ± 6.3	11.8 ± 4.1	1.3 ± 0.5

Table 6.8: Predicted number of events obtained by varying the JES by $\pm 1\sigma$.

used.

Uncertainty associated to the JES A difference in the jet energy scale leads to a change in the normalization of the samples as well as a change in the shape of the decay angle distribution. To estimate this uncertainty, the jet energy scale has been varied by one standard deviation around the nominal correction, where, conservatively,

$$\Delta = \sqrt{\Delta^2_{stat,data} + \Delta^2_{syst,data} + \Delta^2_{stat,MC} + \Delta^2_{syst,MC}}. \tag{6.16}$$

The individual terms are the statistical and systematic uncertainties on the JES in data and in Monte Carlo. This variation was used everywhere except for the kinematic fit where additional jet corrections are applied which improve the JES resolution. The resulting relative uncertainty on the JES is therefore only 0.05 for jets with $p_T \geq 30$ GeV and $0.3 - \frac{p_T}{120\text{GeV}}$ for jets with $p_T < 30$ GeV [59].

Uncertainty associated to the limited template statistics The decay angle templates used in this analysis for signal and background have a statistical uncertainty due to the finite Monte Carlo statistics or, in case of the multijet background, due to the finite data statistics. The uncertainty on the signal templates is negligible due to the interpolation technique that is used. However, the background templates have a sizable statistical uncertainty despite the large data sets used.

Uncertainty associated with the fit to the likelihood discriminant The uncertainties on the number of signal, W+jets and QCD events from the fit are treated as systematic uncertainties. The anti-correlation between the number of W+jets and signal events has been taken into account by assuming that these numbers are totally anti-correlated, i.e. if the signal is scaled up the background is scaled down and vice versa.

Uncertainty associated with the *b*-tag parameterizations The parameterizations for the b-tag efficiency and the mistag rate have been varied within their uncertainties to estimate the systematic uncertainty due to these parameterization. In addition also the parameterization for the taggability has been varied within its uncertainty.

Uncertainty associated with the calibration of the method The average measured f_+ value does not perfectly match the input f_+ value. The average deviation between the input and the output f_+ value is taken as systematic uncertainty.

Uncertainty associated with the flavor composition of the W+jets background The exact flavor composition of the W+jets background is not known and can only be estimated using the relative theoretical cross section, the jet-parton matching and the parameterized b-tagging efficiency. To get a handle on the size of this

effect, the predicted W+jets flavor composition has been replaced by events with only light quarks and by events with two b-quarks.

Uncertainty associated with the modeling of the W+jets background The nominal W+jets background samples have been generated using the following parameterization for the factorization and renormalization scale Q: $Q^2 = m_W^2 + \sum m_T^2$, where m_T is the transverse mass defined as $m_T^2 = m^2 + p_T^2$ and the sum $\sum m_T^2$ extends to all final state partons (including the heavy quarks but excluding the W boson decay products). This scale Q has been changed to $Q^2 = \langle p_T \rangle^2$.

As only the light flavor sample is available with this different scale the following procedure is used: all W+jets samples are replaced by the light flavor sample and the resulting systematic uncertainty is corrected for the incorrect flavor composition by assuming that the systematic uncertainty due to the scale Q is uncorrelated with the systematic uncertainty on the flavor composition.

Uncertainty associated with the modeling of the $t\bar{t}$ signal The signal Monte Carlo used in the measurement includes only the $t\bar{t}$ leading order matrix element and the radiation of additional jets is modeled by PYTHIA. To study the effect of extra jets, a separate sample including the extra radiation in the leading order matrix element has been generated. This sample is mixed with the original sample for $f_+ = 0$ according to the relative cross section of the processes, 6 pb for $t\bar{t}$ and 2.5 pb for $t\bar{t} + j$, to study this effect.

After taking into account the differences in the selection efficiency, the following relative fraction for the $t\bar{t} + j$ sample has been found: 33.7% in the muon channel and 34.7% in the electron channel.

The average observed shift in the ensemble tests using different values of f_+, i.e. the square root of the quadratically added differences, is taken as corresponding systematic uncertainty. The individual systematic uncertainties are then added in quadrature to obtain the overall systematic uncertainty. Table 6.9 lists the individual contributions as well as the overall systematic uncertainty.

Source	Uncertainty
Jet energy scale	0.040
Top quark mass	0.038
Limited template statistics	0.021
Likelihood Fit (electron channel)	0.015
Likelihood Fit (muon channel)	0.008
Composition of W+jets background	0.015
W+jets model	0.011
$t\bar{t}$ model	0.021
Analysis method (calibration)	0.008
b-tag parameterizations	0.001
Total	0.069

Table 6.9: Average observed shift of f_+ in the ensemble tests for each of the systematic effects studied. The total systematic uncertainty is obtained by adding the individual uncertainties in quadrature.

7 Results

After the full event selection 19 events are selected in the muon channel and 33 in the electron channel with an expected signal to background ratio of 3.7 in the muon and 2.4 in the electron channel. The decay angle distribution of these events as well as the calculated negative log likelihood curve for the combination of both channels is shown in Figure 7.1. The individual negative log likelihood values are listed in Table 7.1.

The $\cos\theta$ distributions show a deficit of data events at small positive values of $\cos\theta$. However, no systematic effect could be identified that produces such a deficit in this region. Furthermore it is compatible with being a statistical fluctuation in the data. Any further investigation of this deficit needs therefore more data which will be available in the coming years. The result on f_+ is not influenced by this effect as this particular region in $\cos\theta$ is insensitive to a change in f_+ as can be seen from Figure 7.1c.

The extracted value of f_+ from the fit to the negative log likelihood points together with the estimated systematic uncertainty yields the following result [87, 88]:

$$f_+ = -\mathbf{0.10} \pm \mathbf{0.17}\,(\boldsymbol{stat}) \pm \mathbf{0.07}\,(\boldsymbol{syst}), \tag{7.1}$$

which to date is the most precise single measurement of f_+ using DØ data. The central value is outside the physically allowed region of $f_+ = 0.00 - 0.30$ but consistent with the standard model prediction of $f_+ = 0.00$. The observed statistical uncertainty of 0.17 is also in good agreement with the expected statistical uncertainty of 0.16.

7.1 Limit calculation

Both limit setting methods, the frequentist and the Bayesian approach, described in section 2.4 have been used to obtain an upper limit on f_+. The final limit quoted in this analysis will be based on the Bayesian approach, as this is the method preferred by the DØ collaboration [89]. In addition, it can easily be used to quote a combined limit from several different analyses on f_+ whereas for the frequentist method the combination of the Monte Carlo acceptance is not trivial. The final result is quoted using a 95% confidence level.

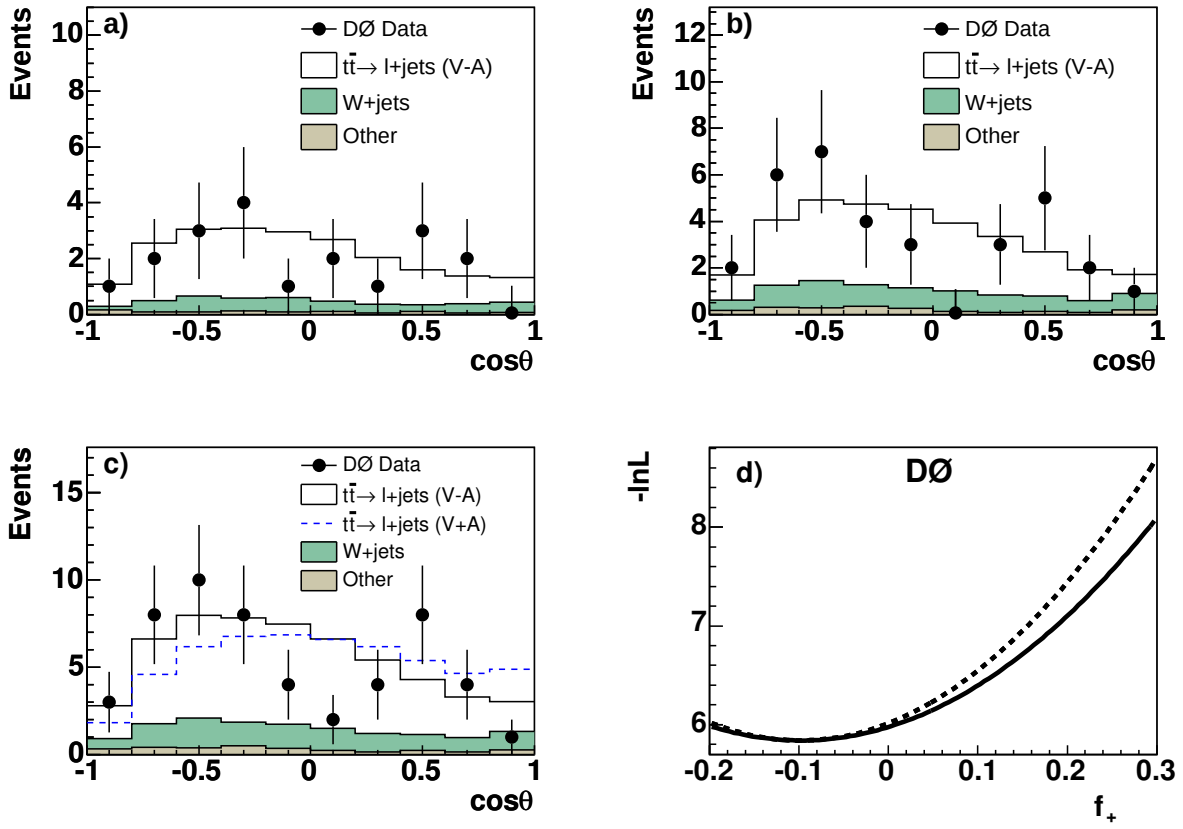

Figure 7.1: a) $\cos\theta$ distribution observed in the muon channel, b) in the electron channel, and c) in the combination of both. The prediction from the standard model, i.e. $f_+ = 0.00$ is shown as open histogram. c) shows in addition the maximal deviation from the standard model, i.e. $f_+ = 0.30$, as dashed line. d) The fit to the calculated negative log likelihood values. The dashed line contains only the statistical uncertainty and the solid line includes in addition the total systematic uncertainty.

f_+	0.00	0.05	0.10	0.15	0.20	0.25	0.30
$-\ln\mathcal{L}$	6.01	6.24	6.55	6.95	7.44	8.02	8.70

Table 7.1: The negative log likelihood values for seven different values of f_+. These values are used to fit the parabola shown in Figure 7.1 (d).

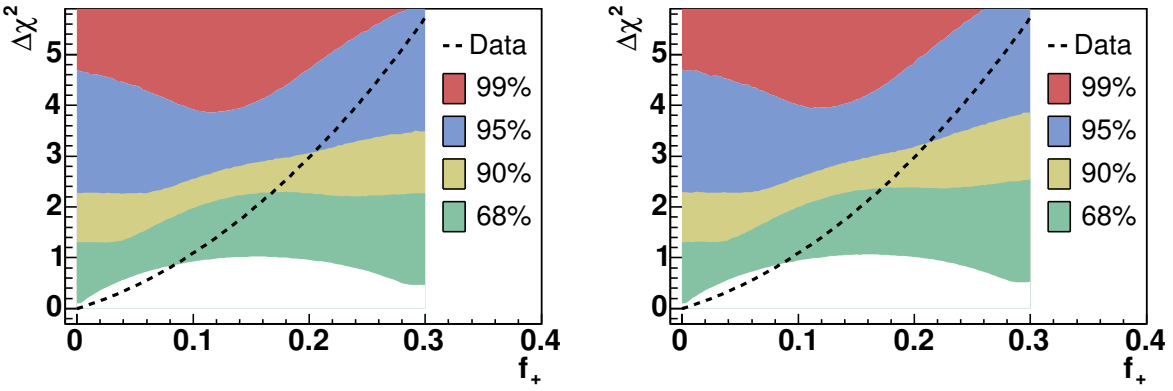

Figure 7.2: The result from the data on top of the Monte Carlo acceptance for statistical only (left) and including systematic effects (right). The data line indicates which values of f_+ are excluded at the various confidence levels: if the data point lies in a given (colored) region than this point is at least excluded at the confidence level that is assigned to this color. The acceptance is calculated from Monte Carlo experiments as described in section 2.4.1.

7.1.1 Frequentist approach

The physics boundaries on f_+ are directly built into the limit calculation procedure as described in section 2.4.1. Using this method the systematic effects can easily be included in the calculation of the Monte Carlo acceptance by replacing the mean μ in the Poisson distribution for each bin with a random number following a Gaussian with mean μ and a width corresponding to the systematic uncertainty. As the total systematic uncertainty is small compared to the statistical one, the effect of including the systematic uncertainties in the acceptance calculation is also small.

Comparing the result obtained in data with the Monte Carlo acceptance in Figure 7.2, the following limit is obtained:

$$f_+ < 0.21 \quad (95\%\ \text{C.L.}) \tag{7.2}$$

7.1.2 Bayesian approach

The physically allowed values for f_+ range from $f_+ = 0.00 - 0.30$. This is incorporated in the limit calculation by multiplying the likelihood with a prior that is zero outside and constant inside the physically allowed region:

$$\pi(f_+) \sim \begin{cases} 1 & 0 \leq f_+ \leq 0.3 \\ 0 & f_+ < 0 \text{ or } f_+ > 0.3 \end{cases} \tag{7.3}$$

The obtained limit including the systematic uncertainties is:

$$f_+ < \mathbf{0.24} \ \ \mathbf{(95\%\ C.L.)} \tag{7.4}$$

The differences in the limit between the Bayesian and the frequentist method can be explained by the fact that the observed minimum is outside the physically allowed region. In such cases the frequentist method results in lower limits than the Bayesian method.

7.2 Combination with the topological analysis

Independent of this analysis, a second analysis of the W boson helicity has been performed [90] using the same dataset and the same sensitive variable $\cos\theta$ but different selection criteria: there, the aim was to select top quark events using only topological variables in order to make use of top quark events in which no jet can be tagged as b-jet. The obtained result is: $f_+ = 0.17 \pm 0.22\,(stat) \pm 0.08\,(syst)$.

As the second analysis vetoes events which contain at least one b-tagged jet, the final data samples used by the two analyses are statistically independent. It is therefore straightforward to combine these results statistically by weighting each individual result with the corresponding statistical uncertainty:

$$f_+ = \frac{f_+^{(1)} \cdot \sigma_2^2 + f_+^{(2)} \cdot \sigma_1^2}{\sigma_1^2 + \sigma_2^2} \tag{7.5}$$

$$\sigma = \sqrt{\frac{\sigma_1^2 \cdot \sigma_2^2}{\sigma_1^2 + \sigma_2^2}} \tag{7.6}$$

where $f_+^{(i)}$ are the central values and σ_i the corresponding statistical uncertainties of the two analyses, and f_+ and σ are the combined central value and statistical uncertainty.

Systematic uncertainties are combined using error propagation on f_+. The combined uncertainty $\delta f_{+,j}$ for each source of systematic uncertainty j is given by:

$$\begin{aligned}(\delta f_{+,j})^2 &= \left(\frac{\partial f_+}{\partial f_+^{(1)}}\right)^2 \delta_{j,1}^2 + \left(\frac{\partial f_+}{\partial f_+^{(2)}}\right)^2 \delta_{j,2}^2 + 2C_j \left(\frac{\partial f_+}{\partial f_+^{(1)}}\right)\left(\frac{\partial f_+}{\partial f_+^{(2)}}\right)\delta_{j,1}\delta_{j,2} \\ &= \sigma^4 \left(\frac{\delta_{j,1}^2}{\sigma_1^4} + \frac{\delta_{j,2}^2}{\sigma_2^4} + \frac{2C_j\delta_{j,1}\delta_{j,2}}{\sigma_1^2\sigma_2^2}\right)\end{aligned} \tag{7.7}$$

Source	Analysis 1	Analysis 2	Correlation	Combined
Jet energy scale	0.04	0.03	100%	0.04
Top quark mass	0.04	0.04	100%	0.04
Template statistics	0.02	0.05	50%	0.03
b-tag	0.02	0.03	100%	0.02
$t\bar{t}$ model	0.02	0.01	100%	0.02
W+jets model	0.01	0.01	100%	0.01
Sample composition	0.02	—	0%	0.01
Calibration	0.01	0.01	0%	0.01
Total	0.07	0.08		0.07

Table 7.2: Systematic uncertainties on f_+ of the two different analyses together with their correlation and the combined uncertainty. The large difference in the systematic uncertainty due to the template statistics can be explained by the fact that the background contribution in analysis 2 is much larger than in analysis 1.

Most of the systematic uncertainties are treated as fully correlated between both analyses, e.g. the uncertainty on the top quark mass or the jet energy scale. Since the analyses themselves and also the final data samples are independent, the uncertainty on the final sample composition as well as the uncertainty due to the chosen analysis method, i.e. the calibration of the analysis, are treated as uncorrelated. The uncertainty on the final sample composition appears only in the analysis presented in this thesis as the other analysis includes this uncertainty in their statistical uncertainty.

The remaining systematic uncertainty is treated as partially correlated. Even though both analyses have an independent sample selection in the data this is not true for Monte Carlo: the b-tagging is implemented via parameterizations that just assign a weight to the events but all the events remain in the sample. This means that the same Monte Carlo event can contribute to both analyses and therefore an arbitrary value of 0.5 (corresponding to the overall b-tag efficiency) is assigned to the correlation coefficient of this source. It has been verified that a different value of this correlation coefficient ($\pm 50\%$) does not change the overall systematic uncertainty.

Table 7.2 lists the inputs to the combination procedure for the systematic uncertainties as well as its results. The combined result on f_+ including all uncertainties is [87, 91]:

$$f_+ = \mathbf{0.00 \pm 0.13\,(stat) \pm 0.07\,(syst)}. \tag{7.8}$$

The Bayesian limit calculation procedure is performed by convoluting the combined likelihood with a Gaussian whose width corresponds to the total combined systematic

uncertainty. The resulting limit is:

$$f_+ < \mathbf{0.25} \ \ \mathbf{(95\% \ C.L.)} \tag{7.9}$$

The limit did not change when combining the two analyses compared to the analysis from this thesis alone. This can be explained by the fact that the central values for f_+ are at different sides of the physically allowed region but, within their statistical uncertainty, still compatible with each other.

This combined result represents the first measurement of the fraction of right-handed W bosons from the DØ experiment and the first published result [87] on the W boson helicity using data from RunII of the Tevatron Collider.

7.3 Outlook

Values of f_+ above 0.01 cannot be explained in the Standard Model. In the next couple of years the analyses will not be able to reach this precision for f_+ but the physically allowed region will be further restricted. In this section possible improvements of the measurement of the W boson helicity in future analyses will be pointed out. The most important steps are to increase the statistics of the data set and to use a detector with an increased performance, e.g. a better signal to background separation and a better calibration. In addition, other analysis methods can be exploited in the measurement of f_+.

7.3.1 Tevatron and DØ

The current analysis is limited by statistics. Therefore the obvious way to improve the analysis is to use more data once it is available. DØ has already collected more than 0.5 fb^{-1} and is still collecting data until the year 2009. By this year, an integrated luminosity of about $5 - 10$ fb^{-1} might be available.

The expected statistical uncertainty achievable by this analysis at the end of the data taking in the year 2009 is $\sigma_{stat}(f_+) \approx 0.03$. At this point the current systematic uncertainty on f_+ would dominate the total uncertainty. However, also the systematic uncertainties will decrease with more data and a better understanding of the detector:

- The uncertainty on the top quark mass will improve by about a factor of two.
- The uncertainty on the jet energy scale will decrease with a better understanding of the detector and more calibration data. Efforts are already underway to measure the JES within top quark decays by using the W boson decaying into a quark-antiquark pair.

- Systematic uncertainties due to limited Monte Carlo statistics can be reduced by generating much larger samples. As the performance of the computers is increasing with time this will not be a problem by 2009.

- The understanding of the $t\bar{t}$ model will also improve with an increased dataset so that this uncertainty will be reduced.

- The increase in the instantaneous luminosity, which leads to a higher background from minimum bias interactions, and the effects of radiation damage in the detector will degrade the performance of the analysis. However, these effects can be compensated by the planed upgrade of the silicon tracker and the trigger system.

- A larger dataset will decrease the relative uncertainty on the sample composition by the same factor as the statistical uncertainty.

Overall the total systematic uncertainty can be reduced to the same level as the statistical uncertainty: $\sigma_{syst}(f_+) \approx 0.03$.

7.3.2 LHC and the ATLAS detector

Recently a study [92] has been performed to estimate the achievable precision on f_+ at the LHC. This study uses the ATLAS[1] detector and an integrated luminosity of 10 fb^{-1}, corresponding to one year of data taking at low luminosity (10^{33} cm^{-2}s^{-1}). As the cross section for $t\bar{t}$ production is much higher at the LHC energy of $\sqrt{s} = 14$ TeV, $\sigma_{t\bar{t}} \approx 850$ pb [93], the number of available $t\bar{t}$ events is more than a factor 200 higher than at the Tevatron which as a result renders the statistical uncertainty negligible: $\sigma_{stat}(f_+) \approx 0.003$.

The study uses the same discriminating variable, $\cos\theta$, as the analysis in this thesis. The differences are that the estimated signal to background ratio will be increased to around 12 by using only double tagged events. This has the advantage that the combinatorial background on the correct jet permutation is reduced. The other difference is that with such a large dataset it is possible to measure f_+ and f_0 simultaneously.

The sources of systematic uncertainties at the LHC are very similar to the ones at the Tevatron. However, the expected strength of these uncertainties is estimated to be much smaller than at the Tevatron[2]. The expected overall systematic uncertainty is: $\sigma_{syst}(f_+) \approx 0.013$.

[1] A Toroidal LHC ApparatuS

[2] It remains to be seen if these estimations based only on a fast simulation of the ATLAS detector reflect the true uncertainties found once the real data from the detector is available.

The LHC will therefore be able to test the whole parameter space for f_+ that cannot be explained in the standard model, i.e. $f_+ > 0.01$ [26].

7.3.3 Other analysis methods

A possible $V + A$ contribution in the decay of the top quark cannot only be measured by comparing the $\cos\theta$ distribution in data with the expectations but also by using other variables and techniques.

Lepton p_T

The easiest way to measure the helicity of the W boson is to analyze the lepton p_T spectrum. This method was used in the first measurement by CDF [94]. The charged leptons from decays of right handed W bosons have a harder p_T spectrum compared to the ones from left-handed and longitudinal polarized W bosons due to the preferred emission of the leptons in the flight direction of the decaying W boson. Essentially this is nothing more than the effect of the different $\cos\theta$ shape observed in the lab frame. As the information on the flight direction of the W boson is not used in this method, the analyzing power is reduced compared to the direct reconstruction of $\cos\theta$. In addition this method is sensitive to the p_T distribution of the top quarks which leads to additional systematic uncertainties. However, this method has the advantage that it can be applied to $t\bar{t}$ events in the dilepton channel and therefore in an independent dataset. Another advantage is that the method does not rely on jets for the actual measurement and therefore the sensitivity to the jet energy scale uncertainty is reduced.

Matrix Element method

Another interesting and very powerful approach is the Matrix Element method. This method has been originally developed to measure the top quark mass [95] and has later been adopted for the measurement of f_0 [96].

The basic idea behind this method is to make use of the full information in the event by using the matrix element $\mathcal{M}$ for $t\bar{t}$ production and decay: the matrix element is written down as a function of f_+ (or any other variable that should be measured). By measuring the final state particles in each event the probability density versus f_+ can be calculated. This event-by-event procedure ensures that each event is weighted differently depending on how well it is measured. In addition, by calculating the matrix element for the background, it is possible to create for each event a background probability that can be used to further reduce the background contamination in the final sample.

The disadvantage of this method is that it is very time consuming: the calculation of the matrix elements can take up to several minutes per event, depending on the desired precision. As only the leading order matrix element is used in these calculations the effects from higher orders need to be carefully estimated for the systematic uncertainties.

7.4 Measurements of the W boson helicity

The analysis presented here is the first published result [87] on f_+ using data from RunII of the Tevatron and the only measurement of f_+ from DØ. However, there are also other measurements on the helicity of the W boson, performed using RunI data, and also indirect limits on f_+ from $b \to s\gamma$ analyses. In the following the results from those measurements are briefly summarized.

Other direct measurements of f_+

The only other direct measurement of f_+ has been recently published by CDF [97] using data from RunI. There, a similar approach as in this analysis has been used. The difference is that instead of reconstructing the rest frame of the W boson, an approximation of $\cos\theta$ is used:

$$\cos\theta \approx \frac{2m^2_{\ell b}}{m_t^2 - M_W^2} - 1 \tag{7.10}$$

This leads to a degraded separation power in $\cos\theta$. On the other hand the advantage of this method is that the event does not need to be reconstructed and specifically no information about the neutrino is needed. This yields a slightly lower systematic uncertainty on the final result. In addition, the lepton p_T spectrum is analyzed to regain sensitivity. By using this method, the dilepton events can be included, which reduces the statistical uncertainty. Combining these two methods and the two data samples, the following result is obtained:

$$f_+ = -0.02 \pm 0.11 \quad \Longrightarrow \quad f_+ < 0.18 \,@\, 95\ \%\text{CL}. \tag{7.11}$$

Direct measurements of f_0

Both experiments, CDF and DØ, performed measurements of f_0 using data from RunI. CDF used the lepton p_T spectrum to extract the value of f_0 assuming the standard model prediction for f_+. Their result based on the dilepton sample is [94]:

$$f_0 = 0.91 \pm 0.37\,(stat) \pm 0.13\,(syst)\ . \tag{7.12}$$

Inspired by the new measurement of the top quark mass using the matrix element approach, an analysis of f_0 has been performed at DØ with this method [96] and assuming the standard model prediction for f_+. Using this improved analysis technique, the to date smallest uncertainty on f_0 could be achieved:

$$f_0 = 0.56 \pm 0.31 \; . \tag{7.13}$$

Indirect limits on f_+

A possible $V + A$ contribution in the top quark sector can also influence the b quark sector through an electroweak penguin contribution. Under the assumption that this penguin contribution is dominant, an upper limit on f_+ of a few percent can be set [98, 99] using the measured branching ratio for $b \to s\gamma$ [100].

8 Summary

In this thesis a measurement of the fraction of W bosons with positive helicity in $t\bar{t}$ events recorded by the DØ detector during the years 2002-2004 has been presented. The data corresponds to an integrated luminosity of about 230 pb^{-1}. The measurement makes use of the decay angle θ between the charged lepton and the (negative) b quark direction in the rest frame of the W boson. To obtain the angle θ, the $t\bar{t}$ system and its decay products have been reconstructed using a kinematic fit with constraints on the mass of the W boson and of the top quark. By constraining the top quark mass, the resolution in $\cos\theta$ could be improved by about 10%.

The event selection makes use of b quark identification by requiring the presence of a significantly displaced secondary vertex. This reduces the background contribution significantly and the signal to background ratio is improved to about 1. In addition an optimized discriminant combining four variables that show a difference between $t\bar{t}$ and background events allowed for the measurement of the data sample composition and a further background reduction. The in situ measurement of the sample composition in the data ensures a good description of the background rate. After all cuts the ratio between signal and background events could be increased to 3.7 in the muon and 2.4 in the electron channel.

By comparing the expectation for $\cos\theta$ from Monte Carlo samples with different fractions of right-handed W bosons, f_+, with the distribution obtained in data, the following result for f_+ has been obtained:

$$f_+ = -0.10 \pm 0.17\,(stat) \pm 0.07\,(syst).$$

Even though the central value is outside the physically allowed region for f_+, ranging from 0.0 to 0.3, it is, within the uncertainty, compatible with the theoretical prediction at next to leading order: $f_+ = 3.6 \times 10^{-4}$. Using a Bayesian limit setting approach, an upper limit on the fraction of right-handed W bosons could be set:

$$f_+ < 0.24 \;\; (95\% \;\; \text{C.L.})$$

This effectively rules out theoretical models which predict a pure or very high $V + A$ contribution in the weak charged current interaction of the top quark. Together with a similar analysis using only events where no b-jets could be identified, this result has been published in Physical Review D [87].

The currently limiting factor in the measurement of the W helicity is the amount of available data. At the end of the Tevatron run in 2009 the available data sample will be a factor of $20 - 30$ larger than the one used in this analysis. At this stage the statistical and the systematical uncertainty will be similar to each other. Extrapolating the current analysis, a precision of $\Delta f_+ \approx 0.05$ should be reachable.

The LHC will allow for a significantly lower uncertainty on f_+. There the statistical uncertainty will be negligible due to the millions of $t\bar{t}$ pairs produced every year. The improvement in the detector performance and the understanding of the top quark will reduce the systematic uncertainty so that the expected precision after one year of data taking will be: $\Delta f_+ \approx 0.01$.

A Supplementary information on the analysis

A.1 Templates

For completeness Fig. A.1 shows the decay angle templates in the muon channel and Fig. A.2 the templates for the discriminant $\mathcal{D}$ that have not been shown in the main part of the thesis as they are very similar between the lepton channels.

Figure A.3 shows the distortion in the decay angle templates caused by the variation of the jet energy scale and Figure A.4 the distortion caused by the variation of the top quark mass.

A.2 Additional control plots

As a sanity check, the following additional control plots are shown:

- Figures A.5–A.10 show a comparison between data and Monte Carlo after applying all selection cuts. There is a good agreement between data and the prediction from Monte Carlo simulations.

- Figures A.11 and A.12 show a comparison between the tagged QCD events in the second jet multiplicity bin with the predictions from the inclusive tag rate function. The good agreement between the predicted and the observed shape gives confidence that the prediction will also be in good agreement for the inclusive 4th jet multiplicity bin.

- Figure A.13 compares the result obtained by the fit to the likelihood discriminant to the theoretical prediction for $t\bar{t}$ production and the results obtained by the corresponding cross section measurement [69]. The results are in reasonable agreement.

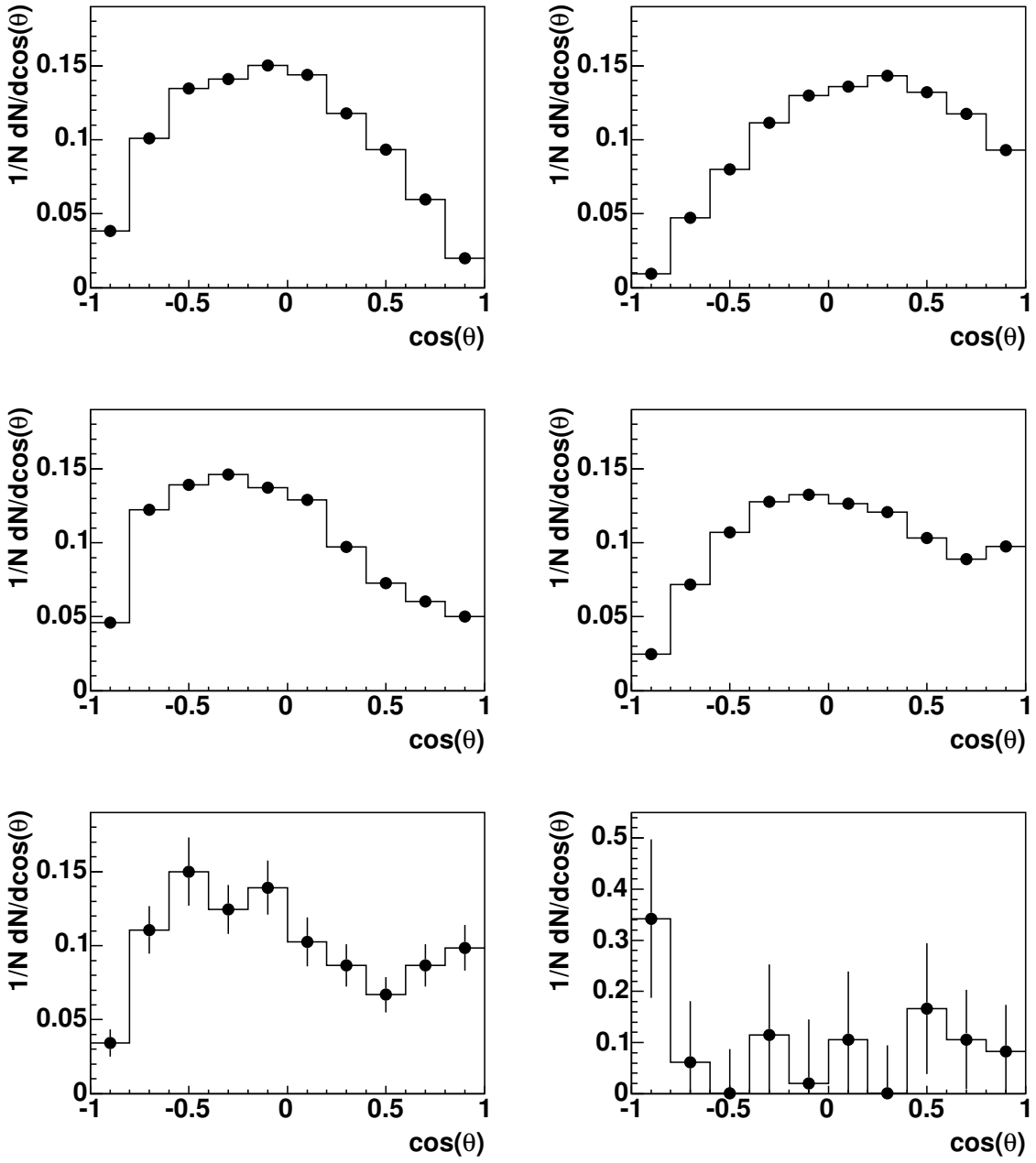

Figure A.1: Templates of the decay angle in the muon channel after all selection cuts: $t\bar{t}$ at parton level with $f_+ = 0.0$ (top left), $t\bar{t}$ at parton level with $f_+ = 0.3$ (top right),$t\bar{t}$ at detector level with $f_+ = 0.0$ (middle left), $t\bar{t}$ at detector level with $f_+ = 0.3$ (middle right), W+jets background (bottom left) and QCD background (bottom right). The statistical precision on the signal templates is very good but the background templates have a sizable statistical uncertainty. The corresponding templates for the electron channel are shown on page 100.

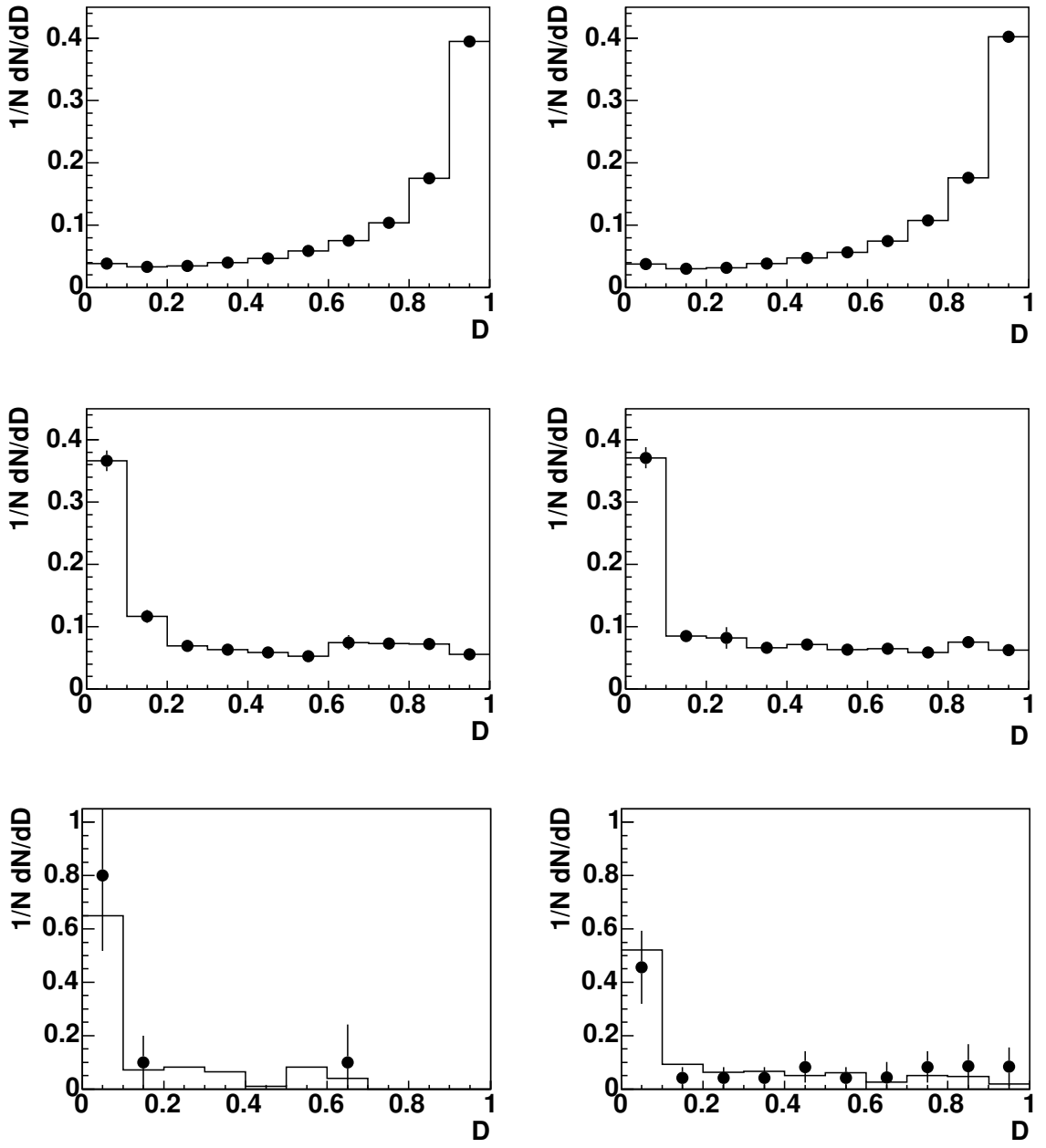

Figure A.2: Templates of the likelihood discriminant D for the muon channel (left) and the electron channel (right). The distributions on the top refer to $t\bar{t}$ and the ones in the middle to W+jets. On the bottom the likelihood discriminant for QCD events is shown. The histograms correspond to the reweighted untagged QCD events. For comparison the tagged QCD events are shown as dots.

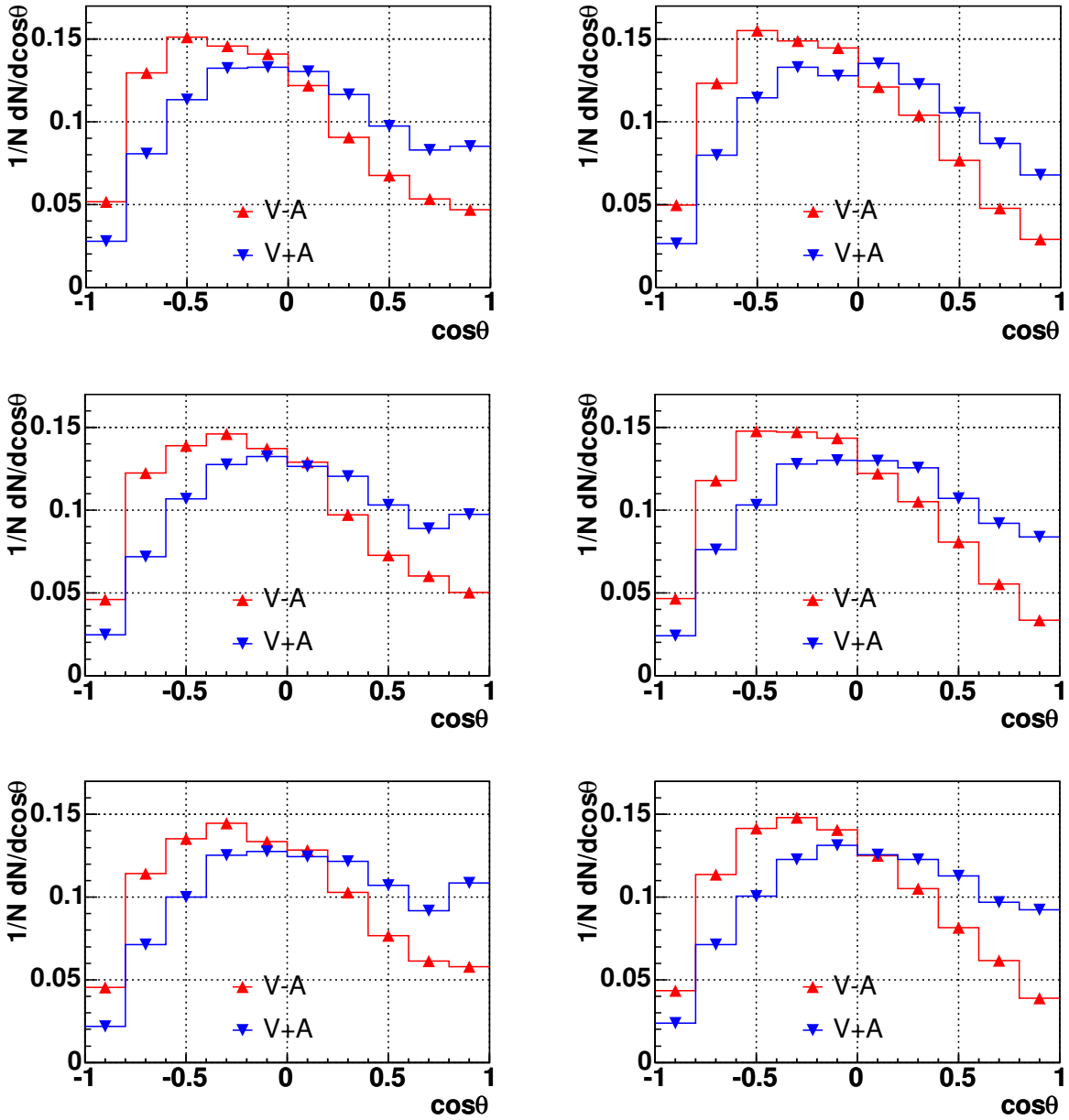

Figure A.3: Decay angle distribution after all selection cuts in the muon (left) and the electron channel (right) with different variations of the jet energy scale: variation of -1σ (top), no variation (middle) and a variation of $+1\sigma$ (bottom).

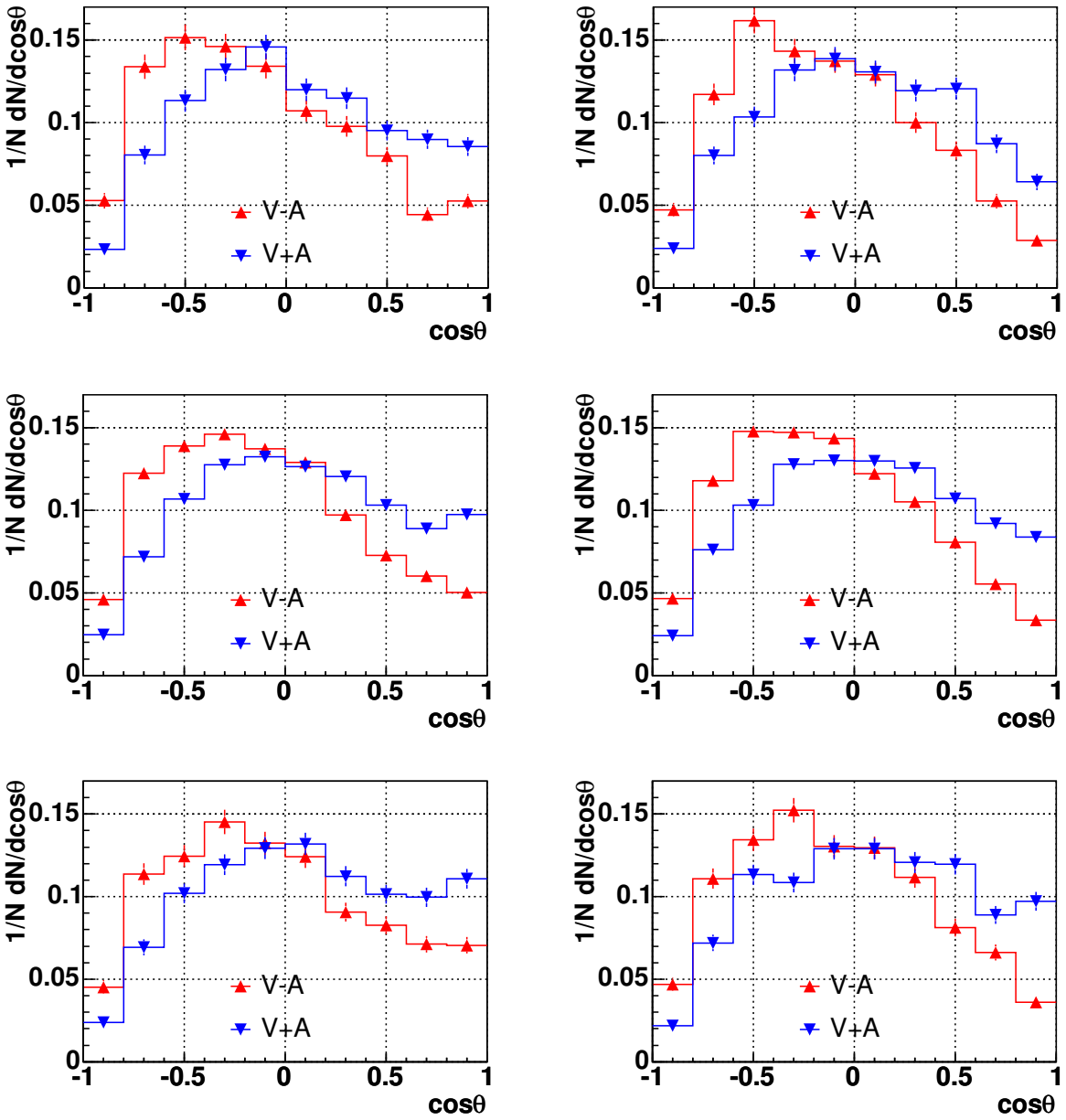

Figure A.4: Decay angle distribution after all selection cuts in the muon (left) and the electron channel (right) with different values for the top quark mass: 170 GeV (top), 175 GeV (middle) and 180 GeV (bottom).

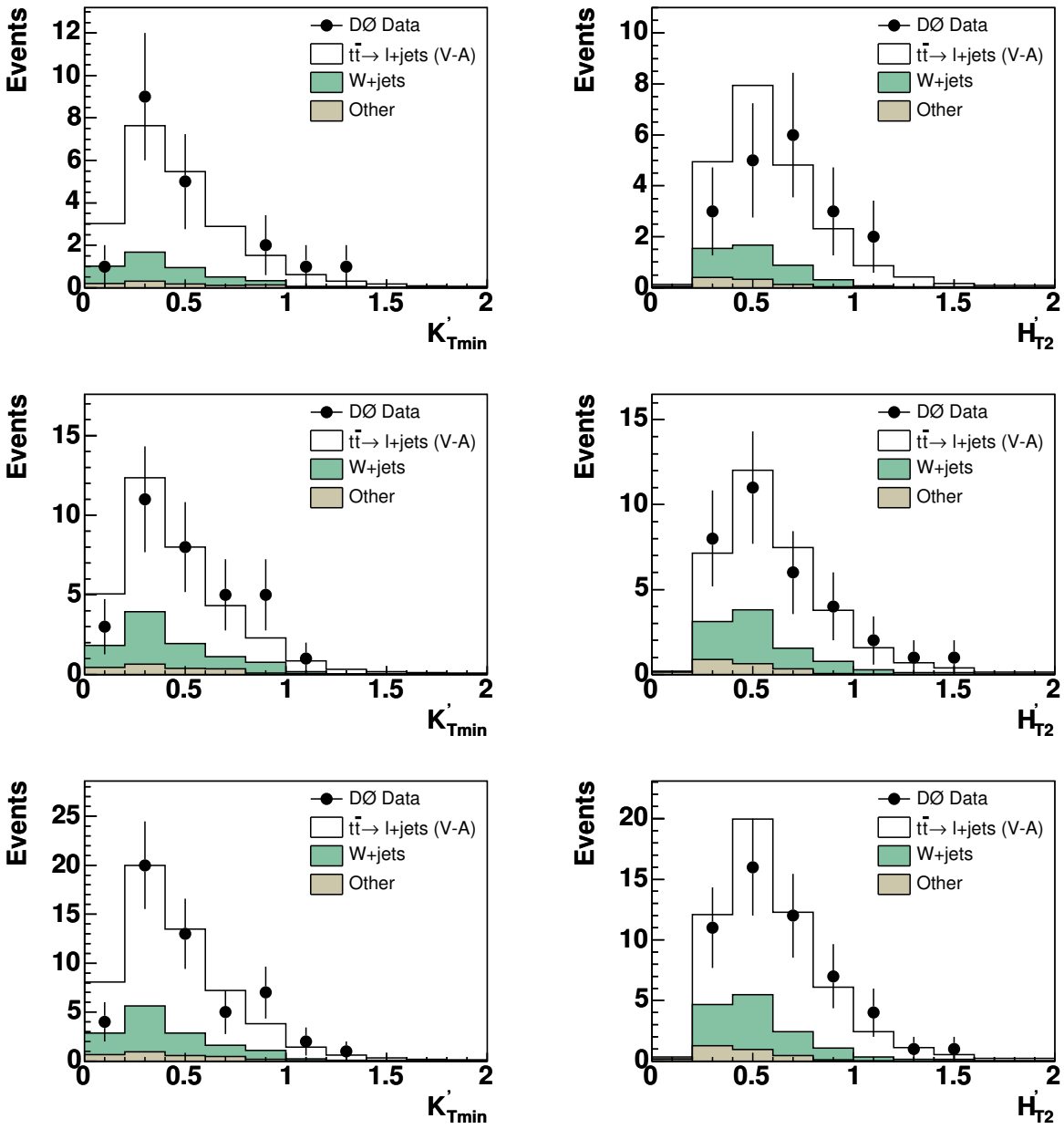

Figure A.5: Comparison between data and Monte Carlo after applying all cuts in the μ+jets channel (top), the e+jets channel (middle) and the combination of both (bottom). The variables are K'_{Tmin} (left) and H'_{T2} (right). The signal and the background samples are scaled to the predicted number of events from the likelihood fit.

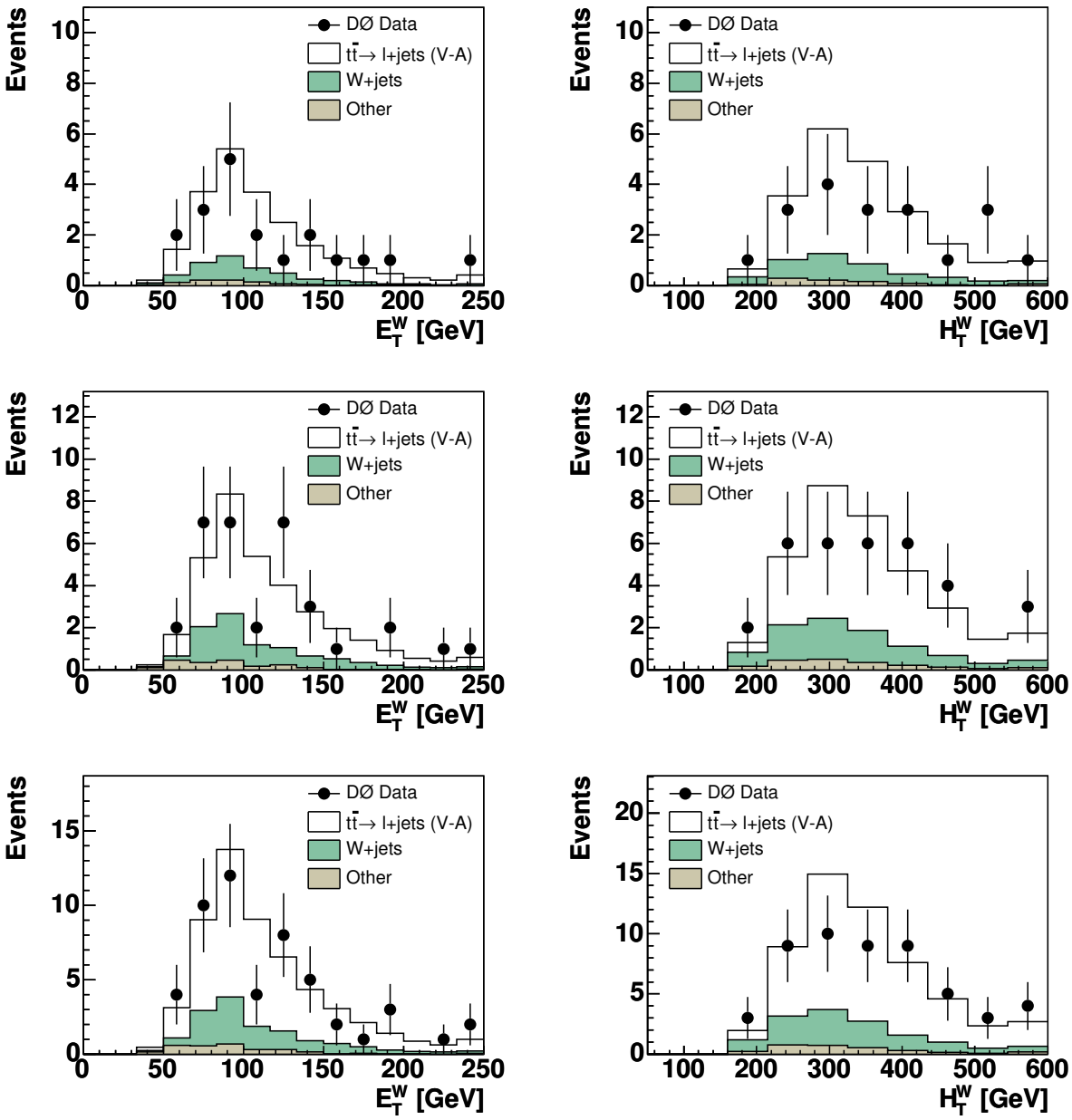

Figure A.6: Comparison between data and Monte Carlo after applying all cuts in the μ+jets channel (top), the e+jets channel (middle) and the combination of both (bottom). The variables are the transverse momentum of the W boson, reconstructed from the lepton and the $\not\!\!E_T$, (left) and H_T^W (right). The signal and the background samples are scaled to the predicted number of events from the likelihood fit.

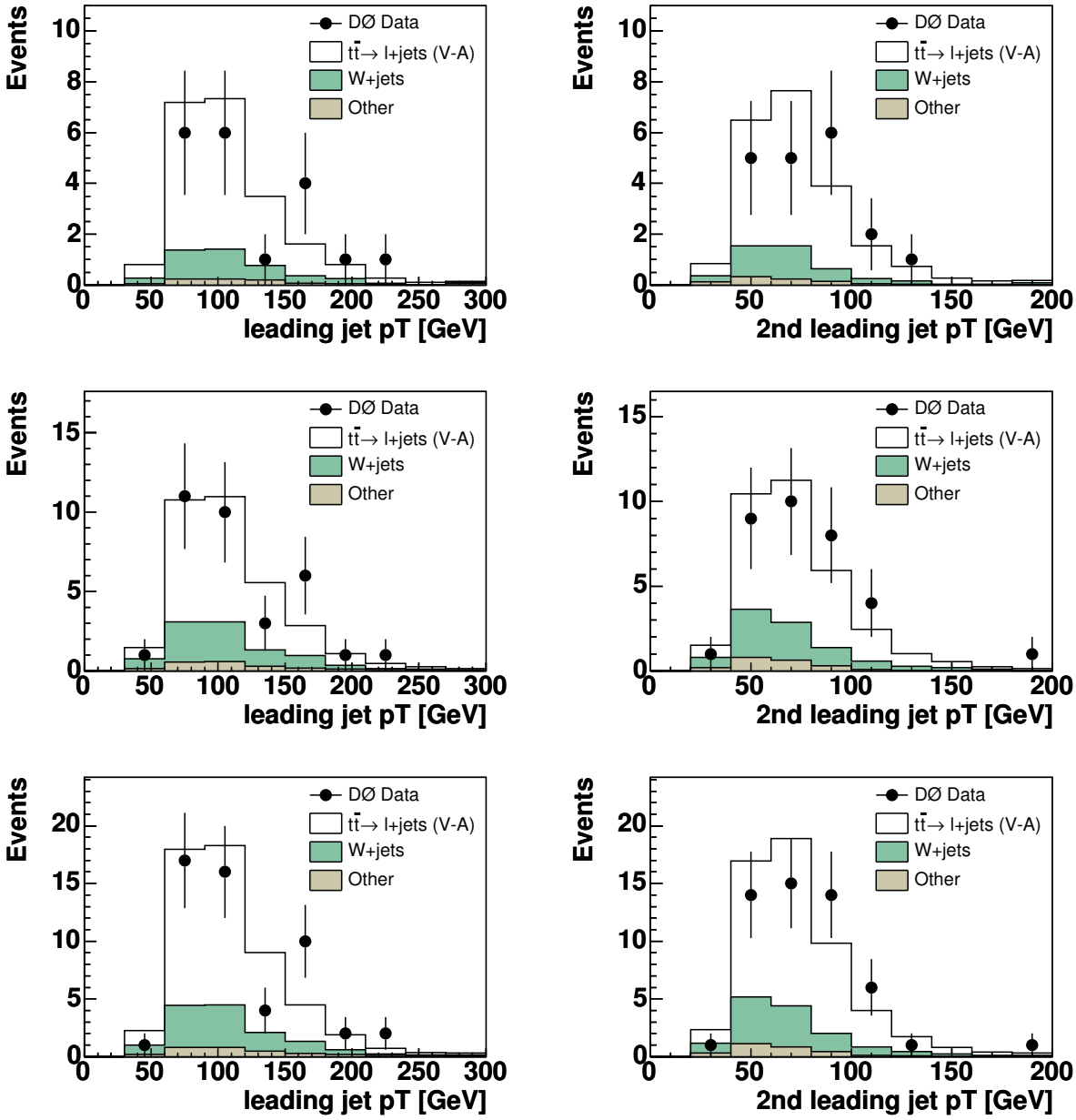

Figure A.7: Comparison between data and Monte Carlo after applying all cuts in the μ+jets channel (top), the e+jets channel (middle) and the combination of both (bottom). The variables are the leading jet p_T (left) and the second leading jet p_T (right). The signal and the background samples are scaled to the predicted number of events from the likelihood fit.

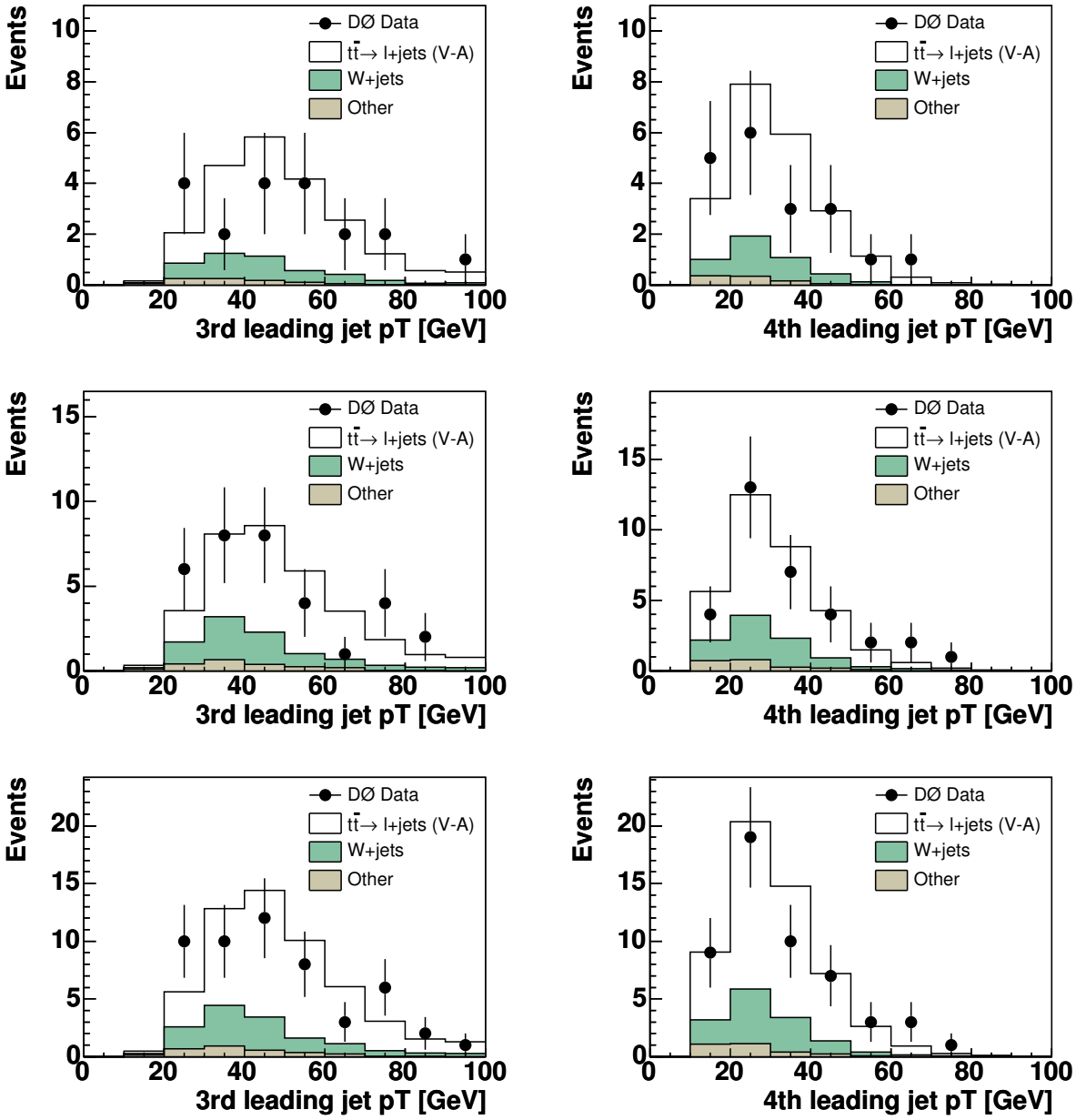

Figure A.8: Comparison between data and Monte Carlo after applying all cuts in the μ+jets channel (top), the e+jets channel (middle) and the combination of both (bottom). The variables are the third leading jet p_T (left) and the fourth leading jet p_T (right). The signal and the background samples are scaled to the predicted number of events from the likelihood fit.

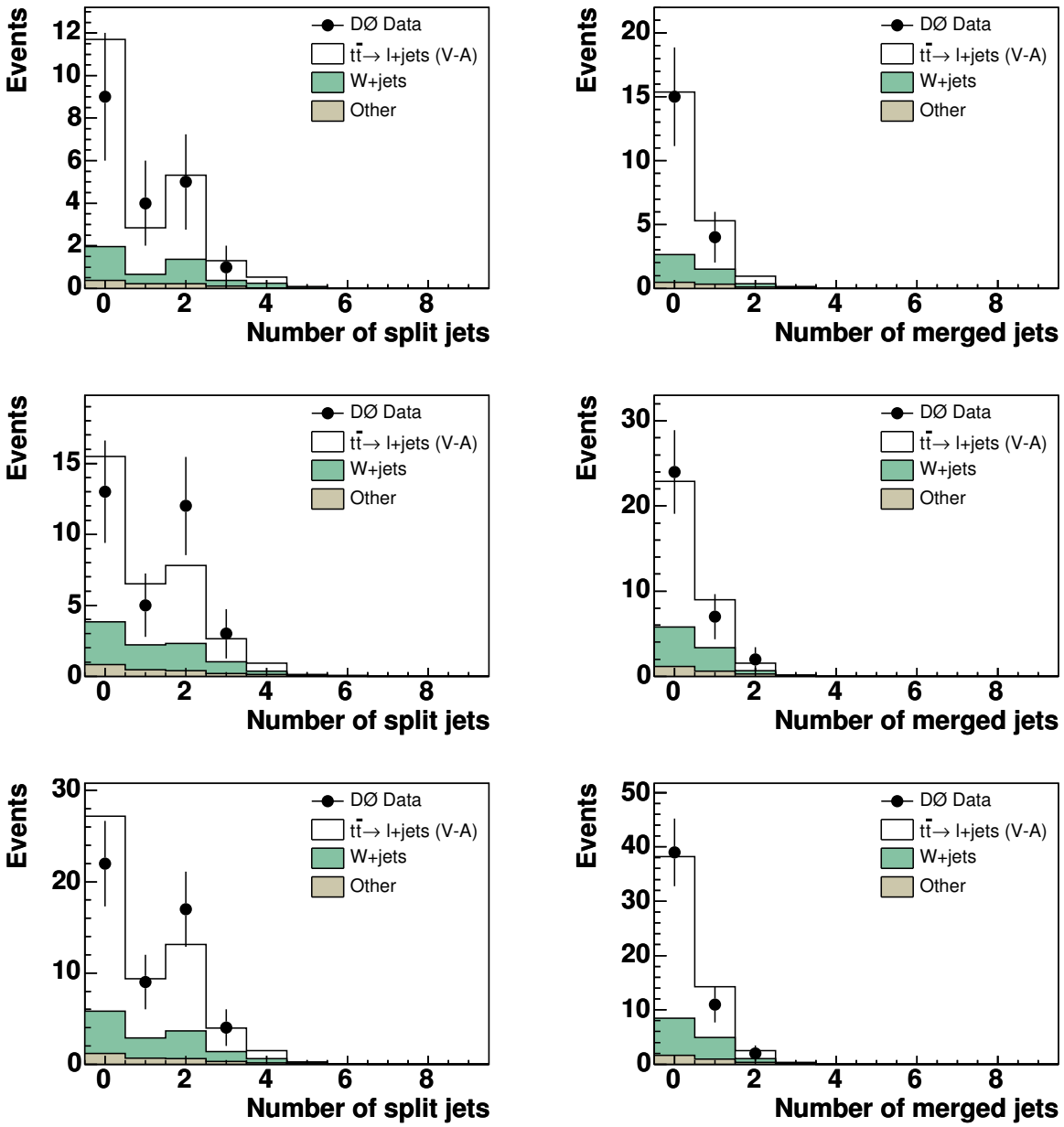

Figure A.9: Comparison between data and Monte Carlo after applying all cuts in the μ+jets channel (top), the e+jets channel (middle) and the combination of both (bottom). The variables are the number of split jets per event (left) and the number of merged jets per event (right). The signal and the background samples are scaled to the predicted number of events from the likelihood fit.

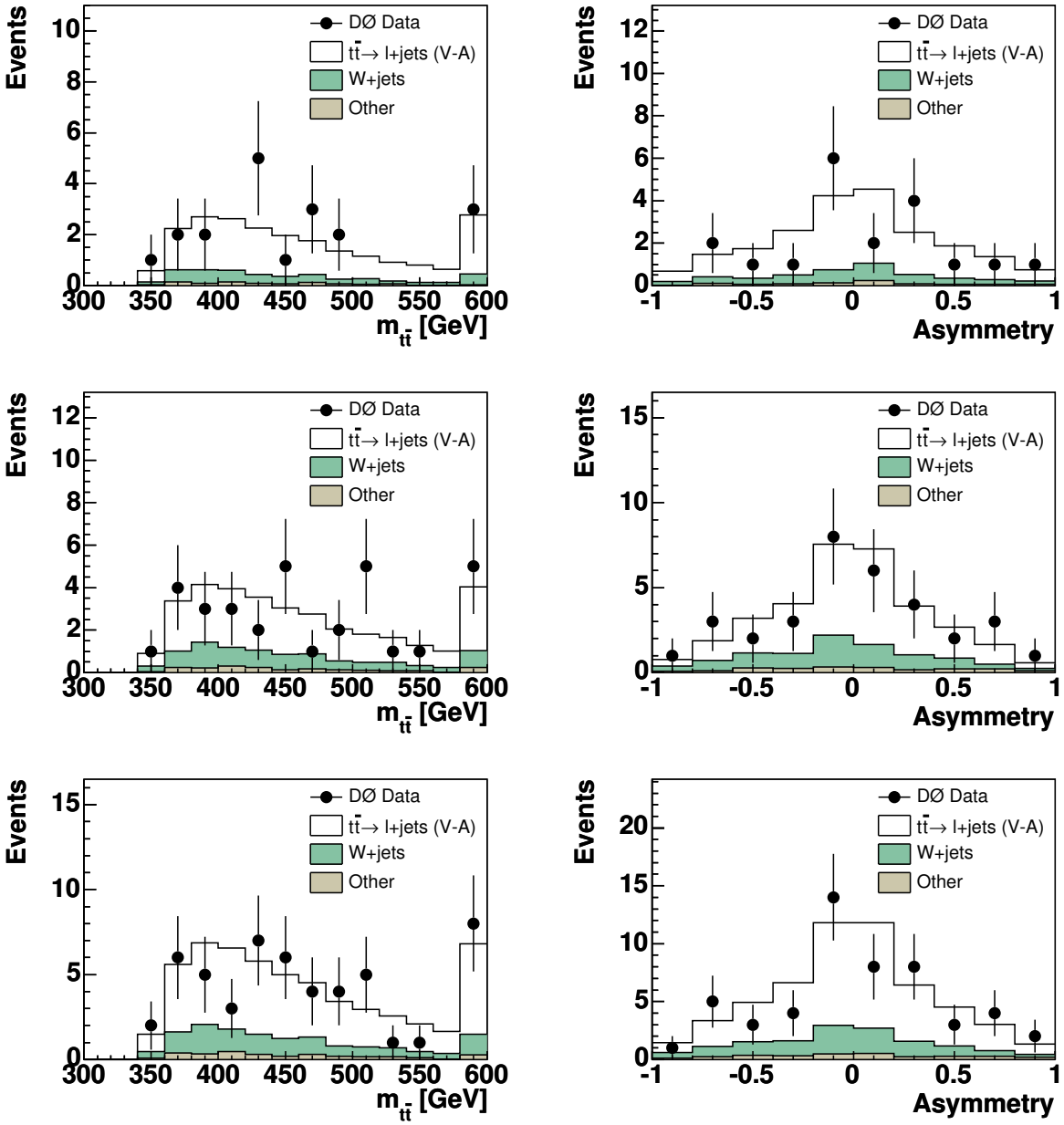

Figure A.10: Comparison between data and Monte Carlo after applying all cuts in the μ+jets channel (top), the e+jets channel (middle) and the combination of both (bottom). The variables are the the invariant $t\bar{t}$ mass (left) and the asymmetry due to spin correlations between the top and the anti-top (right). The signal and the background samples are scaled to the predicted number of events from the likelihood fit.

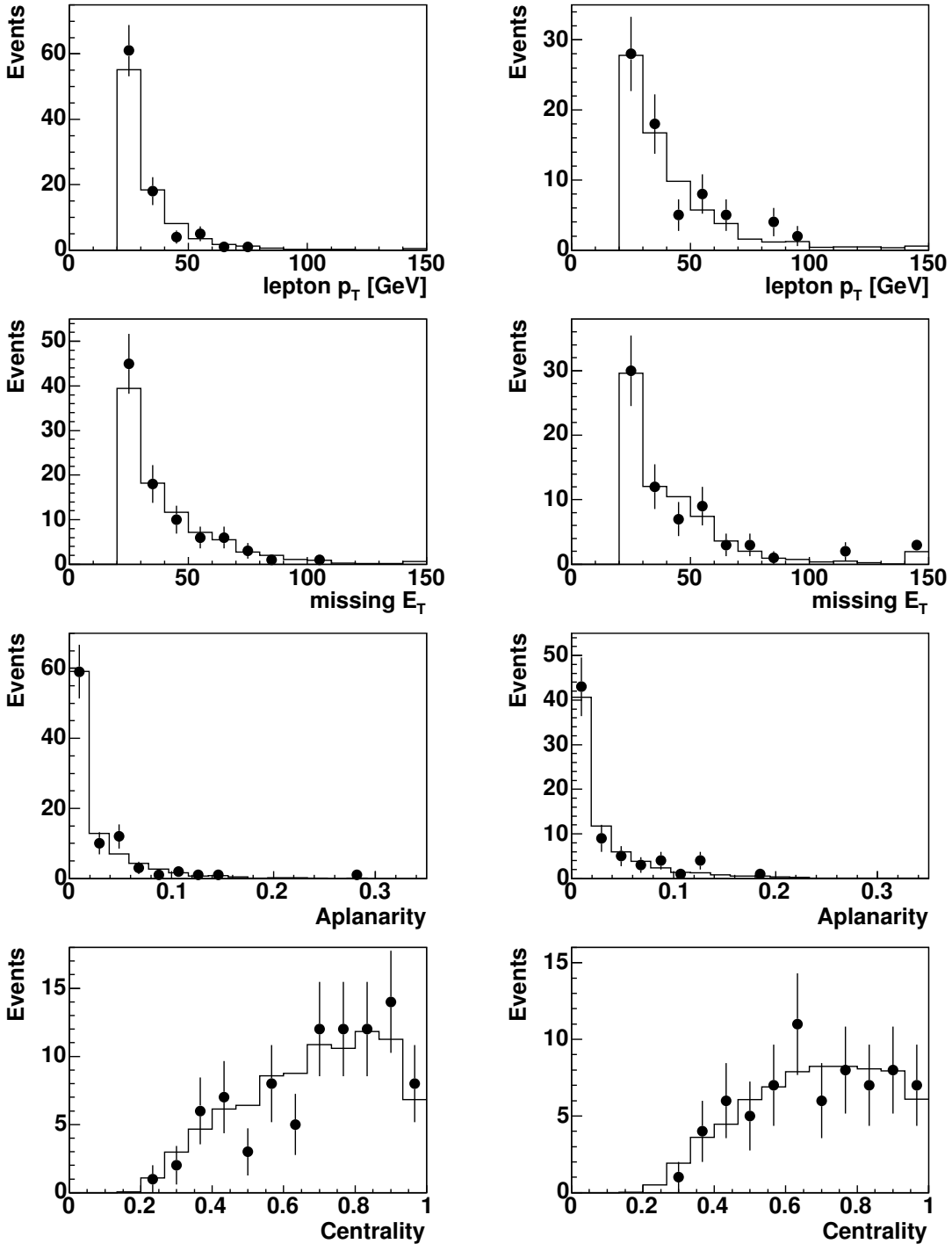

Figure A.11: Comparison between tagged QCD events (points) and untagged QCD events reweighted with the inclusive tag rate function (open histogram) after applying all preselection cuts in the μ+jets channel (left) and the e+jets channel (right). This comparison is for the 2nd jet-multiplicity bin only. The variables are from top to bottom: p_T of the lepton, missing transverse energy, aplanarity and centrality.

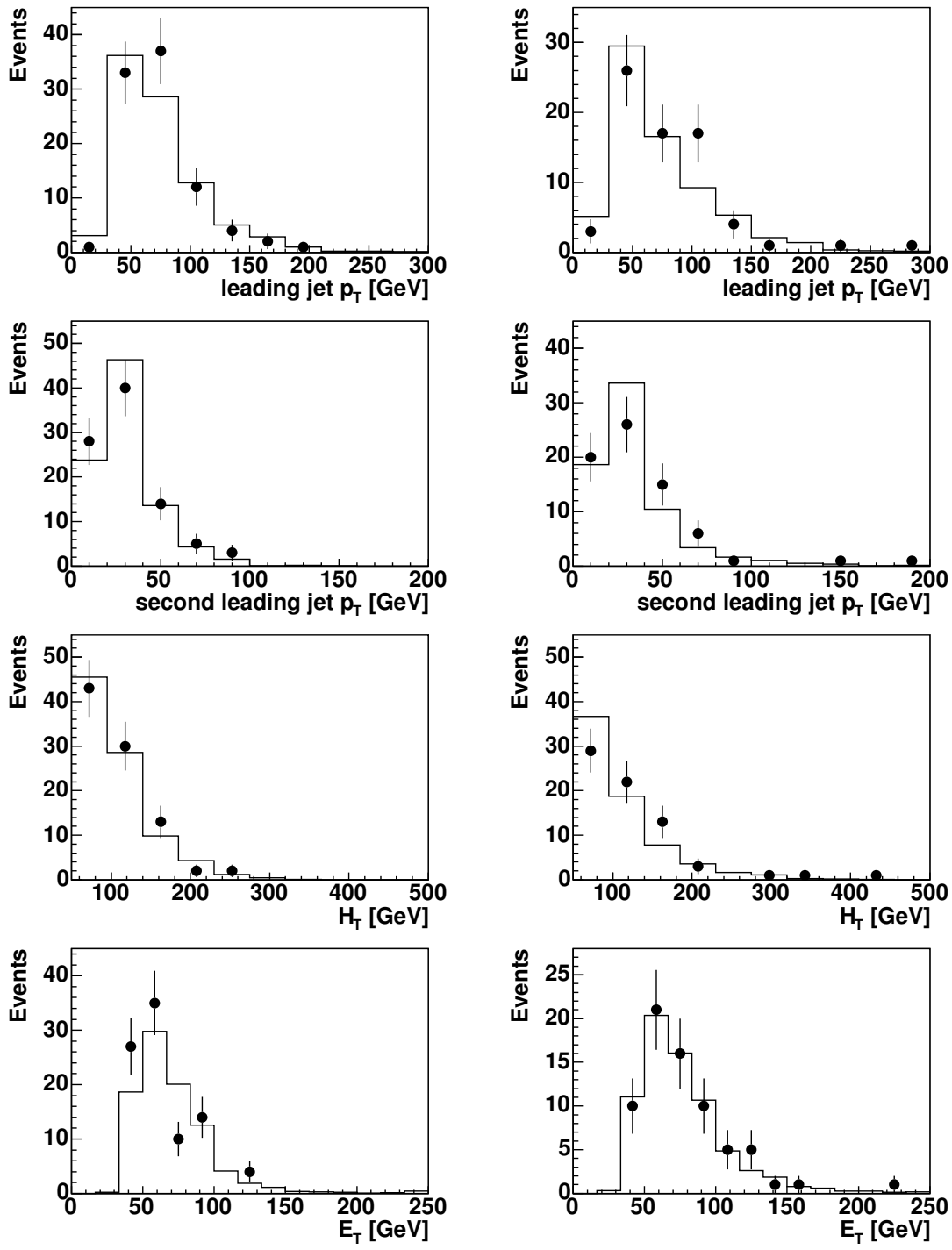

Figure A.12: Comparison between tagged QCD events (points) and untagged QCD events reweighted with the inclusive tag rate function (open histogram) after applying all preselection cuts in the μ+jets channel (left) and the e+jets channel (right). This comparison is for the 2nd jet-multiplicity bin only. The variables are from top to bottom: leading jet p_T, second leading jet p_T, H_T and the sum of the missing transverse energy and the transverse lepton energy.

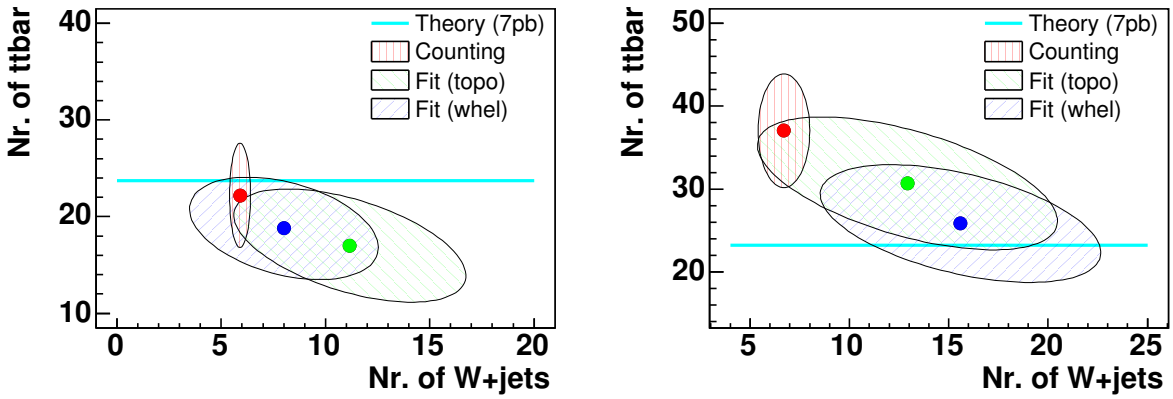

Figure A.13: Comparison of the results from different methods to extract the number of $t\bar{t}$ and W+jets events in the dataset for the muon channel (left) and the electron channel (right). The counting method ("counting") is used by the cross section measurement using lifetime tagging [69], a fit to a 6 variable likelihood discriminant is used by the topological cross section measurement ("topo") and this analysis uses a fit to a 4 variable likelihood as described in section 6.3 ("whel"). The theoretical prediction of 7 pb for $t\bar{t}$ production is also shown. The error ellipses correspond to the 1σ statistical uncertainty.

A.3 Tables of the systematic studies

Tables A.1–A.9 list the observed shift in the average fit values for the different systematic uncertainties as detailed in section 6.6 on 102.

A.4 Events in the final data sample

Tables A.10 and A.11 list all data events that pass the final event selection in the electron and the muon channel respectively.

f_+	JES -1σ	nominal JES	JES $+1\sigma$
0.00	-0.069	-0.003	0.046
0.15	0.092	0.149	0.166
0.30	0.234	0.280	0.270

Table A.1: Average maximum likelihood fit values for jet energy scale values of -1σ, nominal and $+1\sigma$. The average shift observed is 0.040.

f_+	$m_t = 170$ GeV	$m_t = 175$ GeV	$m_t = 180$ GeV
0.00	-0.038	-0.003	0.062
0.15	0.112	0.149	0.190
0.30	0.248	0.280	0.301

Table A.2: Average maximum likelihood fit values for a top quark mass of 170 GeV, 175 GeV and 180 GeV. The average shift observed is 0.038.

f_+	b-tag -1σ	nominal b-tag	b-tag $+1\sigma$
0.00	-0.005	-0.003	-0.001
0.15	0.149	0.149	0.150
0.30	0.280	0.280	0.280

Table A.3: Average maximum likelihood fit values when varying the b-tag parameterizations by -1σ, 0σ and $+1\sigma$. The average shift observed is 0.001.

f_+	Fit -1σ	nominal Fit	Fit $+1\sigma$
0.00	0.013	-0.003	-0.019
0.15	0.142	0.149	0.156
0.30	0.256	0.280	0.301

Table A.4: Average maximum likelihood fit values for the likelihood fit values in the electron channel of -1σ, nominal and $+1\sigma$. The average shift observed is 0.015.

f_+	Fit -1σ	nominal Fit	Fit $+1\sigma$
0.00	0.007	-0.003	-0.012
0.15	0.146	0.149	0.152
0.30	0.267	0.280	0.291

Table A.5: Average maximum likelihood fit values for the likelihood fit values in the muon channel of -1σ, nominal and $+1\sigma$. The average shift observed is 0.008.

f_+	only $WbbJj$	nominal W fractions	only $Wjjjj$
0.00	-0.020	-0.003	-0.020
0.15	0.133	0.149	0.135
0.30	0.264	0.280	0.268

Table A.6: Average maximum likelihood fit values for the variation of the W+jets composition. The average shift observed is 0.015.

f_+	nominal	W+jet background with different scale Q^2
0.00	-0.003	-0.020
0.15	0.149	0.130
0.30	0.280	0.260

Table A.7: Average maximum likelihood fit values using the nominal templates for signal and background and when the W+jets sample is replaced with the light flavor sample in which the scale Q^2 has been changed. The average shift observed is 0.019. Assuming that this uncertainty is uncorrelated with the uncertainty on the flavor composition, the resulting uncertainty due to the different scale is 0.011.

f_+	nominal	$t\bar{t}+j$ as signal
0.00	-0.003	0.018

Table A.8: Average maximum likelihood fit values using the nominal templates for signal and background and when the signal sample is replaced with a mixture of $t\bar{t}$ and $t\bar{t}+j$ according to the relative cross sections. The $t\bar{t}+j$ sample is only available for $f_+ = 0$. The observed shift of 0.021 is taken as systematic uncertainty.

f_+	nominal templates	fluctuated according to statistical uncertainty
0.00	-0.003	0.016
0.15	0.149	0.139
0.30	0.280	0.247

Table A.9: Average maximum likelihood fit values using the nominal templates for signal and background and when the templates were allowed to fluctuate according to their statistical uncertainty. The average shift observed is 0.021.

Run	Event	Tags	discriminant	χ^2 from HitFit	$\cos\theta$
164040	19265127	2	0.99	1.95	-0.61
164539	47070569	1	0.98	6.90	-0.51
168465	4399234	1	0.86	6.48	-0.52
168515	23452583	1	0.94	1.37	0.45
168516	26242720	1	0.63	6.90	0.26
169923	16396718	1	0.77	2.48	-0.69
172591	10663175	1	0.57	6.61	0.52
174424	1062769	1	0.98	1.40	-0.63
175055	23659766	1	0.27	16.63	-0.29
175326	16002373	1	0.71	1.94	0.27
175335	29822900	1	0.66	9.55	-0.55
175343	34082130	1	0.87	8.45	-0.69
176875	16966764	1	0.62	1.82	-0.60
176882	6025400	1	0.48	24.19	-0.12
177275	5302321	1	0.86	1.04	-0.30
178124	45583615	1	0.38	52.81	0.52
178483	30954054	1	0.99	0.96	-0.90
178483	35497013	1	0.66	3.52	-0.34
178733	3210112	2	0.63	13.76	0.70
178790	30505094	1	0.35	2.36	-0.57
179039	19461961	1	0.79	9.76	-0.76
180081	22278985	1	0.42	14.59	-0.83
180335	51564517	1	0.97	1.53	0.94
185868	13687332	1	0.98	6.07	0.74
187863	48985942	1	0.90	1.50	-0.48
188031	34878256	1	0.26	25.61	-0.19
188292	108971	1	0.88	6.37	-0.40
188324	6163900	1	0.63	6.43	0.45
188550	63435382	2	0.96	0.99	-0.58
188904	21333789	1	0.87	4.89	-0.07
188904	22473727	1	0.98	2.25	0.54
189225	7021050	2	0.46	2.59	-0.70
190080	141702197	2	0.82	4.24	0.22

Table A.10: List of all events passing the final selection in the electron channel. For each event the run and event numbers are shown together with the number of b-tags, the value of the likelihood discriminant, the χ^2 from HitFit and the resulting value of the decay angle $\cos\theta$.

Run	Event	Tags	discriminant	χ^2 from HitFit	$\cos\theta$
163524	7542103	2	0.91	8.41	-0.35
167003	27714859	1	0.94	12.82	0.45
173527	2211127	1	0.64	2.45	-0.15
176877	33103694	2	0.92	1.39	0.06
176973	39850057	1	0.88	0.61	-0.75
177034	8492167	1	0.86	12.45	-0.66
178310	11225287	1	0.99	1.85	-0.23
178789	25579312	2	0.98	0.13	0.69
179229	12874690	1	0.77	2.83	-0.48
180130	5357955	1	0.83	1.93	-0.20
180329	24592871	1	0.41	1.37	-0.28
185787	11851805	1	0.54	5.07	0.46
187221	5035077	1	0.55	4.90	-0.43
188298	58551412	2	0.63	6.72	0.53
188925	5787451	1	0.98	4.76	-0.57
189402	69996854	1	0.96	6.47	0.36
189498	56318866	2	0.91	0.23	0.12
189614	27058220	1	0.97	3.26	0.67
189770	28583149	1	0.98	3.17	-0.91

Table A.11: List of all events passing the final selection in the muon channel. For each event the run and event numbers are shown together with the number of b-tags, the value of the likelihood discriminant, the χ^2 from HitFit and the resulting value of the decay angle $\cos\theta$.

B Feasibility study for a measurement of spin correlations in $t\bar{t}$ decays in the lepton+jets channel

Initially, it was foreseen to measure the spin correlations in $t\bar{t}$ events using the lepton+jets decay channel. Due to the slow ramp up of the Tevatron performance and the resulting low integrated luminosity, this plan has been abandoned in favor of the W boson helicity measurement. The initial studies that have been performed in order to determine if a measurement is feasible in the lepton+jets channel are summarized in this chapter.

A measurement of the spin correlations in $t\bar{t}$ events will provide an insight on the production mechanism of $t\bar{t}$ quarks and therefore a test of QCD. It can also be used to search for new interactions or non-standard CP violations in the top sector.

The only existing measurement of spin correlations in $t\bar{t}$ events [101] was performed in the dilepton channel. The advantage of using this channel is that the strength of the spin correlation is maximal for charged leptons. However, there are several disadvantages: the branching ratio for this channel is only about 5%, leading to a small number of $t\bar{t}$ events in the final data sample. In addition, the reconstruction of the rest frame of the two top quarks is an underconstraint problem due to the presence of two neutrinos in the event.

As can be seen from Tab. 2.3 on page 14, the charged lepton is not the only particle that maximizes the strength of the spin correlations: also the quarks with weak isospin $I_3 = -1/2$ ("down-type"), d or s, from the decay of the W boson show the same behavior. For all the other particles, the W boson itself as well as the b quark, the strength is significantly smaller.

The main idea behind this feasibility study is to check if the disadvantages from using the dilepton channel can be avoided by performing the spin correlation analysis in the lepton+jets channel. This channel has a branching ration which is a factor of six higher than the dilepton channel and the rest frame of the two top quarks can be reconstructed using a kinematic fit as only one neutrino is present in the event.

B.1 Monte Carlo samples

In order to study the effects of spin correlations two different Monte Carlo generators are used: PYTHIA [74] and HERWIG [102]. HERWIG correctly simulates the spin correlation effects while PYTHIA does not include these effects. For each Monte Carlo generator 60k events have been generated.

B.2 Parton level results

At the parton level, the four vectors of all the particles and their identity is known. In order to verify that the two Monte Carlo samples, with and without spin correlations, show indeed the predicted behavior, the asymmetry $\mathcal{A}$ is plotted for both samples. Figure B.1 shows the obtained distributions. The charged lepton from the W boson decaying into a lepton and a neutrino and the down-type quark from the W boson that decays into a quark anti-quark pair have been used in the calculation. The obtained distributions are in good agreement with the expectation from the theory (section 2.2.3 on page 13). In addition, also the expected dependence on the chosen spin quantization axis can be seen.

B.3 Identification of the down-type quark

In the lepton+jets channel only one charged lepton is available. To measure the spin correlations a decay particle from the top quark as well as from the antitop quark is needed. The obvious choice of using the two b quarks in the event leads to a spin correlation coefficient $C_{b\bar{b}}$ that is a factor of about 6 smaller than in the case of two charged leptons:

$$C_{b\bar{b}} = C_{\ell\bar{\ell}} \cdot \left(\frac{\lambda_b}{\lambda_\ell}\right)^2 \approx 0.17 \cdot C_{\ell\bar{\ell}} \,, \tag{B.1}$$

where $C_{\ell\bar{\ell}}$ is the spin correlation coefficient for two charged leptons and λ_b and λ_ℓ are the correlation coefficient for a b quark and a charged lepton, respectively, as given in Tab. 2.3 on page 14. The same reduction would occur when using the two W bosons, as their correlation coefficient is identical to that of the b quarks at tree level.

The remaining option is to use the down-type quark from the W decay together with the charged lepton. If the down-type quark could be identified with 100% accuracy, the spin correlation coefficient would be identical to $C_{\ell\bar{\ell}}$. Even without any knowledge about which of the two quarks from the W boson decay is the down-type quark, the

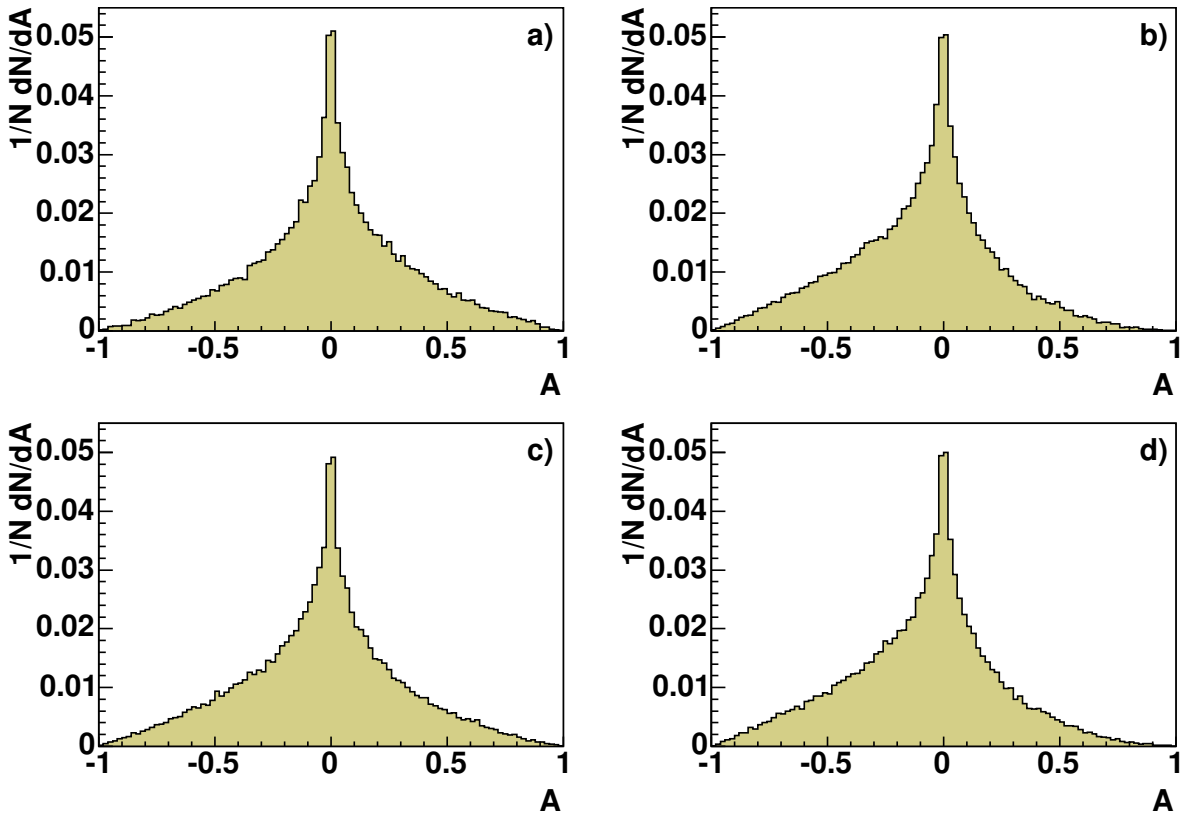

Figure B.1: Distribution in the product of $\cos\theta_+ \cdot \cos\theta_- \equiv A$ at the parton level for uncorrelated $t\bar{t}$ events in the beam basis (a) and correlated $t\bar{t}$ events in the beam basis (b), helicity basis (c) and off-diagonal basis (d). The measured asymmetry values are: a) $(-2.1 \pm 6.0) \cdot 10^{-3}$, b) $(205.8 \pm 6.1) \cdot 10^{-3}$, c) $(78.8 \pm 5.8) \cdot 10^{-3}$ and d) $(192.9 \pm 6.1) \cdot 10^{-3}$.

spin correlation coefficient $C_{q\ell}$ is higher than the corresponding one for b quarks:

$$C_{q\ell} = \frac{0.5 \cdot \lambda_u + 0.5 \cdot \lambda_d}{\lambda_\ell} C_{\ell\bar{\ell}} \approx 0.35 \cdot C_{\ell\bar{\ell}} \,, \tag{B.2}$$

where λ_u and λ_d are the correlation coefficients for up-type, i.e. weak isospin $I_3 = +1/2$, and down-type particles, respectively.

In principle the following differences between the two quarks from the W boson decay can be exploited in order to identify the down-type quark:

Charge: The charge of the W boson that decays into two quarks can be inferred from the charge of the lepton in the event. Therefore the charge of the up-type and the down-type quark in a given event is known. However, the difference between these two is only $\pm 1/3$. Together with the fact that a determination of the jet charge is very difficult [103], this difference does not provide an improvement over randomly choosing one of the two quark as the down-type quark.

Flavor: One obvious difference between the up-type and the down-type quarks is the flavor of the quarks. An identification of the quark flavor by e.g. explicitly reconstructing K or D mesons would be a possibility to distinguish between up- and down-type quarks. However, this identification only works for the second generation, i.e. strange or charm quarks, and reduces the efficiency significantly due to e.g. inefficiencies in the track reconstruction.

Energy: A third option is to make use of the $V - A$ structure of the weak interaction: the conservation of angular momentum together with the $V - A$ structure of the weak interaction leads to a difference in the energy distribution for the down-type and the up-type quarks. On average, the down-type quark is less energetic than the up-type quark as it is more often emitted opposite to the flight direction of the W boson: a consequence from the angular distribution $\omega(\theta)$ as described in section 2.2.4. The down-type quark can therefore be inferred from the energy distribution [19]. This yields the correct identification of the down-type quark in about 60% of the events.

By using the difference in the energy, the spin correlation coefficient $C_{q\ell}$ is reduced to

$$C_{q\ell} = \frac{0.4 \cdot \lambda_u + 0.6 \cdot \lambda_d}{\lambda_\ell} C_{\ell\bar{\ell}} \approx 0.5 \cdot C_{\ell\bar{\ell}} \,. \tag{B.3}$$

B.4 Detector resolution

In order to estimate the influence of the detector, especially its limited resolution, the four vectors at the parton level are replaced by the four vectors of the reconstructed

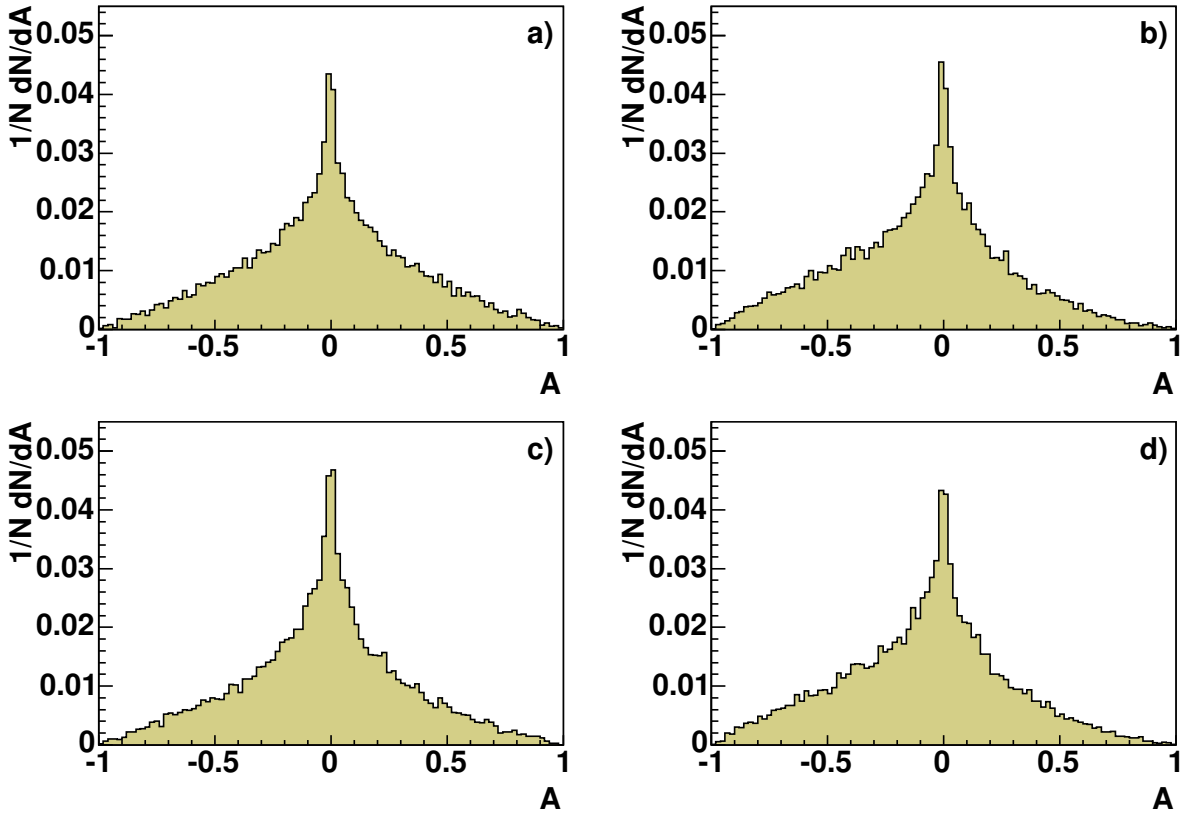

Figure B.2: Distribution in the product of $\cos\theta_+ \cdot \cos\theta_- \equiv A$ at the jet reconstruction level for uncorrelated $t\bar{t}$ events in the beam basis (a) and correlated $t\bar{t}$ events in the beam basis (b), helicity basis (c) and off-diagonal basis (d). The measured asymmetry values are: a) $(38 \pm 12) \cdot 10^{-3}$, b) $(192 \pm 11) \cdot 10^{-3}$, c) $(69 \pm 11) \cdot 10^{-3}$ and d) $(169 \pm 11) \cdot 10^{-3}$.

objects in the event. The top quarks are reconstructed by the kinematic fit described in section 4.8 using in addition a constraint on the top quark mass by setting it to be 175 GeV.

The identification of the individual jets in the event is done by matching the original partons with the jets in $\eta - \phi$ space. Only events are selected, where the jets could be matched to the quarks in an unambiguous way. Figure B.2 shows the effect of the finite detector and reconstruction resolution on the measured asymmetry values. On average the asymmetry is reduced by 15% compared to the case when using the true parton momenta.

B.5 Jet identification

In the studies described so far the association between partons and jets was made using the information from the Monte Carlo generator. In the data the assignment from jets to partons must be done by the kinematic fit: it assigns the b quarks to jets and the two quarks from the W boson decay to two jets. However, the fit does not provide information about which jet from the W boson is the down-type jet. This has to be done using the information on the jet energy as explained in section B.3.

Three different scenarios have been evaluated:

- Assuming an efficiency of 100% for the identification of the down-type quark from the decay of the W boson and a b-tag efficiency as given by the SVT algorithm applied directly on Monte Carlo, i.e. not using the parameterizations from section 4.7.2. This was necessary, because at the time of this study the parameterizations were not yet available. As a consequence, the b-tag efficiency is slightly higher than in reality.
- Assuming a b-tag efficiency of 100%, i.e. the number of possible jet combinations in the kinematic fit is reduced to two as only the two b jets can be interchanged. The identification of the down-type quark is done using the jet energies.
- Using no Monte Carlo information, i.e. the minimal χ^2 solution from the kinematic fit is used together with a b-tag applied directly to the events. The down-type jet is selected based on the jet energies.

Table B.1 lists the asymmetry values obtained in these different scenarios together with the asymmetry measured in $W+$ jets background events. The asymmetry is most sensitive to the correct identification of down-type quarks, however also the b-tag efficiency plays an important role as the combinatorial background reduces the effect of the spin correlation. The background from $W+$ jets production does not show a significant asymmetry.

B.6 Conclusion

The lepton+jets channel provides a factor of six more statistics compared to the dilepton channel for the measurement of the spin correlations. In addition, the reconstruction of the rest frames of the two top quarks can be done by a constraint kinematic fit in this channel. However, the necessary identification of the down-type jet from the decay of the W boson turns out to be a crucial point in the analysis. By making use of the difference in the energy distribution, the down-type jet can be identified in about

Stage	Asymmetry $\times 10^3$			
	uncorrelated	beam basis	helicity basis	off-diagonal basis
Parton level	-2 ± 6	206 ± 6	79 ± 6	193 ± 6
100% b, d eff.	38 ± 12	179 ± 11	69 ± 11	169 ± 11
100% d efficiency	27 ± 11	110 ± 10	38 ± 10	107 ± 10
100% b efficiency	25 ± 12	70 ± 11	29 ± 11	73 ± 11
Detector level	14 ± 16	50 ± 15	17 ± 15	42 ± 15
$W+$ jets		-13 ± 20	-8 ± 20	-5 ± 20

Table B.1: Asymmetry values obtained at different stages of the analysis: using purely the information from the Monte Carlo generator (Parton level), using reconstructed objects and the kinematic fit but taking the jet-parton assignment from the Monte Carlo for both, b quarks and the down-type quark from the W boson decay (100% b, d eff.), using the jet-parton assignment as given by the minimal χ^2 solution of the kinematic fit but assuming an efficiency of 100% to identify the down-type quark (100% d efficiency), using the jet-parton assignment from the kinematic fit given a b-tag efficiency of 100% and choosing the down-type quark based only on the energy of the jets (100% b efficiency), and using no Monte Carlo information at all (Detector level). The last row shows the measured asymmetry in $W+$ jets events. The quoted uncertainties are calculated using the full statistics of the Monte Carlo samples.

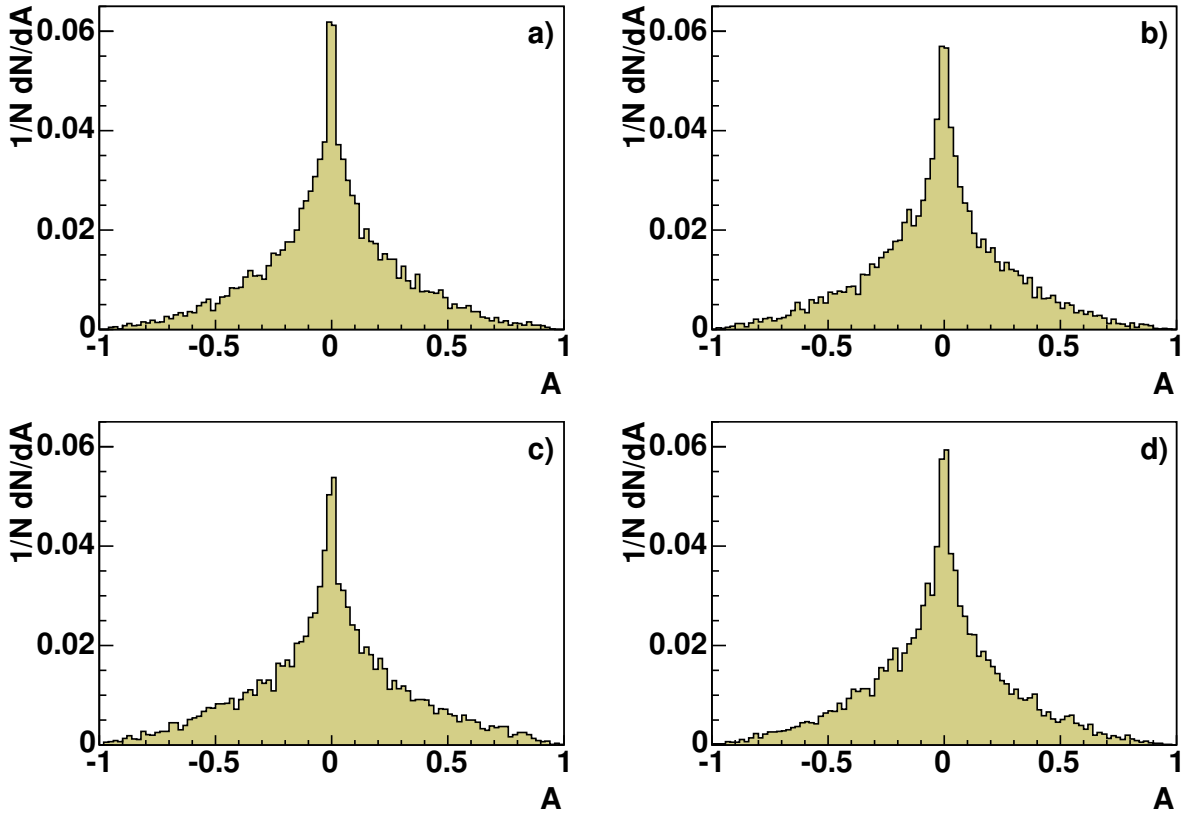

Figure B.3: Distribution in the product of $\cos\theta_+ \cdot \cos\theta_-$ at the detector level for uncorrelated $t\bar{t}$ events (a) and correlated $t\bar{t}$ events in the beam basis (b), helicity basis (c) and off-diagonal basis (d). The measured asymmetry values are: a) $(14 \pm 16) \cdot 10^{-3}$, b) $(50 \pm 15) \cdot 10^{-3}$, c) $(17 \pm 15) \cdot 10^{-3}$ and d) $(42 \pm 15) \cdot 10^{-3}$.

60% of all cases. This assumes that the two jets from the W decay have already be identified by the kinematic fit.

Taking into account the detector resolution, the combinatorial problem in the kinematic fit and a b-tag efficiency which is slightly higher than in reality, the measured asymmetry is reduced by a factor of about four. Nevertheless, a difference between uncorrelated and correlated $t\bar{t}$ events remains visible.

It is therefore feasible to perform an analysis of the $t\bar{t}$ spin correlations in the lepton+jets channel. However, the increase in statistics due to the higher branching ration will not lead to an improvement in the achievable precision due to the reduced sensitivity. But it can provide a good cross check of the result obtained in the dilepton channel. Overall, the expected precision achievable at the Tevatron is about two standard deviations [22].

Bibliography

[1] S. L. Glashow. Partial symmetries of weak interactions. *Nucl. Phys.*, 22:579–588, 1961.

[2] Steven Weinberg. A model of leptons. *Phys. Rev. Lett.*, 19:1264–1266, 1967.

[3] Abdus Salam and J. C. Ward. Electromagnetic and weak interactions. *Phys. Lett.*, 13:168–171, 1964.

[4] Murray Gell-Mann. Symmetries of baryons and mesons. *Phys. Rev.*, 125:1067–1084, 1962.

[5] Y. Ne'eman. Derivation of strong interactions from a gauge invariance. *Nucl. Phys.*, 26:222–229, 1961.

[6] G. Zweig. An $SU(3)$ model for strong interaction symmetry and its breaking. CERN-TH-412.

[7] M. Kaku. Quantum field theory: a modern introduction. New York, USA: Oxford Univ. Pr. (1993) 785 p.

[8] F. Halzen and Alan D. Martin. Quarks and leptons: an introductory course in modern particle physics. New York, Usa: Wiley (1984) 396p.

[9] D. J. Griffiths. Introduction to elementary particles. New York, USA: Wiley (1987) 392p.

[10] Y. Fukuda et al. Evidence for oscillation of atmospheric neutrinos. *Phys. Rev. Lett.*, 81:1562–1567, 1998.

[11] S. Eidelman et al. Review of particle physics. *Phys. Lett.*, B592:1, 2004.

[12] M. Kobayashi and T. Maskawa. CP violation in the renormalizable theory of weak interaction. *Prog. Theor. Phys.*, 49:652–657, 1973.

[13] Peter W. Higgs. Broken symmetries, massless particles and gauge fields. *Phys. Lett.*, 12:132–133, 1964.

[14] Scott Willenbrock. The standard model and the top quark, *hep-ph/0211067*. 2002.

[15] A combination of preliminary electroweak measurements and constraints on the standard model, *hep-ex/0412015*. 2004.

[16] Nikolaos Kidonakis and Ramona Vogt. Next-to-next-to-leading order soft-gluon corrections in top quark hadroproduction. *Phys. Rev.*, D68:114014, 2003.

[17] V. Abazov et al. Search for single top quark production in p anti-p collisions at s**(1/2) = 1.96-TeV, *hep-ex/0505063*. 2005.

[18] Adam F. Falk and Michael E. Peskin. Production, decay, and polarization of excited heavy hadrons. *Phys. Rev.*, D49:3320–3332, 1994.

[19] W. Bernreuther, A. Brandenburg, Z. G. Si, and P. Uwer. Top quark pair production and decay at hadron colliders. *Nucl. Phys.*, B690:81–137, 2004.

[20] Gregory Mahlon and Stephen J. Parke. Maximizing spin correlations in top quark pair production at the Tevatron. *Phys. Lett.*, B411:173–179, 1997.

[21] Gregory Mahlon. Spin issues in t anti-t production and decay, *hep-ph/9811281*. 1998.

[22] Suyong Choi. Spin correlation in t anti-t production from proton anti-proton collisions at $\sqrt{s} = 1.8$ TeV. FERMILAB-THESIS-1999-07.

[23] Gordon L. Kane, G. A. Ladinsky, and C. P. Yuan. Using the top quark for testing standard model polarization and CP predictions. *Phys. Rev.*, D45:124–141, 1992.

[24] R. H. Dalitz and Gary R. Goldstein. The decay and polarization properties of the top quark. *Phys. Rev.*, D45:1531–1543, 1992.

[25] Charles A. Nelson, Brian T. Kress, Marco Lopes, and Thomas P. McCauley. General tests for t –> W+ b couplings at hadron colliders. *Phys. Rev.*, D56:5928–5944, 1997.

[26] H. S. Do, S. Groote, J. G. Korner, and M. C. Mauser. Electroweak and finite width corrections to top quark decays into transverse and longitudinal W-bosons. *Phys. Rev.*, D67:091501, 2003.

[27] M. A. B. Beg, R. V. Budny, Rabindra N. Mohapatra, and A. Sirlin. Manifest left-right symmetry and its experimental consequences. *Phys. Rev. Lett.*, 38:1252, 1977.

[28] Soo-hyeon Nam. B anti-B mixing and CP violation in $SU(2)_L x SU(2)_R x U(1)$ models. *Phys. Rev.*, D66:055008, 2002.

[29] Qaisar Shafi and Zurab Tavartkiladze. $SU(4)_c \times SU(2)_L \times SU(2)_R$ model from 5D supersymmetric $SU(4)_c \times SU(4)_{L+R}$. *Phys. Rev.*, D66:115002, 2002.

[30] H. S. Goh, R. N. Mohapatra, and Siew-Phang Ng. Minimal SUSY $SO(10)$, $b\tau$ unification and large neutrino mixings. *Phys. Lett.*, B570:215–221, 2003.

[31] Manfred Lindner and George Triantaphyllou. Mirror families in electro-weak symmetry breaking. *Phys. Lett.*, B430:303–313, 1998.

[32] Gary J. Feldman and Robert D. Cousins. A unified approach to the classical statistical analysis of small signals. *Phys. Rev.*, D57:3873–3889, 1998.

[33] S. Abachi et al. The DØ detector. *Nucl. Instrum. Meth.*, A338:185–253, 1994.

[34] S. Abachi et al. The DØ upgrade: the detector and its physics. FERMILAB-PUB-96-357-E.

[35] Abid Mahmood Patwa. The forward preshower system and a study of the J/psi trigger with the DØ detector. FERMILAB-THESIS-2002-04.

[36] The DØ Collaboration. DØ Silicon tracker technical design report. DØ Note 2169.

[37] The DØ Collaboration. The DØ upgrade central fiber tracker: technical design report. DØ Note 4164.

[38] D. Lincoln. A large statistics study of the performance and yields of generation-6 VLPCs (HISTE-VI). *Nucl. Phys. Proc. Suppl.*, 78:281–286, 1999.

[39] M. Adams et al. Design report of the central preshower detector for the DØ upgrade. DØ Note 3014.

[40] A. Gordeev et al. Technical design report of the forward preshower detector for the DØ upgrade. DØ Note 3445.

[41] L. Sawyer et al. Technical design report for the upgrade of the ICD for DØ Run 2. DØ Note 2686.

[42] G. C. Blazey. The DØ Run II trigger. To be published in the proceedings of 10th IEEE Real-Time Computer Applications in Nuclear, Particle and Plasma Physics (RT 97), Beaune, France, 22-26 Sep 1997.

[43] D. Chapin et al. The DØ level 3 data acquistion system. *ECONF*, C0303241:TUGP010, 2003.

[44] C. Schmitt. Split CFT clusters. DØ Note 4092.

[45] A. Khanov. HTF: histogramming method for finding tracks. The algorithm description. DØ Note 3778.

[46] G. Borissov. Ordering a chaos or ... technical details of AA tracking. `http://www-d0.fnal.gov/atwork/adm/d0_private/2003-02-28/adm_talk.ps`.

[47] H. Greenlee. The DØ kalman track fit. DØ Note 4303 Version 2.

[48] A. Garcia-Bellido et al. Primary vertex certification in p14. DØ Note 4320.

[49] Ariel Schwartzman. Measurement of the $B^{\pm}$ lifetime and top quark identification using secondary vertex b-tagging. FERMILAB-THESIS-2004-21.

[50] A. Schwartzman and M. Narain. b-quark jet identification via secondary vertex reconstruction. DØ Note 4080.

[51] A. Schwartzman and M. Narain. b-quark jet identification via secondary vertex reconstruction in DØ reco p13 Software. DØ Note 4081.

[52] L. Duflot and M. Ridel. An energy flow algorithm for DØ. DØ Note 3927.

[53] U. Bassler and G. Bernardi. Towards a coherent treatment of calorimetric energies: missing transverse energy, jets, E.M. objects and the T42 algorithm. DØ Note 4124.

[54] J. Vlimant et al. Technical description of the T42 algorithm for the calorimeter noise suppression. DØ Note 4146.

[55] G. Blazey et al. Run II jet physics. DØ Note 3750.

[56] B. Abbott et al. Determination of the absolute jet energy scale in the DØ calorimeters. *Nucl. Instrum. Meth.*, A424:352–394, 1999.

[57] F. Canelli et al. First jet energy scale at DØ in Run II (for p10 data and monte carlo). DØ Note 4110.

[58] `http://www-d0.fnal.gov/phys_id/jes/d0_private/certified/v5.3/`.

[59] Top Physics Working Group. Direct measurement of the top quark mass in the lepton+jets channel using Run II data (general note). DØ Note 4426 v0.1.

[60] M. Agelou et al. DØ Top analyses and data sample for the winter conference 2004. DØ Note 4419.

[61] C. Clement et al. Measurement of the ttbar production cross-section at $\sqrt{s} = 1.96$ TeV in the electron+jets final state using a topological method. DØ Note 4662.

[62] J. Kozminski et al. Electron likelihood in p14. DØ Note 4449.

[63] R. Zitoun. Study of the non linearity of the DØ calorimeter readout chain. DØ Note 3997.

[64] S. Crepe-Renaudin. Energy corrections for geometry effects for electrons in Run II. DØ Note 4023.

[65] C. Clement et al. MuonID certification for p14. DØ Note 4350.

[66] T. Golling. Measurement of the $t\bar{t}$ production cross-section at $\sqrt{s} = 1.96$ TeV in the muon+jets final state using a topological method. DØ Note 4667.

[67] G. Brandenburg et al. Charged track multiplicity in B meson decay. *Phys. Rev.*, D61:072002, 2000.

[68] L. Feligioni et al. Update on b-quark jet identification with secondary vertex reconstruction using DØreco version p14. DØ Note 4414.

[69] C. Clement et al. Measurement of the ttbar production cross-section at $\sqrt{(s)} = 1.96$ TeV using lifetime tagging. DØ Note 4625.

[70] J. Peter Berge, Frank T. Solmitz, and Horace D. Taft. *Rev. of Scientific Instruments*, 32 (5):538–548, 1961.

[71] Scott Stuart Snyder. Measurement of the top quark mass at DØ. FERMILAB-THESIS-1995-27.

[72] Michelangelo L. Mangano, Mauro Moretti, Fulvio Piccinini, Roberto Pittau, and Antonio D. Polosa. ALPGEN, a generator for hard multiparton processes in hadronic collisions. *JHEP*, 07:001, 2003.

[73] H. L. Lai et al. Global QCD analysis of parton structure of the nucleon: CTEQ5 parton distributions. *Eur. Phys. J.*, C12:375–392, 2000.

[74] Torbjorn Sjostrand et al. High-energy-physics event generation with PYTHIA 6.1. *Comput. Phys. Commun.*, 135:238–259, 2001.

[75] Application Software Group (CERN). GEANT – Detector description and simulation tool. CERN Program Library Long Writeup W5013.

[76] M. Angelou et al. Top trigger efficiency measurements and the top_trigger package. DØ Note 4512.

[77] M. A. Dobbs et al. Les Houches guidebook to Monte Carlo generators for hadron collider physics. 2004.

[78] E. Boos et al. CompHEP 4.4: automatic computations from lagrangians to events. *Nucl. Instrum. Meth.*, A534:250–259, 2004.

[79] J. Körner, private communication.

[80] B. Abbott et al. Extraction of the width of the W boson from measurements of $\sigma(p\bar{p} \rightarrow W + X) \times B(W \rightarrow e\nu)$ and $\sigma(p\bar{p} \rightarrow Z + X) \times B(Z \rightarrow ee)$ and their ratio. *Phys. Rev.*, D61:072001, 2000.

[81] E. Barberis et al. The matrix method and its error calculation. DØ Note 4564.

[82] B. Abbott et al. Measurement of the top quark pair production cross section in p anti-p collisions using multijet final states. *Phys. Rev.*, D60:012001, 1999.

[83] V. M. Abazov et al. Measurement of the top quark mass in all-jet events. *Phys. Lett.*, B606:25–33, 2005.

[84] B. Abbott et al. Direct measurement of the top quark mass at DØ. *Phys. Rev.*, D58:052001, 1998.

[85] Kevin Black et al. Measurement of the top quark mass in the lepton+jets channel using DØ Run II data: the low bias template method. DØ Note 4707.

[86] Martijn Mulders and Michele Weber. Top mass measurement with b-tagging in the lepton+jets channel using the ideogram method in Run II. DØ Note 4705.

[87] V. M. Abazov et al. Search for right-handed W bosons in top quark decay. *Phys. Rev.*, D72:011104, 2005.

[88] C. Schmitt. Measurement of the W boson helicity in $t\bar{t}$ decays at $\sqrt{s} = 1.96$ TeV in the lepton+jets final states using a lifetime tag. DØ Note 4704.

[89] V. Buescher et al. Recommendation of the ad-hoc committee on limit-setting procedures to be used by DØ in Run II. DØ Note 4629.

[90] B. Gmyrek et al. Measurement of the W helicity in top quark decays. DØ Note 4687.

[91] C. Schmitt et al. Combination of b-tagged and topological measurements of the W helicity in top quark decays. DØ Note 4686.

[92] F. Hubaut et al. Measurement of the W polarization in top decays with semileptonic $t\bar{t}$ events. ATL-COM-PHYS-2005-015.

[93] M. Beneke et al. Top quark physics. 2000.

[94] T. Affolder et al. Measurement of the helicity of W bosons in top quark decays. *Phys. Rev. Lett.*, 84:216–221, 2000.

[95] V. M. Abazov et al. A precision measurement of the mass of the top quark. *Nature*, 429:638–642, 2004.

[96] V. M. Abazov et al. Helicity of the W boson in lepton + jets t anti-t events. *Phys. Lett.*, B617:1–10, 2005.

[97] D. Acosta et al. Measurement of the W boson polarization in top decay at CDF at $\sqrt{s} = 1.8$ TeV. *Phys. Rev.*, D71:031101, 2005.

[98] Kazuo Fujikawa and Atsushi Yamada. Test of the chiral structure of the top - bottom charged current by the process b $\rightarrow$ s gamma. *Phys. Rev.*, D49:5890–5893, 1994.

[99] Peter L. Cho and Mikolaj Misiak. b $\rightarrow$ s gamma decay in $SU(2)_L \times SU(2)_R \times U(1)$ extensions of the standard model. *Phys. Rev.*, D49:5894–5903, 1994.

[100] Colin Jessop. A world average for B $\rightarrow$ X/s gamma. SLAC-PUB-9610.

[101] B. Abbott et al. Spin correlation in t anti-t production from proton anti-proton collisions at $\sqrt{s} = 1.8$ TeV. *Phys. Rev. Lett.*, 85:256–261, 2000.

[102] G. Corcella et al. HERWIG 6: An event generator for hadron emission reactions with interfering gluons (including supersymmetric processes). *JHEP*, 01:010, 2001.

[103] Xiaojian Zhang. Opposite side jet charge tagging and measurement of CP asymmetry parameter sin(2beta) at D0. FERMILAB-THESIS-2004-13.

Acknowledgments

I would like to thank my supervisor Prof. Dr. Peter Mättig for offering me the opportunity to work on top quark physics. His continuous support and interest were very valuable for this analysis. Especially the long term stay at Fermilab and the frequent visits afterwards helped to keep in touch with the colleagues at DØ.

Prof. Dr. Avto Kharchilava had always an open door for my questions and problems concerning my work on the central fiber tracker. Dr. Aurelio Juste and the other members of the top group were never tired of telling me the right comments in order to bring this analysis closer to publication.

I would also like to thank all members of the Wuppertal high energy physics group for providing an excellent working environment in all aspects. Especially I would like to thank Dr. Torsten Harenberg and Dr. Andreas Kootz for their support regarding the computing infrastructure in Wuppertal and fruitful discussions concerning not only physics related topics. Dr. Klaus Hamacher and Dr. Daniel Wicke, thanks to their large experience, had always lots of suggestions on the analysis.

I would also like to thank my family for their infinite support during my whole life, even though it led me far away from home. Last but not least I would like to thank Lucia for entering my life just at the right moment. This thesis would not have been possible without her supporting me when I needed support and drawing off my attention whenever I needed a break. I will never be able to thank her enough!